INVESTIGATION OF IRON HYDROXIDE AND OXIDE-BASED AS CATHODES FOR SODIUM-ION BATTERIES

by

Sibo Niu, M.S.

A dissertation submitted to the Graduate Council of
Texas State University in partial fulfillment
of the requirements for the degree of
Doctor of Philosophy
with a major in Materials Science, Engineering, and Commercialization
December 2019

Committee Members:

Christopher P. Rhodes, Chair

Jennifer Irvin

Ben Martin

Gary Beall

William Chittenden

FAIR USE AND AUTHOR'S PERMISSION STATEMENT

Fair Use

Duplication Permission

ACKNOWLEDGEMENTS

This work was supported by the National Science Foundation (DMR-1205670). I would foremost like to thank my research advisor, Dr. Christopher Rhodes, for his generous support and great inspiration. I am sincerely grateful to work with him. I would like to express the deepest gratitude to my other committee members: Dr. Benjamin Martin, Dr. Jennifer Irvin, Dr. Gary Beall, and Dr. William Chittenden for their time and guidance. I am also grateful to all my group members in Dr. Rhodes' lab who have helped and inspired me in many ways.

TABLE OF CONTENTS

Page

ACKNOWLEDGEMENTS iv

LIST OF TABLES ix

LIST OF FIGURES xi

LIST OF ABBREVIATIONS xv

ABSTRACT xvi

CHAPTER

1. INTRODUCTION 1

1.1 The Configuration and Working Mechanism of The Rechargeable Batteries 1
1.2 Rechargeable Metal Batteries Beyond Li 4
1.2.1 Rechargeable Mg-Ion Batteries 5
1.2.2 Rechargeable Zn-Ion Batteries 7
1.2.3 Rechargeable K-Ion, Ca-Ion, Al-Ion, and Hybrid Dual-Ion Batteries 8
1.2.4 Rechargeable Na-Ion Batteries 11
1.3 Conventional Cathode Materials in Na-Ion Batteries and Their Challenges 13
1.4 Iron Hydroxide/Oxide Cathodes for Na-Ion Batteries 19
1.5 Effective Strategies to Improve Na^+ Insertion Kinetics 23
1.5.1 Effect of Particle Size on Na-Ion Storage and Transport within Active Materials 23
1.5.2 Effect of Morphology on Na-Ion Storage and Transport within Cathode Materials 25
1.5.3 Effect of Composition of Active Materials on Sodium-Ion Storage, Structural Stabilization, and Electrons Transport 28
1.5.4 Na-Ion Diffusion and Effect of Cation Defects on the Na-Ion Charge Storage Property of Iron Hydroxide/Oxide Cathodes 32
1.5.5 Effect of The Degree of Structural Order on Electrode Performance 34

1.5.5.1 General Studies on Effect of Structural Order on Electrode Performance 34
1.5.5.2 Effect of Structural Order on Na-Ion Charge Transport Within Iron-Based Cathodes 35
1.6 Structure, Properties, and Synthesis of Iron(III) Hydroxide ($Fe(OH)_3$) 36
1.7 Structure, Electronic Properties, and Synthesis of Hematite Phase Iron Oxide (α-Fe_2O_3) Nanoparticles and Iron Oxide (α-Fe_2O_3)/rGO Nanocomposites 40
1.7.1 Structure of Hematite (α-Fe_2O_3) and Transformation Upon Ion Diffusion 40
1.7.2 Electronic Properties of Hematite (α-Fe_2O_3) Nanoparticles...41
1.7.3 Synthesis of Hematite (α-Fe_2O_3) Nanoparticles 42
1.7.4 Synthesis of Hematite (α-Fe_2O_3) and Reduced Graphite Oxide (rGO) Nanocomposites 47
1.8 Objectives and Motivation 48

2. EXPERIMENTAL METHODS 51

2.1 Chemicals 51
2.2 Synthesis of Iron (III) Hydroxides Nanomaterials with Different Degrees of Crystallinity 51
2.3 Synthesis of Pristine α-Fe_2O_3 Nanoparticles and α-Fe_2O_3/rGO Nanocomposites 52
2.4 Structural, Physical and Electrical Characterization 53
2.5 Electrode Preparation and Cell Assembly 55
2.6 Electrochemical Measurement 56

3. RESULTS AND DISCUSSION 58

3.1 The Effect of Structural Order on the Na-Ion Storage Properties of Iron Hydroxide/Oxides Cathodes 58
3.1.1 Study of Phase and Crystallinity of Iron Hydroxide/Oxides Nanocomposites 58
3.1.2 Microscopy Analysis of $Fe(OH)_3$ and α-Fe_2O_3 Nanomaterials 60
3.1.3 Infrared Spectroscopic Analysis of $Fe(OH)_3$ and α-Fe_2O_3 Nanomaterials 61
3.1.4 Thermogravimetric Analysis (TGA) of $Fe(OH)_3$ and α-Fe_2O_3 Nanomaterials 64

3.1.5 Electrochemical Properties of Amorphous, Semi-Crystalline $Fe(OH)_3$, and Crystalline α-Fe_2O_3 Cathodes 68
3.1.5.1 Galvanostatic Charge-Discharge of Amorphous, Semi-Crystalline $Fe(OH)_3$, and Crystalline α-Fe_2O_3 Cathodes 68
3.1.5.2 Rate Capability of Amorphous, Semi-Crystalline $Fe(OH)_3$, and Crystalline α-Fe_2O_3 Cathodes 70
3.1.5.3 Cycling Stability of Amorphous, Semi-Crystalline $Fe(OH)_3$, and Crystalline α-Fe_2O_3 Cathodes 72
3.1.6 Study of Na-Ion Diffusivity and Electric Properties Within Amorphous, Semi-Crystalline $Fe(OH)_3$, and Crystalline α-Fe_2O_3 Cathodes.....74
3.1.6.1 Cyclic Voltammograms (CVs) of Amorphous, Semi-Crystalline $Fe(OH)_3$, and Crystalline α-Fe_2O_3 Cathodes at Different Scan Rates 74
3.1.6.2 Na-Ion Diffusion Coefficients of Amorphous, Semi-Crystalline $Fe(OH)_3$, and Crystalline α-Fe_2O_3 Nanomaterials 77
3.1.6.3 Electronic Conductivities of Amorphous, Semi-Crystalline $Fe(OH)_3$, and Crystalline α-Fe_2O_3 Nanomaterials 80
3.2 Development of Novel High-Performance Low Crystalline Iron Oxide (α-Fe_2O_3)/Reduced Graphite Oxide (rGO) Cathodes for Na-Ion Storage 81
3.2.1 Characterization of As-Prep Reduced Graphite Oxides (rGO).....81
3.2.1.1 X-Ray Diffraction Analysis of Pristine Graphite, Graphite Oxides (GO), and Reduced Graphite Oxides (rGO) 81
3.2.1.2 Analysis of As-Prep rGO Using Raman Spectroscopy 82
3.2.1.3 Morphological Analysis of As-Prep rGO Using TEM 84
3.2.1.4 TGA Analysis of As-Prep rGO.....84
3.2.1.5 The Na-Ion Storage Behavior of rGO Nanosheets As Cathodes 85
3.2.1.6 Cyclic Voltammogram (CV) of rGO 86
3.2.2 Characterization of Pristine α-Fe_2O_3 Nanoparticles and α-Fe_2O_3/rGO Nanocomposites 87
3.2.2.1 Scanning Electron Microscopy Analysis 87
3.2.2.2 X-Ray Diffraction 88

3.2.2.3 TGA Analysis 91
3.2.3 Electrochemical Properties of High Crystalline Commercial α-Fe_2O_3, Low Crystalline α-Fe_2O_3 and α-Fe_2O_3/rGO Nanocomposites 92

4. CONCLUSIONS.....102

REFERENCES 105

LIST OF TABLES

Table **Page**

1. Comparison of characteristics for Li^+ and Na^+ as charge carriers for rechargeable batteries 12

2. Performance features of cathode materials 14

3. Examples of current cathode materials for Na-ion batteries 20

4. Representative iron-based materials and their electrochemical performances as cathodes for Li-ion batteries 21

5. Theoretical capacities and electrochemical equations of representative ion-based materials using a one-electron process 22

6. A summary of the representative iron oxide and iron oxyhydroxides with rGO composites 32

7. Synthetic conditions of different $Fe(OH)_3$ and α-Fe_2O_3 nanomaterials 52

8. Average discharge capacities of amorphous, semi-crystalline $Fe(OH)_3$, and crystalline α-Fe_2O_3 cathodes at different current rate (the 2nd cycle) 71

9. Average capacity retention and coulombic efficiency of amorphous, semi-crystalline $Fe(OH)_3$, and high crystalline α-Fe_2O_3 cathodes at different current rate (the 2nd to 30th cycle) 73

10. Diffusion coefficients of amorphous, semi-crystalline $Fe(OH)_3$, and high high crystalline α-Fe_2O_3 cathodes 80

11. Electronic conductivities of amorphous, semi-crystalline crystalline $Fe(OH)_3$, and high crystalline α-Fe_2O_3 cathodes 81

12. Average discharge capacities of high crystalline commercial α-Fe_2O_3, low low crystalline α-Fe_2O_3, and α-Fe_2O_3/rGO nanocomposites at different mass-normalized current (the 2nd cycle) 96

13. Average discharge capacity of the 2nd cycle and the 50th cycle, capacity retention, and coulombic efficiency of high crystalline commercial α-Fe_2O_3, low crystalline α-Fe_2O_3, and α-Fe_2O_3/rGO nanocomposites (the 2nd to 50th cycle) at 0.1 C 99

14. Average discharge capacity of the 2nd cycle and the 50th cycle, capacity retention, and coulombic efficiency of high crystalline commercial α-Fe_2O_3, low crystalline α-Fe_2O_3, and α-Fe_2O_3/rGO nanocomposites (the 2nd to 150th cycle) at 1.7 C (34 minutes discharge time) 101

LIST OF FIGURES

Figure **Page**

1. Comparison of the different battery technologies in terms of volumetric and gravimetric energy density.....2

2. The working principles of Na-ion batteries 13

3. Comparison of charge and discharge of $LiCoO_2$ and $NaCoO_2$ for Li-ion and Na-ion batteries respectively 17

4. Charge and discharge curve of 400,100,10 nm Fe_3O_4 nanoparticles at the current rate of 20 mA g^{-1}. The electrolyte is 1 mol dm^{-3} $NaClO_4$ dissolved in ethylene carbonate (EC): dimethyl carbonate (DMC) 25

5. The comparison of rate study for hollow nanoparticles and solid nanoparticles.....27

6. The comparison of rate study for pure hollow nanoparticles, pure CNT, and hollow nanoparticles/CNT. Cells were operated within the voltage range of 1.1-4.0 V. The electrolyte is 1 M $NaClO_4$ in PC.....29

7. Comparison of cycling stability of amorphous and crystalline $FeVO_4$ nanoparticles. The inset shows the XRD patterns of two electrodes. 36

8. Ball-and-stick model of $Fe(OH)_3 \cdot H_2O$ crystal 37

9. The illustration of the local arrangements of the FeO_6 octahedra in $Fe(OH)_3$; (a) edge, (b) double-corner sharing linkages.....37

10. Hexagonal close–packed crystal structure of pure hematite.....41

11. XRD patterns of resulting materials prepared at different reaction times: (a) 0.5, (b) 1, (c) 2 h 44

12. XRD patterns of as-prepared products from urea-water hydrothermal system 45

13. XRD patterns of the products synthesized at 120 ºC at different times in 0.1M $Fe(NO_3)_3$ and 0.5 M urea aqueous solutions.....46

14. Schematic illustration of Na-ion coin cell assembly.....57

15. XRD patterns of $Fe(OH)_3/\alpha\text{-}Fe_2O_3$ obtained with different amount of urea and temperatures. 59

16. SEM images of $Fe(OH)_3$ and $\alpha\text{-}Fe_2O_3$ obtained at: (a) 120 °C, urea/Fe^{3+} = 0:1 (b) 120 °C, urea/ Fe^{3+}= 3: 1 (c) 120 °C, urea/ Fe^{3+}= 5:1 (d) 180 °C, urea/ Fe^{3+}= 3:1. 59

17. ATR-FT-IR spectra of as-prepared iron hydroxides/oxides with different degrees of crystallinity within the (a) 4000-400 cm^{-1} spectral range; (b) the expanded 4000-2500 cm^{-1} spectral range;(c) the expanded 1200-800 cm^{-1} spectral range; (d) the expanded 700-400 cm^{-1} spectral range. 62

18. TGA curves of iron hydroxides/oxides with different degrees of crystallinity 65

19. TGA curves of liquid EG 66

20. XRD pattern of $Fe(OH)_3$ nanomaterials (FE-3-120 sample) annealed at 400 ºC for 2h 67

21. Galvanstatic charge-discharge tests of amorphous, semi crystalline $Fe(OH)_3$ and high crystalline $\alpha\text{-}Fe_2O_3$ cathodes for the 3rd cycle (electrolyte with 1 M $NaClO_4$ in PC; counter/reference metallic Na; voltage range of 1.0-4.0 V vs Na; mass-normalized current of 47 mA g^{-1}) 69

22. Rate capability of amorphous, semi crystalline $Fe(OH)_3$ and high crystalline $\alpha\text{-}Fe_2O_3$ cathodes (electrolyte with 1 M $NaClO_4$ in PC; counter/reference metallic Na; voltage range of 1.0-4.0 V vs Na). 71

23. Cycling stability of amorphous, semi-crystalline $Fe(OH)_3$, and high crystalline $\alpha\text{-}Fe_2O_3$ cathodes (electrolyte with 1 M $NaClO_4$ in PC; counter/reference metallic Na; voltage range of 1.0-4.0 V vs Na). 72

24. Comparison of CVs of amorphous $Fe(OH)_3$ nanoparticles (FE-0-120) at different scan rates of 0.1, 0.2, 0.3, and 0.5 mV s^{-1} after a few cycles.....75

25. Comparison of CVs of lower semi-crystalline $Fe(OH)_3$ nanosheets (FE-3-120) at different scan rates of 0.1, 0.2, 0.3, and 0.5 mV s^{-1}. 76

26. Comparison of CVs of higher semi-crystalline $Fe(OH)_3$ nanosheets (FE-5-120) at different scan rates of 0.1, 0.2, 0.3, and 0.5 mV s^{-1}.....77

27. Comparison of CVs of high crystalline α-Fe_2O_3 nanoparticles (FE-3-180) at different scan rates of 0.1, 0.2, 0.3, and 0.5 mV s^{-1}.....78

28. Peak current (I_p, A) vs. square root of scan rate ($V^{1/2}$, $V^{1/2}$ $s^{-1/2}$) and related linear fit within $Fe(OH)_3$/α-Fe_2O_3 with different degrees of crystallinity. 79

29. XRD patterns of pristine graphite, GO, and rGO 82

30. Raman spectra of rGO 83

31. Transmission electron microscopy (TEM) image of rGO 84

32. TGA curves of as-prep rGO..... 85

33. Galvanostatic charge and discharge voltage profiles (second cycle) of rGO nanosheets (electrolyte 1 M NaClO4 in PC; counter/reference metallic Na).....86

34. CV scan of rGO at a scan rate of 1 mV s^{-1} in a voltage range of 1.0–4.0 V vs Na.....87

35. SEM images of (a) the commercial α-Fe_2O_3, (b) pristine FeO_x, (c) FeO_x/rGO nanocomposites.....88

36. XRD patterns of high crystalline commercial α-Fe_2O_3, low crystalline α-Fe_2O_3, and α-Fe_2O_3/rGO nanocomposites.....89

37. TGA curves of high crystalline commercial α-Fe_2O_3, low crystalline α-Fe_2O_3, and α-Fe_2O_3/rGO nanocomposites. 92

38. Galvanstatic charge-discharge tests of high crystalline commercial α-Fe_2O_3, low crystalline α-Fe_2O_3, and α-Fe_2O_3/rGO nanocomposites (electrolyte with 1 M NaClO4 in PC; counter/reference metallic Na; voltage range of 1.0-4.0 V vs Na; mass-normalized current of 16.7 mA g^{-1}).....93

39. Rate capability tests of high crystalline commercial α-Fe_2O_3, low crystalline α- Fe_2O_3, and α-Fe_2O_3/rGO nanocomposites (electrolyte with 1 M $NaClO_4$ in PC; counter/reference metallic Na; voltage range of 1.0-4.0 V vs Na.) 95

40. Cycling stability tests of high crystalline commercial α-Fe_2O_3, low crystalline α-Fe_2O_3, and α-Fe_2O_3/rGO nanocomposites (electrolyte with 1 M $NaClO_4$ in PC; counter/reference metallic Na; voltage range of 1.0-4.0 V vs Na; C-rate ~0.1 C (mass-normalized current of 20 mA g^{-1})).....96

41. Cycling stability tests of high crystalline commercial α-Fe_2O_3, low crystalline α-Fe_2O_3, and α-Fe_2O_3/rGO nanocomposites (electrolyte with 1 M $NaClO_4$ in PC; counter/reference metallic Na; voltage range of 1.0-4.0 V vs Na; C-rate = 1.7 C (mass-normalized current of 170 mA g^{-1})).....100

LIST OF ABBREVIATIONS

Abbreviation	Description
CE	Coulombic efficiency
CNTs	Carbon nanotubes
CV	Cyclic voltammetry
DEC	Diethyl carbonate
DFT	Density functional theory
EC	Ethylene carbonate
EDLC	Electric double-layer capacitive
EG	Ethylene glycol
EVs	Electric vehicles
GO	Graphite oxide
PC	Propylene carbonate
rGO	Reduced graphite oxide
SEM	Scanning electron microscope
SEI	Solid electrolyte interphase
SHE	Standard hydrogen electrode
TEM	Transmission electron microscopy
TGA	Thermogravimetric analysis
XRD	X-ray powder diffraction

ABSTRACT

Na-ion batteries have received significant attention for their low-cost, resource abundance, and similarities to commercial Li-ion batteries. However, the development and commercialization of Na-ion batteries have been impeded by a lack of suitable cathodes that can accommodate the large radius of Na^+ and provide high Na-ion diffusivity. Iron hydroxides/oxides have been considered as potential cathodes for Na-ion storage. However, iron hydroxide/oxide cathodes typically show low specific capacities, poor rate capabilities, and substantial capacity degradation upon cycling. Altering the degree of crystallinity or structural order provides an approach to improve the electrochemical properties of iron oxides and iron hydroxides, because an amorphous structure or a low crystallinity can facilitate Na-ion diffusion and accommodate the Na-ion insertion/de-insertion within cathodes, leading to higher specific capacities, better rate capabilities, and improved cycling stabilities. Herein, in the first part of this work, iron (III) hydroxides, $Fe(OH)_3$, with different degrees of crystallinity were prepared by altering the precursor concentrations and synthesis temperature during the hydrothermal synthesis process. The electrochemistry results show that $Fe(OH)_3$ cathodes with low crystallinity exhibit higher reversible capacities, much better rate capabilities, and improved capacity retention upon cycling compared with crystalline counterparts. The enhanced electrochemical performance of low crystallinity $Fe(OH)_3$ cathodes is attributed to the combination of facilitated Na-ion mobility, improved ability to accommodate reversible volume changes during ion insertion/de-insertion within the structure, and a

higher degree of ion storage sites within the material. However, it was also found that a semi-crystalline $Fe(OH)_3$ cathode provided improved rate capability and cycling life compared with the counterpart with a completely amorphous structure suffered from an extremely low electronic conductivity, resulting in low specific capacities at high current rates. The better electrochemical performance of semi-crystalline $Fe(OH)_3$ cathode is attributed to the multiple factors, such as morphology, electronic and ionic conductivity. However, the cycling stability of low crystalline $Fe(OH)_3$ cathodes is still needed to be further improved for practical applications.

In the second part of this dissertation, to improve the cycling stability, low crystalline α-Fe_2O_3/reduced graphite oxide (rGO) nanocomposites were synthesized via a rapid microwave synthesis method to enhance the electronic conductivity and structural stability by integration of rGO compared to pristine α-Fe_2O_3 nanoparticles. Products with low crystallinity were obtained from the short reaction times. The results show that α-Fe_2O_3/rGO nanocomposite cathodes exhibit superior electrochemical properties compared to highly crystalline commercial α-Fe_2O_3 nanoparticles and low crystalline α-Fe_2O_3 nanoparticles with rGO high-performance and low-cost cathodes for Na-ion batteries.

1. INTRODUCTION

1.1 The Configuration and Working Mechanism of Rechargeable Batteries

Global energy consumption has been dramatically increasing during the past decades, leading to the massive emissions of carbon dioxide (CO_2) and extremely high dependence on fossil fuels.[1-4] It is a well-known fact that the CO_2 emissions can acidify oceans and contribute to global warming.[5] Therefore in order to reduce CO_2 emissions and meet the increasing demand for energy, it is very critical to have clean and sustainable source of energy, such as solar- and wind-based power, and biofuel.[3] However, so far, these types of renewable energy are relatively high cost, low efficiency, and need significant further development efforts.[6] In addition, energy storage systems are in urgent demand. Furthermore, due to a fast-growing demand from electrical energy storage devices, there is an urgent need to develop low-cost, stable and efficient energy storage systems.[7]

The Li-ion battery, as one type of rechargeable batteries, has been considered as the most successful technology for its wide applications in portable consumer electronic devices such as smart-phones, tablet computers and laptops. Advantages of Li-ion batteries include high voltage, high energy density, no memory effect, long cycle life, and broad temperature range of operation.[8] Figure 1 shows the comparison of the different battery technologies with respect to volumetric and gravimetric energy density.[9] Compared to lead-acid batteries, Ni-Cd batteries, Ni-MH batteries, and Li metal batteries, Li-ion batteries exhibit much higher volumetric energy density and gravimetric energy density,

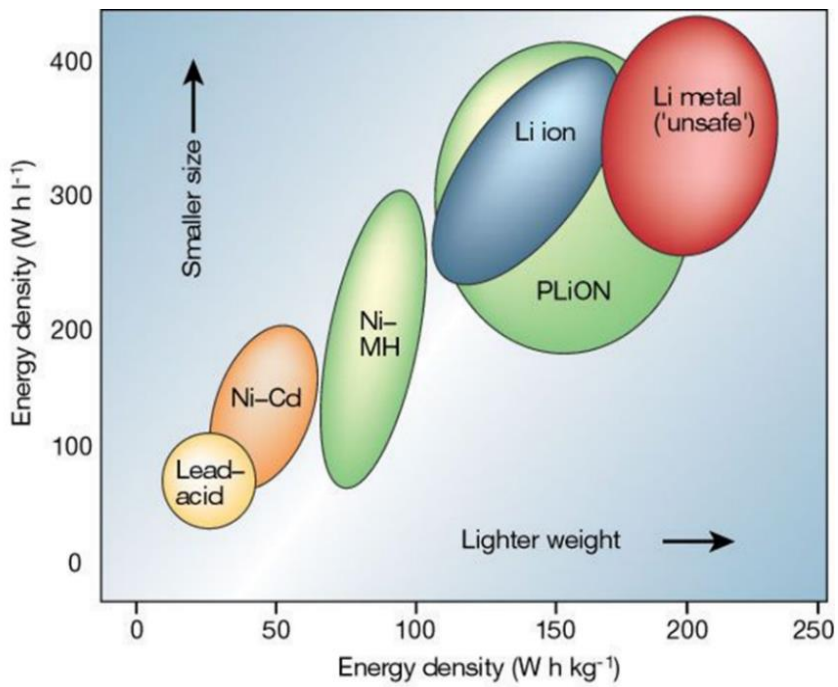

Figure 1. Comparison of the different battery technologies in terms of volumetric and gravimetric energy density.[9]

A battery is composed of one or more interconnected electrochemical cells to provide the capacity giving a certain current at a voltage for a time Δt.[10] A single electrochemical cell has four major components: a cathode, anode, electrolyte, and separator. The electrolyte can be either a liquid or a solid phase. However, due to the problem of solid-solid interfaces, solid electrolytes are most compatible with gaseous or liquid electrodes.[10] Instead, liquid electrolytes are normally used for conventional solid electrodes. Electrolytes are ionically conductive and allow shuttling of Li ions between the cathode and the anode. Electrons are transported through the external circuit. During the discharging process, Li^+ as well as electrons move from the anode to the cathode. Upon charging, Li^+ and electrons are moved from cathodes to anodes accompanied with the redox reaction, which can be generally described using the following expression:[11]

$$\mathrm{Li}x_i[\text{cathode}] + (x_j - x_i)\mathrm{Li}[\text{anode}] \leftrightarrow \mathrm{Li}x_j\,[\text{cathode}] + [\text{anode}] \quad (1)$$

where x_i and x_j indicate the solid solubility limits of the intercalation reaction. The change in Gibbs free energy (ΔG) between the charged and discharged state is described by the following equation [12]:

$$\Delta G_r = \Delta H_r - T\Delta S_r = \Delta U_r + P\Delta V_r - T\Delta S_r \quad (2)$$

where P is the pressure and T is the temperature of the system. $P\Delta V_r$ and $T\Delta S_r$ represent the volume change and the difference in the vibrational and configurational entropies of ion insertion or extraction. ΔU_r is the change in internal energy. The chemical potential μ is associated with the partial molar quantity of Gibbs free energy G. Therefore, the equilibrium voltage, $E(x)$, is shown as follows:[13]

$$E(x) = \frac{-\Delta G}{(x_j - x_i)F} \quad (3)$$

where F is the Faraday constant.

During the electrochemical process, the discharge voltage, V_{dis}, and charge voltage, V_{ch}, are determined by initial open-circuit voltage, V_{oc} and polarization, η, as a result of the internal battery resistance R_b. The overvoltage, discharge voltage, and charge voltage can be described as following equations:[10]

$$\eta = I_{ch}R_b \quad (4)$$

$$V_{dis} = V_{oc} - \eta\ (q, I_{dis}) \quad (5)$$

$$V_{ch} = V_{oc} + \eta\ (q, I_{ch}) \quad (6)$$

where q represents the state of charge, and I_{dis} and I_{ch} are ionic current at charge and discharge process, respectively. Since the output power, $P\ (q) = V(q)\ I_{dis}$, for a given discharge current, in order to have high energy, it is good to have a high open-circuit voltage but a low polarization (low internal battery resistance). V_{oc} is the difference in

chemical potential between the anode (μ_A) and the cathode (μ_c), which is expressed as following equation:[14]

$$\text{Voc} = \frac{\mu_{A-}\mu_C}{e} \tag{7}$$

where e is the magnitude of the electronic charge. The working potential is also limited by the electrochemical window of the electrolyte.

The cell efficiency at a fixed current *I* can be described as following equations:[10]

$$I_{\text{cell}} = 100 \times \frac{\int_0^{Q_{dis}} V_{dis}(q)\text{dq}}{\int_0^{Q_{ch}} V_{ch}(q)\text{dq}} \tag{8}$$

$$\text{Q} = \int_0^{\Delta t} I dt = \int_0^{Q} dq \tag{9}$$

where Q represent the total charge per unit weight (Ah kg^{-1}) transfer by the current I = dq/dt on discharge or charge. Q is dependent on *I* due to the rate of transfer of ions across electrode/electrolyte interfaces, which is a diffusion-limited factor at high current rate,[15] resulting in a reversible loss of capacity at a high rate of charge or discharge. Moreover, the chemical reactions between electrode-electrolyte, structural changes in electrode volume, and electrode decomposition can contribute to the irreversible loss of capacity.[16] For example, the irreversible formation of the solid-electrolyte interphase (SEI) layer that forms during first few cycles contributes to irreversible losses. The percent Coulombic efficiency of each cycle involving a fading capacity is described:[10]

$$I_{CE} = 100 \times \frac{Q_{dis}}{Q_{ch}} \tag{10}$$

1.2 Rechargeable Metal Batteries Beyond Li

Although Li-ion batteries have great a success in addressing problems with increasing demand of sustainable energy, there is a rising concern about the feasibility of lithium.[17] Lithium in the earth's crust is limited to only 20 ppm (0.0007 %

of the earth's crust).[18] As a result, the price of lithium has been continually increasing for the past decade from ~ $ 5,000 per metric ton in 2008 to $16,000 per metric ton at the beginning of 2018.[19] It is expected that with such a limited availability, any increase in demand would truly boost the price of Li metal in the world market. Currently, battery technology is extending to large-scale devices, such as electric vehicles (EVs) and electric grids, requiring the production of renewable energy to be inexpensive and efficient. Therefore, beyond Li-ion batteries, several novel rechargeable metal battery systems are under investigation.

1.2.1 Rechargeable Mg-Ion Batteries

Rechargeable magnesium ion (Mg-ion) batteries are one type of rechargeable metal batteries, which pair metallic a Mg anode with various cathodes. Rechargeable Mg-ion batteries have been recognized as promising alternatives to Li-ion batteries because of the ideal features of a high volumetric energy density (3,833 mAh cm^{-3} of Mg anode), natural abundance (1.5 wt % in earth crust and 0.13 wt % in sea water), and high safety without dendrite deposition at the anode side.[20] However, the primary challenges of commercialization of Mg-ion batteries lie in identification of suitable cathode materials and efficient electrolytes with a good Mg-ion conductivity and stability, contributing to a high operating voltage and high capacities.[21] The divalent charge of Mg-ion causes complicated moisture-sensitive electrolyte chemistry and results in sluggish solid-state Mg-ion diffusion and slow interfacial charge transfer.[22] Compared to monovalent cations (Li^+, Na^+ and K^+), the high charge density of Mg^{2+} (twice as high as Li^+) inevitably enhances the energy barrier of solvation.[23] Furthermore, divalent Mg-ions also induce strong electrostatic interactions with the host lattice upon ion insertion and hopping.

Thus, it is difficult to find suitable cathode materials with reasonable kinetics and high reversibility.

Prior studies has explored layered intercalation compounds, including manganese dioxide (α-MnO_2),[24] vanadium pentoxide (V_2O_5),[25] TiS_2,[26] and MoS_2[27] as positive electrode materials for Mg-ion storage. However, these host materials exhibited substantial polarization with Mg^{2+}, causing slow Mg^{2+} diffusivity. Some pioneering research found that shielding of the Mg^{2+} charge via wet electrolytes, insertion/deinsertion of big guest ionic groups, and doping other divalent cations can decrease the electrostatic interaction and facilitate Mg-ion diffusion coefficients, contributing to improved specific capacities, especially at high current rates.[25] In spite of this work, these strategies cannot completely eliminate the effect of large electron density of Mg^{2+} on slow solid-state diffusion of Mg^{2+} cations. In addition, the use of these electrolytes limits greatly the choice of cathodes for Mg^{2+} storage. Electrolytes, such as propylene carbonate (PC), ethylene carbonate (EC) and diethylene carbonate (DEC), which are widely used in Li-ion batteries, cannot be used in Mg-ion batteries electrolytes because they are readily reduced on the Mg anode forming a passivating layer.[28] Furthermore, it is hard to find suitable electrolytes that can reversibly strip or plate the Mg^{2+} efficiently.[29] Some electrolytes do enable reversible Mg dissolution, for example, organohaloaluminate/ether electrolytes. However those electrolytes typically exhibit relatively narrow electrochemical stability window, of up to 2.2 V vs. Mg (~2.8 V vs. Li/Li+), leading to lower specific capacities.[30] Therefore, it seems unlikely to make Mg-ion batteries practical within a short term and replace commercial Li-ion batteries.

1.2.2 Rechargeable Zn-Ion Batteries

Similar to Mg-ion batteries, zinc ion (Zn-ion) batteries match zinc metal as the anode electrode with transition metal cathodes with advantages of a very high volumetric capacity (5845 mAh cm^{-3} of Zn anode) and relative lower cost.[31] Nevertheless, after awareness of the similar problems that non-aqueous Zn-ion batteries may have the same issues as divalent ions in Mg-ion batteries, Zn-ion batteries have recently been reexplored using the aqueous electrolytes. Compared to non-aqueous batteries, aqueous Zn-ion batteries are promising for grid-scale electrochemical energy storage due to their low-cost and high operational safety.[32] More importantly, the ionic conductivity of aqueous electrolytes (~1 S cm^{-1}) is 2 orders higher than that of organic electrolytes (~ 1-10 mS cm^{-1}), contributing to superior capabilities of Zn-ion charge transfer.[33] For example, Chen et al. developed porous V_2O_5 nanofibers as cathode materials for rechargeable aqueous Zn-ion batteries.[34] The V_2O_5 cathodes delivered a discharge capacity of 100 mAh g^{-1} at 10 C. Moreover, the cathodes maintained an 80% of the initial discharge capacity after 500 cycles. Li et al. reported a rechargeable aqueous Zn-ion battery based on a $Na_3V_2(PO_4)_2F_3$ cathode. $Na_3V_2(PO_4)_2F_3$ cathodes exhibited an extraordinary cycling stability of with 95% capacity retention over 4000 cycles.[35] Alfaruqi et al. reported using layered-type birnessite δ-MnO_2 nanoflakes as cathodes for zinc-ion battery applications; they showed a discharge capacity of 112 mAh g^{-1} after 100 cycles.[36]

However, many challenges still exist in making great breakthroughs in high-performance aqueous Zn-ion batteries. One of the problems so far is a low operation voltage (0.4-1.1V vs. Zn) in the aqueous battery and resulting in side reaction with water or electrolytes.[37] The Zn anode possesses a redox potential (−0.76 V vs standard

hydrogen electrode (SHE)) in aqueous electrolytes.[38] When operated at a low voltage range, other ions (H^+ and OH^-) instead of only Zn^{2+} can shuttle between the cathode and the anode, leading to low CE and formation of byproducts.[39] In alkaline Zn batteries, metallic Zn anodes react with OH^- and form ZnO byproducts and dendrites. Even though aqueous rechargeable Zn-ion batteries have unique benefits as energy storage devices, there are still some challenges which limit their practical applications.

1.2.3 Rechargeable K-Ion, Ca-Ion, Al-Ion, and Hybrid Dual-Ion Batteries

Besides Mg-ion and Zn-ion batteries, other types of rechargeable metal batteries, such as potassium (K)-ion, calcium (Ca)-ion, and aluminum (Al)-ion batteries are under investigation. Rechargeable K-ion batteries employ potassium metal as the anode side. K^+ as charge carriers are transported between anodes and cathodes. The merits of K-ion batteries include relatively a high energy density, low cost, and fast ion transport kinetics in electrolytes.[40] However, K^+ has the largest atomic radius (1.38 Å) compared to Li (0.68 Å), causing poor K^+ kinetics in solid electrodes and a low diffusivity.[41] Another issue as a result of the largest K^+ radius is tremendous volume change and phase transformation of active materials over cycling due to insertion/extraction of K^+. The repeated K-ion insertion/deinsertion results in pulverization and electrochemical inactive areas isolated from the conductive agents and irreversible capacity fading.[42] A number of cathode materials have been examined for K-ion storage, such as layered oxide compounds, Prussian blue analogs, polyanionic compounds, and organic compounds.[43] However, extensive studies will be needed to overcome the drawbacks of K-ion batteries.

Rechargeable Ca-ion batteries are another type of appealing novel batteries. Ca is the fifth most abundant element in the earth's crust. Similar to Mg-ion and Zn-ion

batteries, Ca^{2+} can carry two charges due to their divalent nature. Ca anode have a high gravimetric capacity of 1,340 mAh g^{-1}.[44] However, the development of Ca-ion batteries is extremely challenging. The lack of high-performance cathodes pairing with Ca anodes and electrolytes with high Ca-ion conductivity/activity impede the application of Ca-ion batteries. Prior studies found that conventional electrolyte systems based on a mixture of carbonate solvents containing Ca^{2+} salts, such as $Ca(ClO_4)_2$, $Ca(BF_4)_2$, and $Ca(TFSI)_2$ (calcium trifluoromethanesulfonimide) did not work for Ca-ion batteries, with no redox processes observed at room temperature.[45] At elevated temperatures (50-100 ºC), $Ca(ClO_4)_2$ and $Ca(BF_4)_2$ solvent exhibited reversible redox processes but also led to side reactions and formed CaF_2 as an undesirable byproduct.

In order to rationally design and develop cathode materials for Ca-ion batteries, density functional theory (DFT) modeling has been extensively used to efficiently predict the kinetics and Ca-ion storage properties of active materials.[46] It has been reported that multivalent ion mobility within spinel Mn_2O_4, olivine $FePO_4$, layered NiO_2, and orthorhombic δ-V_2O_5 can be calculated, and the results were used to improve the ionic mobility via modification of host materials.[47] However, a lot of work is needed toward the successful development and commercialization of Ca-ion batteries.

Al-ion batteries have metallic Al negative electrodes, cathodes and Al^{3+} salts. Similar to other metal batteries (except Li-ion batteries), the benefits of rechargeable Al-ion batteries are low cost, natural abundance, and high theoretical energy density (13.4Wh/cm^3).[48] In addition, insertion of one Al^{3+} can exchange three redox electron. Noticeably, the radius of Al^{3+} (0.54 Å) is quiet similar to or even smaller than Li^+ (0.76 Å), therefore, host materials will not exhibit lattice twist or volume expansion upon Al-

ion intercalation.[49] However, it has been found that it is very challenging to develop efficient electrolytes that can reversibly electroplate and electrostrip Al^{3+}.[49] Also, recently little progress has been made for investigation of host materials for Al-ion intercalation.

After being aware of the drawbacks of rechargeable multivalent batteries, researchers began to consider that how to avoid the large ion intercalation within positive host materials and eliminate the capacity degradation over battery cycling. Therefore, dual-ion batteries have received much attention. The merit of dual-ion batteries is to use two different charge carriers. One is Li^{+} inserting into cathodes. The other one can be Mg^{2+} or Al^{3+}, which are stored in metallic Mg or Al anodes.[50] The cell configuration of dual-ion batteries makes it easy to find suitable cathodes for Li-ion storage. However, it is challenging to find efficient electrolytes that can have good ionic conductivities for Li^{+} and Mg^{2+}/Al^{3+}. In dual-ion batteries, as electrolytes are the ion source for the intercalation/deintercalation process on both cathode and anode, it plays an important role as an active material. Furthermore, the concentration of electrolytes and ionic conductivities exhibit a dynamic feature upon the charge/discharge process, leading to concentration gradients within the cell.[51] It was also found that the concentration of Li^{+} significantly influenced the ionic conductivity of electrolyte as well as the electrochemical performance of battery cells.[52] Mao et al. reported a novel dual-ion electrolyte by mixing LiTFSI and inorganic LiFSI, where LiFSI (lithium bis(fluorosulfonyl)imide) not only provided high conductivity, but also dominated the interfacial behavior, while LiTFSI acted as a stabilizer and conducting agent. The results showed that a 99% CE and good cycling performance at a high current 10 mA cm^{-2}.[52] In general, these novel rechargeable batteries remain too far from commercialization within

a short term even though they have undoubled advantages compared to current Li-ion batteries.

1.2.4 Rechargeable Na-Ion Batteries

Sodium-ion (Na-ion) batteries, as the earliest battery system that was developed in parallel to Li-ion batteries, have recently gained much interest once again after so much work on development of other new batteries beyond Li-ion. It has been realized Na-ion batteries are much closer to be applied as good alternatives to commercial Li-ion batteries. Sodium-ion battery technology at ambient temperature is similar to Li-ion batteries. Na^+ are monovalent charges, thus reducing the potentially strong electrostatic interaction of divalent cations with host materials. Furthermore, Na^+ are much more active to be stripped/deposited compared with Mg^{2+} and Zn^{2+}, therefore, it is much easier to develop suitable electrolytes for reversibly electrodepositing/stripping sodium metal and intercalating Na^+ into host compounds which served as cathodes. Elemental Na is located right below Li in the periodic table and shares similar chemical properties. However, in contrast to Li, Na is one of the most abundant elements in Earth's crust (above 1%). The price of Na metal (~$3000 per metric ton) is much cheaper than Li metal (~$16,500 per metric ton).[53]

At ambient temperature, both Na-ion and Li-ion batteries have been under investigation since in the early 1980s.[54-56] Compared to Na-ion batteries, Li-ion batteries have a higher energy density, thus becoming dominant in the market of portable electronic devices. However, in large-scale energy storage devices, gravimetric energy density is not as essential. Therefore, recently, Na-ion batteries once again have attracted significant interest. Nonetheless, several barriers need to be overcome before Na-ion

batteries become a practical reality. Even though sharing similarity in cell configuration with Li-ion batteries, there are a few fundamental differences between Na-ion and Li-ion batteries, as shown in Table 1.[57-58]

Table 1. Comparison of characteristics for Li^+ and Na^+ as charge carriers for rechargeable batteries.[29-30]

	Li^+	Na^+
Ionic radius (Å)	0.76	1.02
Relative atomic mass (u)	6.94	23.00
E°(vs SHE)/V in the aqueous solution	-3.04	-2.71
Gravimetric energy density (Wh/kg)	3861	1166
Desolvation energy in PC (kJ mol^{-1})	218.0	157.3
Coordination environment	Octahedral and tetrahedral	Octahedral and prismatic

The working principle and configuration of Na-ion batteries are the same as for Li-ion batteries, as shown in Figure 2.[53] Na^+ are shuttled between cathodes ($NaCoO_2$) and anodes (graphite) through electrolytes upon charge and discharge. Electrons migrate externally but along the same direction as Na^+. Since Na^+ have a larger radius than Li^+, electrodes (both cathodes and anodes) can be substantially pulverized due to significant volume expansion during Na^+ insertion. Additionally, it is hard for most electrodes to accommodate Na^+ unless host materials possess channels and/or interstitial sites.[59-60] Moreover, the operation voltage of Na-ion batteries is 330 mV lower than that of Li-ion batteries. It is a huge challenge to get cathode materials having redox reactions at relatively high voltage vs. Na reference electrode, resulting in a low specific capacity. Therefore, extensive efforts have been devoted to developing high-performance

cathode materials.[61]

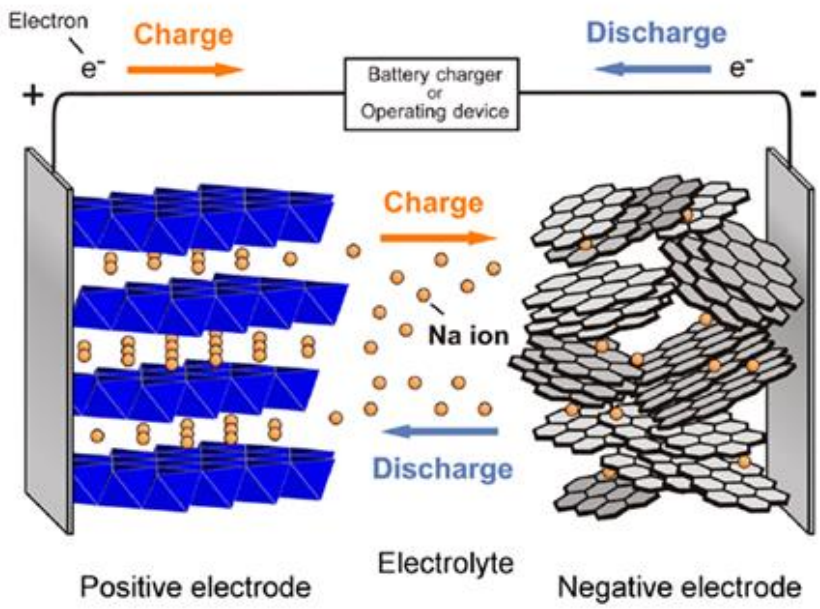

Figure 2. The working principles of Na-ion batteries.[51]

1.3 Conventional Cathode Materials in Na-Ion Batteries and Their Challenges

The electrochemical performance of Na-ion batteries is dependent on the electrode materials, particularly the cathode materials since the capacity of Na-ion full cells is limited by the capacity of the cathode materials. Upon charging and discharging, cathodes experience several processes simultaneously: 1) Na-ion insertion and extraction into or out of cathode materials; 2) electrons transported from the active materials interior to its surface across the junction of current collector; and 3) Na-ion migration from the interior of active materials to the solid-electrolyte interface. All these steps above affect the performance of cathodes and hence battery capacities. The electrochemical properties of cathode materials are normally evaluated in a Na-ion half-cell configuration where the anode side is Na metal with a fixed potential (-2.71V versus SHE). The cell voltage can be used to precisely indicate the potential of the cathodes of interest. There are several

criteria used to determine the attributes of cathodes, including safety, specific capacity,

Table 2. Performance features of cathode materials[13]

Features	Unit	Equation	Notes
Theoretical capacity	mAh g^{-1}	$Q_{therotical}=\frac{nF}{3.6*M_w}$	n represents the number of electrons transferred per active element F represents Faraday constant M_w represents molar weight of active cathode material
Rate capability	N/A	N/A	The specific capacity obtained at different C-rate
Cycling stability	N/A	$\frac{Q_{discharge}^{N^{th}\ cycles}}{Q_{discharge}^{inital}} \times 100\%$	Discharge capacity retention relative to initial capacity after N cycles
Coulombic efficiency	N/A	CE = $\frac{Q_{discharge}}{Q_{charge}} \times 100\%$	The charge and electrons transfer red within battery The closer to 100%, the better performance
Volumetric energy density	Wh L^{-1}	$D_{volumetric}=\frac{\int_{V_0}^{V_t} Q(v)dv}{V_w}$	The amount of electrical energy per unit of weight V_w represents molar volume
Gravimetric energy density	Wh kg^{-1}	$D_{Gravimetric}=\frac{\int_{V_0}^{V_t} Q(v)dv}{m_w}$	The amount of electrical energy per unit of weight m_w represents molar mass

voltage, and cycle life. Perform parameters for cathode materials are shown in Table 2.[13]

The electromotive force (E) of Na-ion batteries obeys the equation:[62]

$$E = E_{\text{Cathode}} - E_{\text{Na}} = -\frac{\Delta G}{nF} \tag{11}$$

where ΔG is the Gibbs' free energy difference, and E_{cathode} and E_{Na} are potentials of the cathode and the Na reference electrode (anode), respectively. The potential of cathode materials is intrinsically determined by the energy position (vs Fermi level of metallic

Na) of the redox couples, which can be raised by increasing the inductive effect of anions.[63]

The cycle life of cathode materials is significantly influenced by the structural stability of materials themselves as well as the electrochemical stability of electrolytes. Capacity degradation is usually attributed to irreversible structural changes induced by the large expansion of Na-ion insertion.[64] With respect to electrolytes, if the energy level of the cathode is lower than the highest occupied molecular orbital (HOMO) energy of electrolytes, oxidation decomposition of the electrolytes will occur, result from the thermodynamically favorable electron transfer from electrolytes to cathode materials which contributes to the decomposition of the electrolyte and capacity fading.[65] Therefore, it is very essential to match cathode materials with appropriate electrolytes.

The rate capability of cathode materials of Na-ion batteries is governed by Na-ion diffusivity and electron conductivity. In general, ion diffusion in host electrode materials is associated with the diffusion length (L_{ion}) and diffusion coefficient (D_{ion}), which can be represented as the equation:[66-68]

$$\tau = \frac{L_{ion}^2}{D_{ion}} \tag{12}$$

where τ is the characteristic time for diffusion. Based on the atomic theory of diffusion, vacancies and interstitials can promote ion diffusion through the crystal.[69]

Because of the similarities of electrode materials and working mechanisms between Li-ion and Na-ion batteries, the knowledge accumulated for cathode materials in Li-ion batteries can be used as basic principles for investigation of cathode materials for Na-ion batteries. For Li-ion batteries, typical cathode materials are transition metal compounds, oxides, or complex oxides.[70] Inserted Li^+ often occupy spaces between

adjacent layers, unoccupied octahedral or tetrahedral sites, and vacancies in crystal structures. On the other hand, electrons migrate into available *d* orbitals of the transition metal cations in the host crystal. The change in the Gibbs free energy and the electrochemical potential of the lithiated cathode material mainly relies on the valence state, ionic radius, electronegativity, and local environment of the transition metal cations.[11]

Goodenough et al. recognized $LiCoO_2$ was suitable for Li-ion battery cathodes, which further became a widely applied commercial cathode material since in 1991 due to its several advantages, such as a high redox voltage potential (~ 4 V vs. Li), a high theoretical capacity (273 mAh g^{-1}), and an excellent cycling stability at room temperature.[71] Similarly, by replacing Li^+ replaced Na^+ , $NaCoO_2$ with a layered structure was developed.[53] Electrochemical storage of Na-ion using $NaCoO_2$ can be described by the following equation:[53]

$$NaCoO_2 \leftrightarrow NaCoO_2 + xNa^+ + xe^- \quad (13)$$

As shown in Figure 3, the initial charging voltage of $LiCoO_2$ (~3.0 V) is ~ 1.0 V higher than that of $NaCoO_2$ (~ 2.0 V).[53] Once both cells reach charge capacities of higher than 100 mAh g^{-1}, the voltage difference between Na-ion and Li-ion batteries shrank to ~ 0.4 V, indicting the reduction becomes more significant as Na^+ concentration increases. However, generally, as a cathode material for Na-ion batteries, $NaCoO_2$ does not show as good electrochemical performance as that of Li counterpart ($LiCoO_2$) for Li-ion batteries. Following the same strategy, a series of layered transition metal oxides, $NaAMO_2$ (A=Mn, Fe, and Ni) were synthesized and evaluated their electrochemical properties.[72-74]

The motivation was to reduce the content of high cost and short supply cobalt metal. Moreover, inclusion too much cobalt has been verified to generate thermal instability of cathodes, preventing their applications in large-scale Na-ion batteries.[75] For example, electrochemical properties of both α- and β- $NaMnO_2$ were first investigated in 1985.[76] Even though the theoretical capacity of $NaMnO_2$ is 242 mAh g^{-1}, the reversible capacity of α- and β- $NaMnO_2$ was only ~50 mAh g^{-1} and 36.3 mAh g^{-1}, respectively, due to the irreversible sodiation and desodiation of Na^+ within $NaMnO_2$ crystals.[61] $NaFeO_2$ is a low cost and cobalt free cathode material with a flat voltage plateau at 3.3 V vs Na metal. Although the practical capacity of $NaFeO_2$ is higher than that of $NaMnO_2$, the reversible capacity was only 85 mAh g^{-1}.[77] So far, none of these cathodes are good enough to be commercially applied for Na-ion batteries.

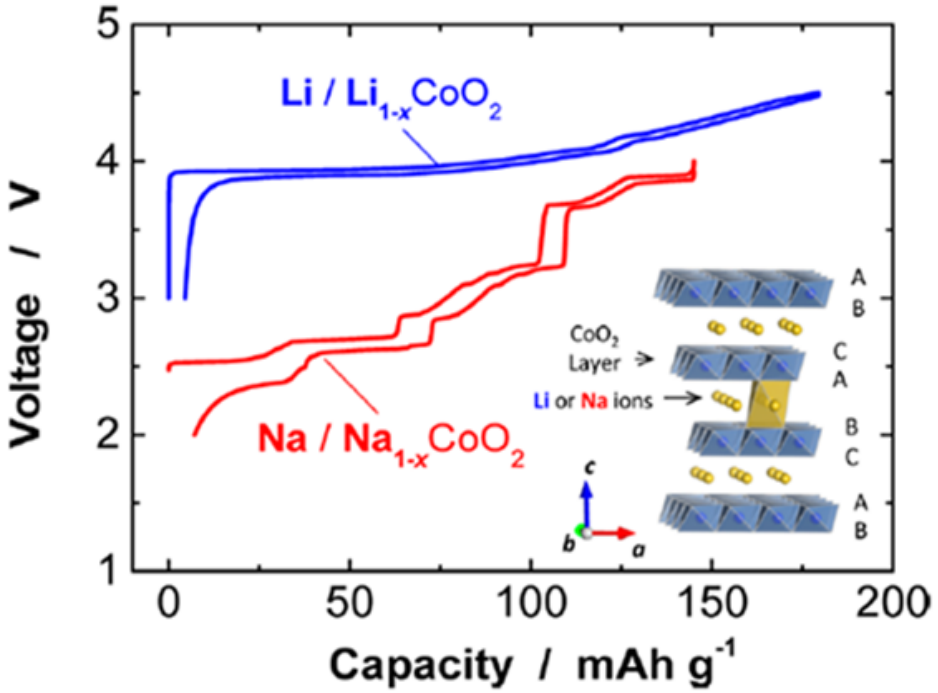

Figure 3. Comparison of charge and discharge of $LiCoO_2$ and $NaCoO_2$ for Li-ion and Na-ion batteries respectively.[51]

Besides the single transition-metal oxides, Na-inserted layered mixed-cation oxides are designed with consideration of cooperative effect of contributions of various metals in order to reduce the cost of the expensive Ni or Co metal, improve electrochemical as well as the structural stability. Substitution of Li^+ in $LiNi_{1/2}Mn_{3/2}O_4$ (LNMO) with Na^+ ions, the $Na_{2/3}[Ni_{1/3}Mn_{2/3}]O_2$ cathode material was expected as a promising multi-metal oxide for Na-ion batteries.[78] The material displayed a reversible capacity of 86 mAh g^{-1} at low current rate (0.1C). But, at an elevated current rate (1C), the specific capacity of $Na_{2/}3[Ni1_{/3}Mn_{2/3}]O_2$ dropped to 77 mAh g^{-1} due to the slow solid-state Na-ion diffusivity. $NaTi_{1/2}Ni_{1/2}O_2$ was explored as a titanium-based cathode material for Na-ion batteries.[79] It exhibited a reversible capacity of 121 mAh g^{-1} at 0.2 C. Nevertheless, the cycling stability was poor (almost 40% fading after 100 cycles).

Metal fluoride (MF_x, M = Ni, Mn, and Fe) cathodes were recently developed mainly due to their high operation voltage as cathode materials for Na-ion batteries.[80] For instance, $NaFeF_3$ fluoroperovskite cathode showed several advantages, including a high theoretical capacity of 197 mAh g^{-1} for one electron per iron center (Fe^{3+}/Fe^{2+}), low cost, and intrinsically high oxidative stability.[79, 81-82] Upon electrochemical charging in Na-containing electrolytes, Na^+ can be deintercalated from the $NaFeF_3$ structure, forming a FeF_3 phase.[83] However, there are still a number of obstacles before it can be practically used. The foremost issue is its high electrical resistance as a result of the metal−fluoride bond, leading to a poor rate capability. At worst, ionic fluorine is toxic and corrosive to Na-ion cells, especially for a long-term cycling.

Compared to these types of cathodes above, the bare sodium-free transition-metal oxides (MO_x, M= V, Mn, and Fe) have been suggested as promising cathodes for Na-ion

batteries due to ease of synthesis and low cost.[84-86] Vanadium pentoxide (V_2O_5) has been investigated as a cathode for Na-ion batteries due to its high theoretical capacity (236 mAh g^{-1}), a unique layered structure, low cost, and abundant sources. It has been reported that V_2O_5 can host reversible Na-ion insertion/extraction.[87] However, the major problem of crystalline V_2O_5 cathodes is the slow Na-ion diffusion in the compact crystal structure and the low electronic conductivity, resulting in a low specific capacity in fast charging and discharging process. Manganese dioxides (MnO_2) have a larger open tunnel than that of crystalline V_2O_5 and provide interstitial spaces for Na-ion storage and transport.[88] Some phases of manganese oxides (MnO_2) can reversibly store Na-ion within a reasonably voltage range. However, the product of electrochemical reaction, $NaMnO_2$, is not thermodynamically stable, generating safety concerns.[89] Table 3 shows properties of other types of current cathode materials for Na-ion batteries.[61-62, 90]

1.4 Iron Hydroxide/Oxide Cathodes for Na-Ion Batteries

The application of iron-based materials as cathodes for Na-ion batteries is derived from their applications in Li-ion batteries. Iron is the fourth abundant element in the earth crust (5%). Due to its abundance, it has a much lower cost (~$70 per metric ton) than other 3d metal oxides such as Co (~$70,000 per metric ton) and Ni (~$13,800 per metric ton).[91-93] Therefore, iron-based materials have attracted significant interest as potential cathode materials in Li-ion batteries. As shown in Table 4, the research is mainly focusing on iron oxides (Fe_2O_3 and Fe_3O_4) and iron-based hydroxides.[94]

Fe_2O_3 includes two phases, α-Fe_2O_3 and γ-Fe_2O_3. Iron-based hydroxides are comprised of two classes: oxyhydroxides (α-FeO(OH), β-FeO(OH), γ -FeO(OH), δ-FeO(OH), amorphous FeO(OH) and hydroxides ($Fe(OH)_2$ and $Fe(OH)_3$).[95-96] As

cathodes, insertion of Li^+ into iron-based materials is associated with the $Fe^{2+/3+}$ redox couple. Table 4 shows iron hydroxide/oxide materials and their electrochemical performances as cathodes for Li-ion batteries. It has demonstrated that iron-based materials show reasonable specific capacities at low current rates within voltage window of 1.5-4.3V vs Li metal.[68-77]

Table 3. Examples of current cathode materials for Na-ion batteries[34,46,60]

Compound	Type	Theoretical capacity (mAh g^{-1})	Redox pair
$NaCrO_2$	Single transition-metal oxides	250	Cr^{3+}/Cr^{4+}
$NaFePO_4$	Olivines	173.8	Fe^{2+}/Fe^{3+}
$Na_3V_2(PO_4)_2F_3$	Sodium vanadium fluorophosphates	128	V^{3+}/V^{4+}
Na_2FePO_4F	Layered sodium iron fluorophosphates	124	Fe^{3+}/Fe^{4+}
$Na_3V_2(PO_4)_3$	NASICON-type materials	117.6	V^{3+}/V^{4+}
VO_2	Metal oxide	323	V^{3+}/V^{4+}
$Fe[Fe(CN)_6$	Prussian blue	200	Fe^{2+}/Fe^{3+}
$Na_2FeP_2O_7$	Pyrophosphates	97	Fe^{2+}/Fe^{3+}
FeO_x	Metal oxide	232-336	Fe^{2+}/Fe^{3+}

Learning from cathode development in Li-ion batteries, iron hydroxide/oxide materials are expected to be good candidate cathode materials for Na-ion batteries because of their low-cost, low toxicity and high theoretical capacities. Table 5 shows theoretical capacities and electrochemical equations of representative iron-based materials. However, iron hydroxide/oxide materials exhibited experimental low specific capacities and significant degradation mainly due to the intrinsic low electronic conductivity, and

slow solid-state Na-ion diffusion.[97] For example, Komaba et al. reported that evaluation of Fe_3O_4 nanoparticle cathodes for Na-ion storage.[86] Three electrode cells were set up using Li metal as a reference electrode, mixture of casted acetylene black and PVDF as a counter electrode, and active material, Fe_3O_4 nanoparticles, as a working electrode. As a Na-ion electrolyte, 1 M $NaClO_4$ dissolved EC/DMC as the Na^+ containing electrolyte was used. The reference section filled with the 1 M $LiClO_4$ electrolyte was separated from the working/counter compartment by using a glass filter. The results showed that

Table 4. Representative iron-based materials and their electrochemical performances as cathodes for Li-ion batteries.[68-77]

Materials	Morphology	Specific capacity (mAh g^{-1})	Current	Voltage potential (V vs. Li)
γ-Fe_2O_3	Nanoparticles	~150	8 mAg^{-1}	1.3-4.3V
Fe_3O_4	Nanoparticles	~200	20 mAg^{-1}	1.5-4.3V
α-Fe_2O_3	Nanoparticles	~177	0.54 mA cm^{-3}	1.5-4.3 V
γ-Fe_2O_3	Nanoparticles	~ 15	20 mAg^{-1}	2.0-4.1V
γ-Fe_2O_3	Nanosheets	~150	30 mAg^{-1}	1.5-4.2V
γ-Fe_2O_3	Hollow nanoparticles	~145	30 mAg^{-1}	1.5-4.5V
β-FeO(OH)	Tunnel	~275	0.1 mA cm^{-2}	1.5-4.2V
β-FeO(OH)	Nanorods	~250	0.2 mA cm^{-2}	1.5-4.2V
γ-FeO(OH)	Nanoparticles	~175	1A g^{-1}	1.3-4.3V
Amorphous FeO(OH)	Nanoparticles	~100	30 mAg^{-1}	1.5−4.5 V

within the voltage window between 1.5-4.0V vs Li, the specific capacity of Fe_3O_4 nanoparticles was 100 mA g^{-1} initially at the current of 20 mA g^{-1}. But after 10 cycles,

Table 5. Theoretical capacities and electrochemical equations of representative iron-based materials using a one-electron process

Materials	Type	Electrochemical equations for Na-ion storage	Theoretical capacity (mAh g^{-1})
α-Fe_2O_3 γ- Fe_2O_3	Iron oxide	$Fe_2O_3 + xNa^+ + xe^- \leftrightarrow Na_xFe_2O_3$	336
Fe_3O_4	Iron oxide	$Fe_3O_4 + Na^+ + xe^- \leftrightarrow Na_xFe_3O_4$	232
α-FeO(OH) β-FeO(OH) γ-FeO(OH) δ-FeO(OH) FeO(OH) $Fe(OH)_3$	Oxyhydroxides/ hydroxides	$FeO(OH) + Na^+ + xe^- \leftrightarrow Na_xFeO(OH)$	301

the capacity degraded to 50 mAh g^{-1}, attributing to the large Na^+ pulverizing the Fe_3O_4 structure. Later, γ-Fe_2O_3 nanoparticles were studied as cathodes for Na-ion batteries.[98] Iron oxide (γ-Fe_2O_3) nanoparticles showed a very low Na-ion discharge capacity of 32 mAh g^{-1} at a high current rate of 3A g^{-1} within voltage range of 1.1- 4.0 V, which may be related to the poor electronic conductivity of iron oxide that impedes the potential application of high-rate cathodes for Na-ion batteries. In order to channel Na^+ ions transport and insertion, tunnel type oxide/hydroxides, akaganeite, β-FeO(OH), was used as cathodes for Na-ion storage.[60] Initially, the specific capacity of β-FeO(OH) was near 200 mAh g^{-1} at the current of 30 mA g^{-1} within the voltage potential between 1.1-4.0 V vs. Na. However, the capacities significantly decreased to 75 mAh g^{-1} after 50 cycles.

Generally, when working as cathode materials for Na-ion batteries, iron-based materials usually exhibit lower specific capacities and much faster capacities fading with

comparison to their Li-ion counterparts. Furthermore, the problems of iron-based materials, such as a low electronic conductivity, irreversible phase transformation during ion insertion, and slow solid-state ion diffusion become more significant when being utilized for Na-ion storage.

1.5 Effective Strategies to Improve Na^+ Insertion Kinetics

The electrochemical performance of battery cathode materials is strongly influenced by several factors such as particle size, composition, morphology, electrochemical potential, and crystallinity. Therefore, many efforts have been made to optimize the performance of active positive materials for Na-ion storage via adjusting these parameters.

1.5.1 Effect of Particle Size on Na-Ion Storage and Transport within Active Materials

The importance of particle size has been acknowledged because it was found that nano-size electrode materials had superior properties than bulk micro-size electrodes.[99] Extensive studies have illustrated advantages of active electrodes with the small particle size.[100] At first, cathode materials with small particle sizes can reduce the diffusion or transport distance of Na^+ and electrons accompanying Na-ion insertion and extraction reactions, leading to a better rate capability. In addition, decreasing the particle size of active materials can increase the surface/volume ratio as well as surface area. Electrode materials with a large surface can have more active sites storing Na-ion, contributing to a higher specific capacity.[101]

Prior studies have revealed that cathodes with smaller particle sizes usually deliver high specific capacities as a result of better accessibility for Na^+ ion to the cathode

surface.[11] For instance, Komaba et al. found that enhancement of surface area of Fe_3O_4 nanoparticles by decreasing particle sizes could improve their discharge specific capacities.[86] Fe_3O_4 nanoparticles with three different sizes (400 nm, 100 nm, and 10 nm) were synthesized and characterized by the nitrogen physical adsorption (BET) method. Compared to particles with the largest size (400 nm), the surface area of 10 nm Fe_3O_4 nanoparticles was three times higher, about 202 $m^2 g^{-1}$. From the results of galvanostatic tests (Figure 4), among these three samples, the electrochemical activity of 400 nm Fe_3O_4 nanoparticles was worst. The 100 nm Fe_3O_4 nanoparticles exhibited the medium electrochemical performance, whereas the crystallized Fe_3O_4 nanoparticles with a small size of 10 nm delivered a highest specific capacity (145 mA g^{-1}) for the first cycle.

Similarly, the electrochemical properties of crystalline α-Fe_2O_3 nanoparticles exhibited size dependency.[86] The specific capacity of 10 nm crystalline α-Fe_2O_3 demonstrated a high specific capacity of 200 mAh g^{-1} within a voltage range of 1.2-4.0 V vs. Li using a PC/$NaClO_4$ electrolyte.

However, a large surface cannot improve the intrinsic low electronic conductivity of most iron-based materials, therefore the high specific capacity can be obtained only at low current rate; at high current rate the specific capacity will still be poor. Moreover, it has been reported that because of the large specific surface area, nanocrystalline electrode materials usually suffer from a decreased energy density, cycling stability, and effective electrode capacity.[102]

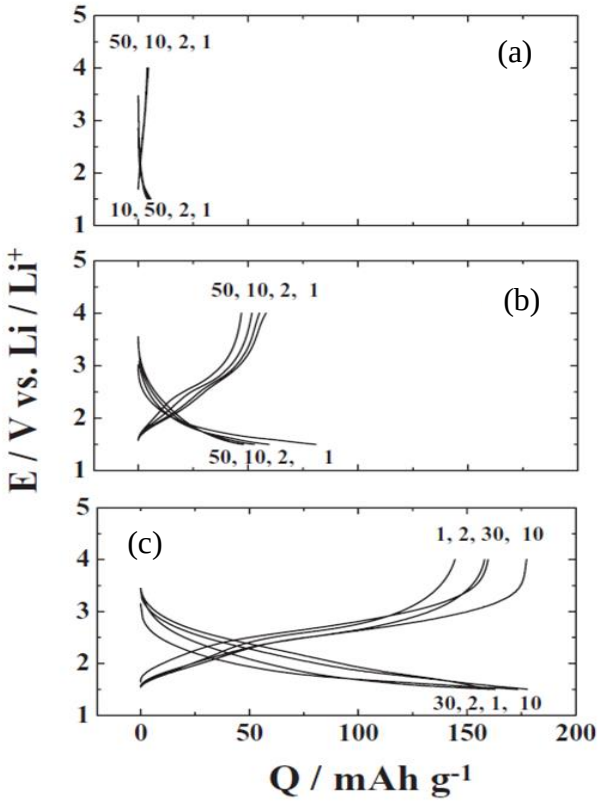

Figure 4. Charge and discharge curve of (a) 400, (b)100, (c)10 nm Fe_3O_4nanoparticles at the current rate of 20 mA g^{-1}. The electrolyte is 1 mol dm^{-3} $NaClO_4$ dissolved in ethylene carbonate (EC): dimethyl carbonate (DMC).[81]

1.5.2 Effect of Morphology on Na-Ion Storage and Transport within Cathode Materials

Another critical factor that has been demonstrated to significantly affect the Na-ion storage and transport of active materials is the morphology. So far, iron hydroxide/oxide with several different nanostructures have been prepared, including nanoparticles,[103] nanoplates,[104] nanosheets,[105] nanotubes,[106] hollow structure,[107] and 3D nanoflowers.[108] Among these types of nanostructures, two-dimensional (2D) nanosheets and hollow structures have received particular interest because of their unique benefits for Na-ion storage and transport.

The original concept of 2D nanosheets comes from graphene nanosheets. However, the family of 2D materials has grown steadily and is no longer limited to only graphene nanosheets.[109] With unique physical and chemical properties, 2D nanosheets, particularly the 2D transitional metal hydroxide/oxide nanosheets, have exhibited superior advantages as applications in energy storage devices. 2D nanosheets exhibit the property of quantum confinement that can result in orders of magnitude higher electronic conductivities, which specially benefits the electron transport with 2D transitional metal hydroxide/oxide nanosheets, typically having a low poor electronic conductivity.[110] Furthermore, ultrathin 2D nanosheets exhibit surface storage kinetics, being enabling Na-ions to be stored on the surface of active materials rather than by diffusion into materials. As discussed above, a large radius of Na^+ usually results in significant volume expansion and lattice twist, causing serious capacity degradation upon cycling. Therefore, charging Na-ion on the surface can improve the structural stabilization and have a better cycling stability since Na^+ do not intercalate/deintercalated into electrodes. Moreover, 2D nanosheets with a large surface area can be accessible to Na-ion efficiently.[111] Zhang et al. reported that amorphous $FePO_4$ nanosheet cathodes exhibited good electrochemical properties for Na-ion storage.[112] At a low current rate of 20 mA g^{-1}, $FePO_4$ nanosheets delivered a high discharge capacity of 126.4 mAh g^{-1} for the first cycle, superior cycling performance (89.8% capacity retention over 100 cycles), and high rate capability (42.1 mAh g^{-1} at 1000 mA g^{-1}).

Besides the sheet-like nanostructure, hollow structures are even more appealing to channel Na-ion transport compared to other morphologies. Hollow nanostructures used as electrode materials for Na-ion storage offer more accessible storage sites and larger

electrode/electrolyte contact area, thus higher specific capacities. In addition, the interior void space can buffer the destructive volume expansion and alleviate stress/strain produced during cycling, resulting in improved cycling stability.[113] More importantly, the character of the hollow structure can help to transport Na^+. Koo et al. prepared both solid and hollow γ-Fe_2O_3 nanoparticles and compared their electrochemical properties.[98] As shown in Figure 5, at a current rate of 3000 mA g^{-1}, solid γ-Fe_2O_3 nanoparticles showed only a low specific capacity of less than 30 mAh g^{-1} whereas hollow nanoparticles delivered a much higher capacity of ~ 75 mAh g^{-1}. These results demonstrated that the hollow structure is beneficial for achieving a better rate capability as well as enhancing the specific capacity. In addition, Wang et al. reported hollow α-Fe_2O_3 nanospheres obtained a high discharge capacity of 837.3 mAh g^{-1} tested as anodes.[114] The materials were synthesized by a carbon-template method.

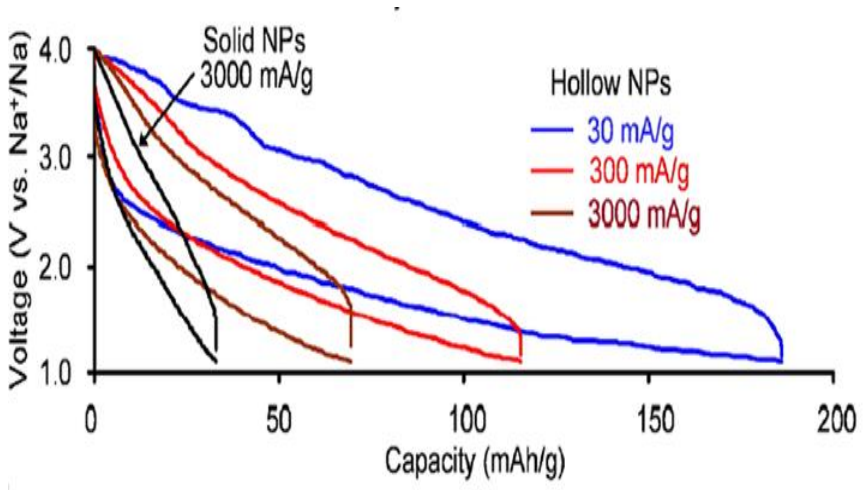

Figure 5. The comparison of rate study for hollow nanoparticles and solid nanoparticles. Cells were operated within the voltage range of 1.1-4.0V. The electrolyte is 1 M $NaClO_4$ in propylene carbonate (PC).[92]

1.5.3 Effect of Composition of Active Materials on Sodium-Ion Storage, Structural Stabilization, and Electron Transport

Due to most iron-containing active materials showing a very low electronic conductivities, integration with carbon-based materials has become an effective method to improve electron transport. For instance, in order to improve the electrochemical activity during the fast charge and discharge process, studies have focused on development of iron-based nanocomposite materials with carbon nanotubes (CNTs). Koo et al. first reported taking advantage of carbon nanotubes to increase the rate capability of iron oxide (γ-Fe_2O_3) hollow nanoparticles.[98] With carbon nanotubes, the specific capacities and cycling stabilities dramatically improved, especially at high current rate, compared to the pure γ-Fe_2O_3 hollow nanoparticles (as shown in Figure 6) due to the enhanced electronic conductivity. Nevertheless, an unusual phenomenon that the specific capacity increased upon cell cycling instead of decreasing occurred, indicating a side reaction rather than the electrode itself contributing to the high electrochemical activity. In other studies, β-FeOOH/CNTs cathodes for Li and Na-ion storage were evaluated, repectively.[60, 115] Similarly, the β-FeOOH/CNTs nanomaterials showed much better electrochemical properties than that of bare β-FeOOH as a result of significantly enhanced electronic conductivity (from 2×10^{-6} to 3 S cm^{-1}).[115] However, the strategy of modification of iron-based materials with CNTs needs to overcome the hydrophobic properties of sidewalls of CNTs.[116]

In order to make iron-based materials grow on CNTs or seamless combination, the surface of CNTs needs to be further modified with a strong acid, for instance, HNO_3,

which leads to complex synthesis routes, extra pollution, and costs. Therefore, it is of great necessity to design iron-based nanomaterials for Na-ion batteries that provide the improved electrochemical performance.

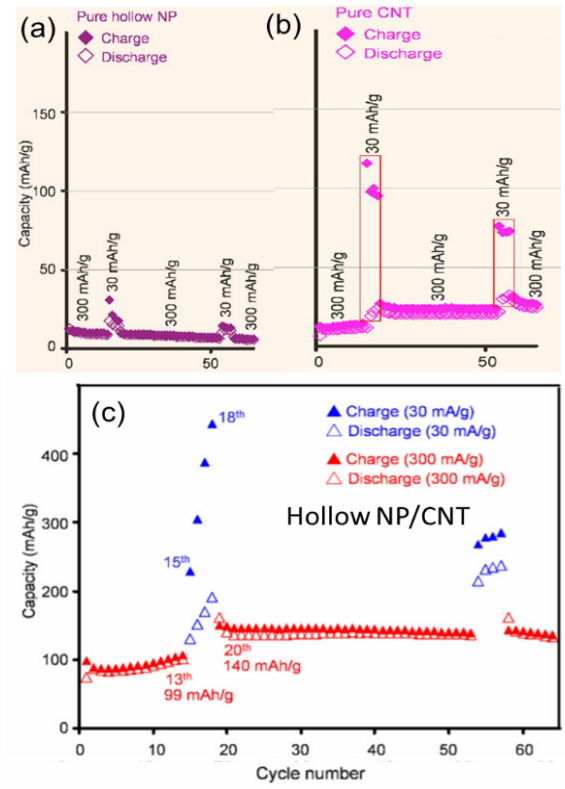

Figure 6. The comparison of rate study for pure hollow nanoparticles, pure CNT, and hollow nanoparticles/CNT. Cells were operated within the voltage range of 1.1-4.0 V. The electrolyte is 1 M $NaClO_4$ in PC.[92]

Besides carbon nanotubes, reduced graphene nanosheets have been extensively explored as conductive materials integrated into iron-based materials. Graphene, an atomically thin two-dimensional carbonaceous material, has attracted tremendous attention in the scientific community, due to its exceptional electronic, electrical, and mechanical properties.[117] It can be produced by exfoliation of highly ordered graphite, epitaxial growth, chemical vapor deposition, and reduction of graphene oxide (GO).[118] Similar to graphene, reduced graphene oxides (rGO) exhibit the sheet-like structure and

have a high electronic conductivity. But, different from graphene and carbon nanotubes, the surface of rGO has functional groups, including carboxyl, hydroxyl, and ester groups.[119] Therefore, rGO is hydrophilic and can form stable aqueous colloids that facilitate the assembly of macroscopic structures by simple and inexpensive solution processes. Moreover, these functional groups can avoid graphene sheets restacking after thermal treatment and retain a high surface area. The high electronic conductivity of rGO facilitates electron transport of iron-based materials and the large surface area as well as "flexible confinement" function help iron-based materials to deliver high specific capacity without significant the volume change and prevent electrodes detachment and agglomeration.[120] Because of these superior properties, rGO nanosheets were incorporated into iron fluoride (FeF_3), and FeF_3/rGO delivered a substantially enhanced discharge capacity of 266 mAh g^{-1} compared to 158 mA h g^{-1} of the bare FeF_3 due to a larger surface area, better Na-ion transport, and higher electronic conductivities.[121] Liu et al. prepared $FePO_4$/rGO nanocomposites as cathodes for Na-batteries via directly growing $FePO_4$ nanospheres on each side of the rGO nanosheets.[122] $FePO_4$/rGO cathodes exhibited a very cycling stability with a high specific capacity of 153.4 mAh g^{-1} after 70 cycles at 0.1C. In addition, the discharge-specific capacity of $FePO_4$/rGO was maintained at 154.5 mAh g^{-1}, 151.6 mAh g^{-1}, 122.3 mAh g^{-1} and 100.6 mAh g^{-1}, at 0.1C, 0.2C, 0.5C and 1C, respectively. The excellent rate capability was attributed to the rGO in as-prepared $FePO_4$/rGO nanocomposites, which provided a high-speed pathway for electron transfer.

In order to obtain iron-based/rGO nanocomposites with good electrochemical

activity, the interface between iron-based nanomaterials and rGO is an essential factor that affects the Na-ion charge transfer process and electron transport. Instead of physically mixing or dispersing rGO with iron-based materials, which leads to poor interfacial interactions, anchoring and growing iron-based materials directly on the surface of rGO have become common strategies to increase interfacial interactions and achieve well-defined uniform structures by covalent and/or noncovalent bonds.[123-124] Oxygen-containing functional groups on rGO ensure good interfacial interactions and electrical contacts between rGO and iron-based materials, thus having synergistic effects on ions storage.[124] Besides that, rGO provides a two-dimensional support for uniformly nucleating, growing or assembling iron oxides and/or iron hydroxides with well-defined size, shape, and crystallinity. Iron-based materials growing between the layers of rGO can efficiently suppress the re-stacking of rGO nanosheets.[125]

There are several methods to grow iron-based materials on rGO nanosheets, such as hydrothermal, co-precipitation, microwave heating, self-assembly method, and electrochemical approach. [99-105] Typical examples are listed in Table 6. Among these methods, hydrothermal synthesis is a conventional way to produce iron oxides/hydroxides and rGO nanocomposites in aqueous and/or organic solution under a certain amount of pressure and temperature. The advantages of hydrothermal synthesis involve mild conditions (below 200 °C) and large scale, resulting in potential applications in industry.[126] The reaction medium is a key component in the hydrothermal process. Reaction media with diverse physical and chemical functions (e.g. boiling temperature, polarity, function groups) can significantly affect the solubility, reactivity, and diffusion behavior of reactants.[127] Thus, the morphology, phase, and content of components can be

adjusted by controlling the mass ratio of iron salt and rGO in reactant, reaction time, temperature, and reaction media.

Table 6. A summary of the representative iron oxide and iron oxyhydroxides with rGO composites.[99-105]

Composition	Synthetic method	Iron salt	Application
α-Fe_2O_3/rGO	Hydrothermal	$FeCl_3 \cdot 6H_2O$	Supercapacitor
Fe_3O_4/rGO	Hydrothermal	$FeCl_3 \cdot 6H_2O$	Biosensor
Fe_3O_4/rGO	Hydrothermal	$FeCl_3 \cdot 6H_2O$ and $FeCl_2 \cdot 4H_2O$	Supercapacitor
Amorphous FeO(OH)/rGO	Co-precipitation	$FeCl_3 \cdot 6H_2O$	Supercapacitor
Fe_3O_4/rGO	Co-precipitation	$FeSO_4 \cdot 7H_2O$	Electromagnetic wave absorption
γ-Fe_2O_3/rGO	Microwave	$Fe(acac)_3$	Li-ion batteries (anode)
Fe_3O_4/rGO	Thermal decomposition	$Fe(NO_3)_3 \cdot 9H_2O$	Li-ion batteries (anode)

1.5.4 Na-ion Diffusion and Effect of Cation Defects on the Na-Ion Charge Storage Property of Iron Hydroxide/Oxide Cathodes

As mentioned above, the electrochemical performance of cathode materials for Na-ion batteries is strongly influenced by both Na-ion diffusivity and electronic conductivity. In particular, the efficiency of Na-ion diffusion involves three Na-ion transfer processes, including Na-ion conduction in liquid electrolytes, Na-ion transfer at the electrolyte/electrode interface, and Na-ion diffusion in solid electrodes, which is the rate limiting step when Na-ion cells are charged/discharge at high current rates.[128] Generally, the most basic model for ion diffusion within solids is to assume that they

move by a series of random jumps, called the random-walk diffusion model, as described by the following equation:[129]

$$< x^2 > = na^2 = \Gamma t a^2 \quad (14)$$

where $< x^2 >$ is the average of the square of the distance that each of the N diffusing atoms reaches after carrying out n random steps over the time of the diffusion experiment *t*. Each jump is of the same distance, a, and Γ is the frequency with which each atom jumps to the next position.

Vacancy diffusion is one type of random-walk diffusion, where vacancies are in the form of defects. Defects mainly include cation vacancies, dislocations, interstitials, stacking faults, and grain boundaries. Among them, cation vacancies can directly affect intercalation of alkali-ions into iron-based nanomaterials through creating extra sites to accommodate alkali-ion and elevate the ion-insertion potential.[130] Substitution of a fraction of Fe^{3+} ions with metal cations of higher oxidation state, such as Mo^{6+} or V^{5+}, increased cation vacancies of γ-Fe_2O_3.[131] Even though there have been some work on investigation of the effect of cation vacancies on Li-ion storage, so far, only Chervin et al. reported iron oxide aerogels were substituted with vanadium (V^{5+}) and annealed at different atmosphere (Ar/O_2). The resulting materials exhibited a specific capacity of 70 mAh g^{-1} within a higher intercalation potential (1.7-3.7 V vs. Na) for Na^+ insertion.[132-133] This pioneering study demonstrated that increasing concentrations of cation defects consequently improved their specific capacities for Na-ion storage.

1.5.5 Effect of the Degree of Structural Order on Electrode Performance

1.5.5.1 General Studies on Effect of Structural Order on Electrode Performance

Amorphous materials, also known as glassy materials, are composed of atoms in a random sequential arrangement without the long-range order in their atomic packing.[134] In amorphous/low crystalline transitional metal hydroxides/oxides, metal-oxides (M-O) or metal-hydroxyl (M-OH) polyhedra, basic building components, are randomly arranged rather than maintaining perfect periodicity.[135] By contrast, in crystalline materials, polyhedral building blocks are interconnected via different types of configurations, including edge sharing, corner sharing, and face sharing of oxygen atoms.[136] The disordered structure reduces scattering mean free path and grain boundaries within materials.

It has been widely accepted that the performance of insertion electrode materials is highly dependent on the structural crystallinity.[137] Crystalline materials have been the main candidates investigated for energy storage applications, because their ordered structures can offer higher electronic conductivities.[138] However, storage capacities delivered by electrode materials are crucially dependent on various factors, including the structural stability, phase transitions, and ion diffusivity. In recent years, there are numerous reports pointing out advantages of amorphous nanomaterials over the crystalline counterparts in energy storage application.[139] It has been reported that inherent disorderliness in the structural arrangement is highly constructive to improving the alkali ion diffusion through the lattice.[140] In addition, a well-crystallized structure has a difficulty in expanding or contracting, limiting the ion diffusivity and reversibility.[141]

1.5.5.2 Effect of Structural Order on Na-Ion Charge Transport Within Iron-Based Cathodes

Amorphous active materials exhibit noticeable advantages with respect to Na-ion charge storage. Active materials that have an amorphous structure or short-range order can enhance Na-ion diffusion via more open active diffusion channels and random structures, leading to higher capacities.[142-143] Furthermore, amorphous electrode materials benefitting from a flexible lattice structure can accommodate lattice distortion and/or volume expansion upon large size Na-ion intercalation/deintercalation, resulting in a better cyclic stability.[139, 144]

Up to now, there have been many studies involving amorphization of iron-based cathode materials as Na-ion hosts to optimize their electrochemical activities. Zhang et al. reported that amorphous iron trifluoride (FeF_3) and carbon nanocomposites as cathodes for Na-ion batteries exhibited a high discharge capacity (~73 mAh g^{-1}) at a superior high current rate of 1500 mA g^{-1} and good cycling performance with a ~127 mAh g^{-1} at 75 mA g^{-1} after 100 cycles. The high electrochemical activity might be partially attributed to their amorphous structures, leading to a high Na-ion diffusivity.[145] Ma et al. prepared amorphous and crystalline $FeVO_4$ nanoparticles via the electrostatic spray assisted coprecipitation method.[138] Figure 7 shows that $FeVO_4$ cathodes with an amorphous nature demonstrated a much better cycling stability compared to highly crystallized counterparts due to a faster Na-ion transport evaluated by the impedance analysis. Moreover, extensive studies on $FePO_4$ cathodes showed that the amorphous structure was beneficial to Na-ion diffusion and diffusion and obtained improved electrochemical performance compared to that of crystalline phase.[112, 144, 146-148] Besides iron-based

cathodes, it has been demonstrated that other nanosized transitional metal oxides, such as manganese dioxide (MnO_2),[149] vanadium pentoxide (V_2O_5),[150] and sodium cobalt oxide ($NaCoO_2$),[151] also benefit from the amorphous structure for Na-ion transport and storage. Therefore, it is worthwhile to investigate the effect of structural disorder on the Na-ion storage of iron hydroxide/oxide cathodes as an avenue to enhance the electrochemical performance.

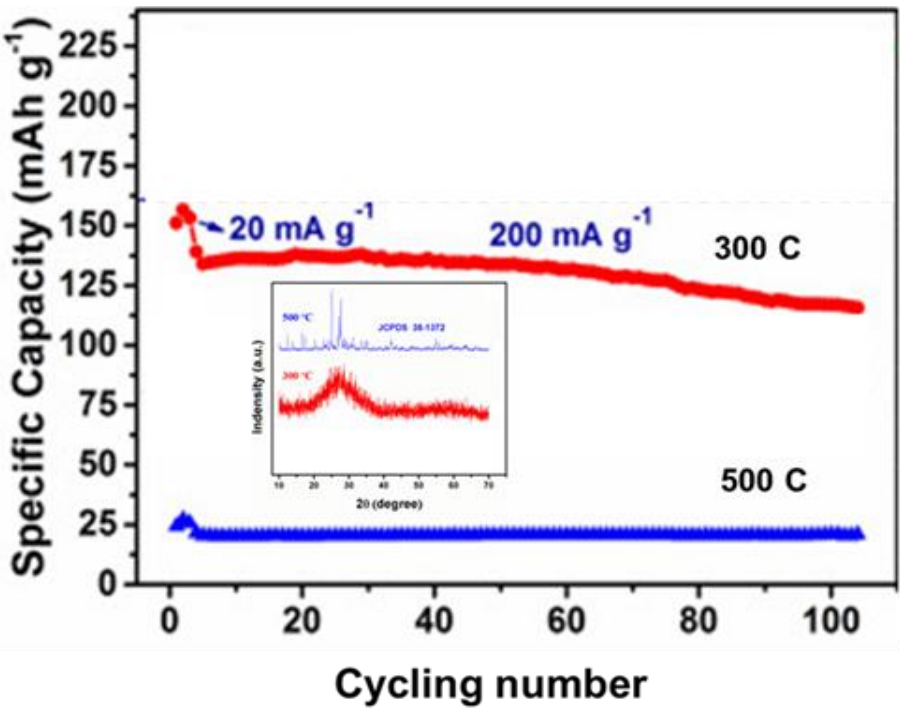

Figure 7. Comparison of cycling stability of amorphous and crystalline $FeVO_4$ nanoparticles. The inset shows the XRD patterns of two electrodes.[130]

1.6 Structure, Properties, and Synthesis of Iron(III) Hydroxide ($Fe(OH)_3$)

Among the phases of iron hydroxides/oxides, iron (III) hydroxide, $Fe(OH)_3$, has a naturally amorphous/low crystalline structure.[152-153] Hydrate iron oxyhydroxides, $Fe(OH)_3$, have a orthorhombic structure (a = 7.54 Å, b = 7.56 Å, and c = 7.56 Å), shown in Figure 8.[95] Due to the poor crystallinity of $Fe(OH)_3$, there are only few studies involving examination of crystal structure. Shinoda et al. studied the local structure of $Fe(OH)_3$

powder via X-ray scattering and EXAFS methods.[154] It was found that $Fe(OH)_3$ structure was composed of FeO_6 octahedra, which were connected with the edge and double-corner sharing linkage, shown in Figure 9. McCammon et al. reported that within $Fe(OH)_3$, the octahedra coordinate together.[155] Within $Fe(OH)_3$, the bond length of Fe-O range from 1.98 to 2.04 Å, and the O-Fe-O bond angles vary between 86.0 and 90.4°.

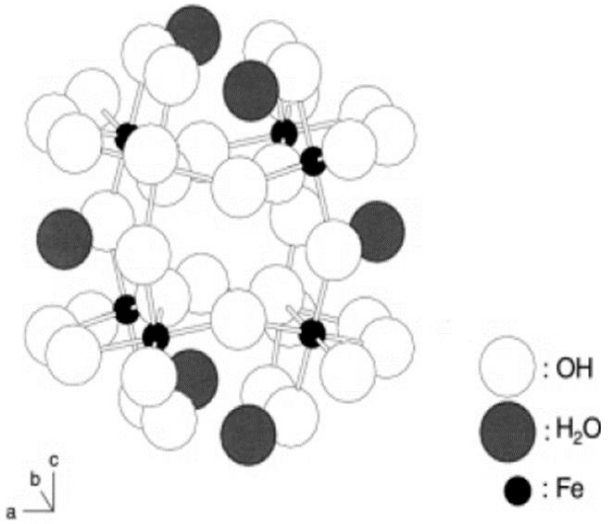

Figure 8. Ball-and-stick model of $Fe(OH)_3 \cdot H_2O$ crystal.[90]

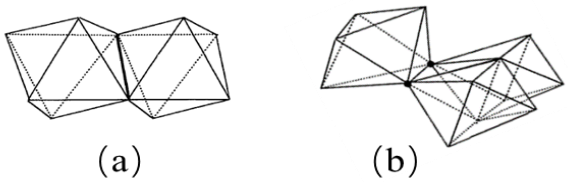

Figure 9. The illustration of the local arrangements of the FeO_6 octahedra in $Fe(OH)_3$; (a) edge, (b) double-corner sharing linkages.[145]

Amorphous $Fe(OH)_3$ is thermodynamically unstable and can transform to crystalline α-FeOOH or α-Fe_2O_3 phases at high temperatures.[156] Popov et al. investigated the effect of thermal treatment on the phase transformation of $Fe(OH)_3$ with addition of organic solvents.[157] It was shown that at a relative low temperature (~120 °C), $Fe(OH)_3$

converted into poorly crystallized materials. By contrast, when temperature was elevated to 180 °C, the obtained materials were well indexed with crystalline α-Fe_2O_3. The fundamental mechanism involves the internal rearrangement and dehydration. It was also observed that organic solvents locally reduced the concentration of $Fe(OH)_3$, thereby preventing the formation of α-FeOOH crystallites and favoring the formation of α-Fe_2O_3 particles. Cornell et al. explored the crystallization of $Fe(OH)_3$ to either crystalline α-FeOOH or α-Fe_2O_3.[156] The formation of $Fe(OH)_3$ began at hydrolytic polymerization reaction from generation of original hexa-aquo ion, $Fe(H_2O)_6^{3+}$, to form hydroxo and oxo species. Then, with addition of base, when the ratio of OH^- to Fe^{3+} exceed three to one, the $Fe(OH)_3$ started to precipitate. Below shows the detailed mechanism of $Fe(OH)_3$:

$$Fe^{3+} + 6H_2O \rightarrow [Fe(OH_2)]^{3+} \quad (15)$$

$$[Fe(OH_2)_6]^{3+} + OH^- \rightarrow [FeOH(OH_2)_5]^{2+} \quad (16)$$

$$[Fe(OH_2)_6]^{3+} + H_2O \rightarrow [FeOH(OH_2)_5]^{2+} + H_3O+ \quad (17)$$

$$[FeOH(OH_2)_5]^{2+} + OH^- \rightarrow [Fe(OH)_2(OH_2)_4]^{+} \quad (18)$$

$$[Fe(OH)_2(OH_2)_5]^{+} + OH^- \rightarrow [Fe(OH)_3(OH_2)_3] \quad (19)$$

The evolution of α-Fe_2O_3 phase from $Fe(OH)_3$ was proposed by removal of a proton from an OH^- group followed by migration of this proton to combine with another OH^- group, consequently leading to elimination of one water molecule and formation of an oxo linkage. The proton loss is further compensated by migration and redistribution of Fe^{3+} within the cation sublattice. It was observed via X-ray adsorption spectroscopy that Fe-Fe bonds become shorter during the conversion to α-Fe_2O_3. Nevertheless, $Fe(OH)_3$ transformed to α-FeOOH via reconstructive transformation involving dissolution of $Fe(OH)_3$.

A few methods have been reported on synthesis of $Fe(OH)_3$. For example, Au-Yeung et al. prepared $Fe(OH)_3$ by oxidation of $Fe(II)SO_4$ with $[Co(III)(en)(dien)]_2O_2[ClO_4]_4$, $[Co(III)(tetraen)]_2O_2[ClO_4]_4$, and H_2O_2 in acid solution. The X-ray diffraction pattern of products showed very broad and low intense peaks, indicating that the obtained $Fe(OH)_3$ does not have a highly crystalline structure.[158] Instead of acidic environment, $Fe(OH)_3$ powders were produced in mild basic solution using $Fe(II)SO_4$ and $NH_3{\cdot}H_2O$ at a temperature of 60°C. The XRD spectra of as-prepared $Fe(OH)_3$ displayed only one weak adsorption peak at the 2θ degree of 45, suggesting the synthesized $Fe(OH)_3$ prefers to form a lattice without significant well-defined long-range order.[159] Du et al. reported a strategy to form $Fe(OH)_3$ sol by boiling Fe^{3+} salts in aqueous solution and gradually enucleating into $Fe(OH)_3$ sol.[160] Recently, Su et al. synthesized $Fe(OH)_3$ nanoparticles using $FeCl_3$ and urea as precursors through the hydrothermal synthesis in pure aqueous solution.[161] Urea, $CO(NH_2)_2$, here serves as a reservoir for providing OH^-. At a temperature above 80°C, urea reacts with H_2O and then decomposes into CO_2 and NH_3, which further form $NH_3{\cdot}H_2O$ with H_2O molecule. $NH_3{\cdot}H_2O$ then ionizes in water, generating OH^-.[162] On the other hand, CO_2 dissolved into water to form H_2CO_3, which is not stable and further ionizes to CO_3^{2-} and H^+. Therefore, hydrolysis of CO_3^{2-} generates OH^- as well. OH^- groups provide the alkaline condition for formation of $Fe(OH)_3$ with Fe^{3+}. The detailed reactions are shown below:[161, 163]

$$CO(NH_2)_2 + H_2O \xrightarrow{\Delta} CO_2 + 2NH_3 \tag{20}$$

$$NH_3 + H_2O \rightarrow NH_3{\cdot}H_2O \rightarrow NH_4^+ + OH^- \tag{21}$$

$$CO_2 + H_2O \rightarrow H_2CO_3 \tag{22}$$

$$H_2CO_3 \rightarrow CO_3^{2-} + 2H^+ \tag{23}$$

$$CO_3^{2-} + H_2O \rightarrow HCO_3^- + OH^- \quad (24)$$

Gulina et al. prepared $Fe(OH)_3$ microtubes in a mixed $FeCl_2/FeCl_3$ ascorbic acid water solution and then reacted with gaseous ammonium (NH_3).[164] $FeCl_2/FeCl_3$ reacted with NH_3 gas in aqueous solution to form $Fe(OH)_3$. However, so far comparatively no investigations have been concerned with urea dose on the phase formation and morphologic evolution of $Fe(OH)_3$.

$Fe(OH)_3$ have been reported as catalysis used to produce β-amino alcohols by reacting with various aryloxy, terminal, and meso epoxides with aromatic and aliphatic amines at room temperature due to hydroxide groups.[165] In addition, Baca et al. used $Fe(OH)_3$ as an absorbent to remove silica in waste water. Nevertheless, so far, no studies have been reported on the electrochemical properties of ferric oxyhydroxide, $Fe(OH)_3$, for alkali-ion batteries (Li- and Na-ion batteries).

1.7 Structure, Electronic Properties, and Synthesis of Hematite Phase Iron Oxide (α-Fe_2O_3) Nanoparticles and Iron Oxide (α-Fe_2O_3)/rGO Nanocomposites

1.7.1 Structure of Hematite (α-Fe_2O_3) and Transformation Upon Ion Diffusion

The detailed crystal structure of hematite, α-Fe_2O_3, was initially reported by Linus Pauling and Sterling Hendricks in 1925.[166] As shown in Figure 10, iron and oxygen atoms containing in α-Fe_2O_3 are arranged in a rhombohedrally-centered hexagonal closed-packed lattice (hcp) along the [001] direction.[167] The lattice parameter is a =b= 5.038 Å, c= 13.772 Å with space group $R\bar{3}c$.[168] In the perfect crystal, Fe atoms are surrounded by 6 oxygen neighbors. FeO_6 octahedra share edges with three neighboring octahedra in the same plane.[169] In amorphous α-Fe_2O_3, FeO_6 octahedra are distorted and form a network in a randomly ordered package. Prior studies reported that

structural order significantly affected electrochemical behaviors since Li^+ are sensitive to the local environment.[170] It was found that upon Li-ion intercalation, nanocrystalline α-Fe_2O_3 nanoparticles were probed to undergo a two-phase reaction at the local scale analyzed by the EXAFS data.[165] Specifically, the hexagonal closed-packed lattice transformed to the cubit structure with observed lattice distortion. Due to Li^+ and Na^+ share similar properties and Na^+ even have much large radius than that of Li^+, substantial lattice distortion and significant phase transformation is expected, leading to serious degradation of Na-ion storage capacity.

1.7.2 Electronic Properties of Hematite (α-Fe_2O_3) Nanoparticles

α-Fe_2O_3 is the most thermodynamically stable phase of iron oxides with a high resistance to corrosion, low cost, environmentally friendliness and non-toxicity.[171] α-Fe_2O_3 is a n-type semiconductor (E_g = 2.1 eV) with a very low electronic conductivity.[172]

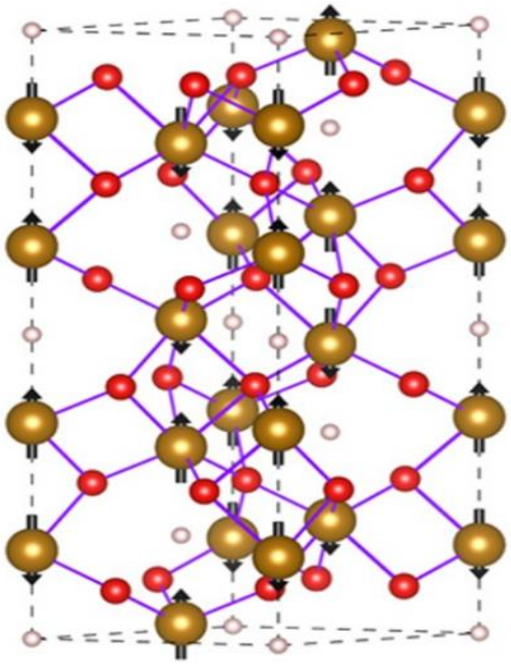

Figure 10. Hexagonal close–packed crystal structure of pure hematite. The gold yellow spheres represent Fe atoms, and red spheres indicate positions of O atoms. The octahedral holes are also drawn, which are represented by white spheres.[158]

Within α-Fe_2O_3, electrons are transported as described by the small polaron model where the movement of charge carriers is coupled to distortion of nearby atoms and charge carriers hop from sites to sites.[173] Prior studies showed that hematite acted as a Mott-insulator, which means that it poorly transported charge, even though it facilitates charge separation.[174]

Pant et al. studied the electronic conductivity of α-Fe_2O_3 nanocrystalline powder.[175] Crystalline α-Fe_2O_3 nanoparticles were prepared at different temperatures at 250 ºC, 350 ºC, 450 ºC, and 650 ºC via a simple chemical method. The obtained α-Fe_2O_3 nanoparticles had various sizes from 14 nm to 33 nm with enhanced reaction temperatures. The electronic resistance of α-Fe_2O_3 nanoparticles obtained at 450 ºC was measured to be 2.4×10^{7} Ω·cm ($\sigma = 4.2\times10^{-8}$ S cm^{-1}) by the two-probe method. Dawy et al. reported a similar result of electronic conductivity of α-Fe_2O_3 nanoparticles prepared by a hydrothermal approach.[176] The obtained raw materials were further annealed at 600 ºC for 2 h. The electronic conductivity of α-Fe_2O_3 nanoparticles was measured as 1.0×10^{-8} S cm^{-1}.[171]

1.7.3 Synthesis of Hematite (α-Fe_2O_3) Nanoparticles

The structure and properties of α-Fe_2O_3 are markedly influenced by the synthesis method. So far, extensive studies have worked on developing different strategies in order to obtain α-Fe_2O_3 with varied morphologies, degrees of structural order, and electric properties.[177] All these factors can greatly affect the electrochemical properties of α-Fe_2O_3. With respect to the degree of structural order of α-Fe_2O_3 nanoparticles, the reaction time, temperature, concentration of precursors, and the type of reaction play a critical role.

The primary methods of preparation of α-Fe_2O_3 nanoparticles are sol-gel synthesis, hydrothermal synthesis, precipitation, and microwave synthesis. Akbar et al. reported using a sol-gel method to synthesize α-Fe_2O_3 nanoparticles, which were prepared at a citric acid concentration of 0.2 M and 0.1 M iron nitrate with aging of the dry precursors at 90 ºC for about 16 hours.[178] The raw materials were subsequently annealed at different temperatures in the range 180 ºC to 400 ºC, producing similar particle sizes but showing large variation in the purity of α-Fe_2O_3 phase.[178] Similarly, Kopanja et al. synthesized α-Fe_2O_3 nanoparticles via a sol-gel method embedded in an amorphous silica matrix.[179]

Zhu et al. prepared α-Fe_2O_3 nanoparticles via a simple hydrothermal process using PVP (polyvinylpyrrolidone) as a surfactant and NaAc (sodium acetate) as a precipitation agent.[172] The obtained α-Fe_2O_3 have a narrow size distribution but different degrees of crystallinity. It was revealed that longer reaction time significantly increase the degrees of structures order, shown in Figure 11. Su et al. investigated the effect of reaction media and urea dose on the synthesis of α-Fe_2O_3 nanoparticles.[161] Pure crystalline α-Fe_2O_3 nanoparticles were formed via a hydrothermal process. In addition, it was found that the crystallinity of α-Fe_2O_3 nanoparticles were significantly enhanced as increasing dose of urea as one of precursors, which was shown in Figure 12. In addition to sol-gel and hydrothermal synthesis, precipitation is another strategy to prepare α-Fe_2O_3 nanoparticles. Lassoued et al. reported that pure α-Fe_2O_3 nanoparticles were synthesized with a chemical precipitation method.[180] In this reaction, precursors were

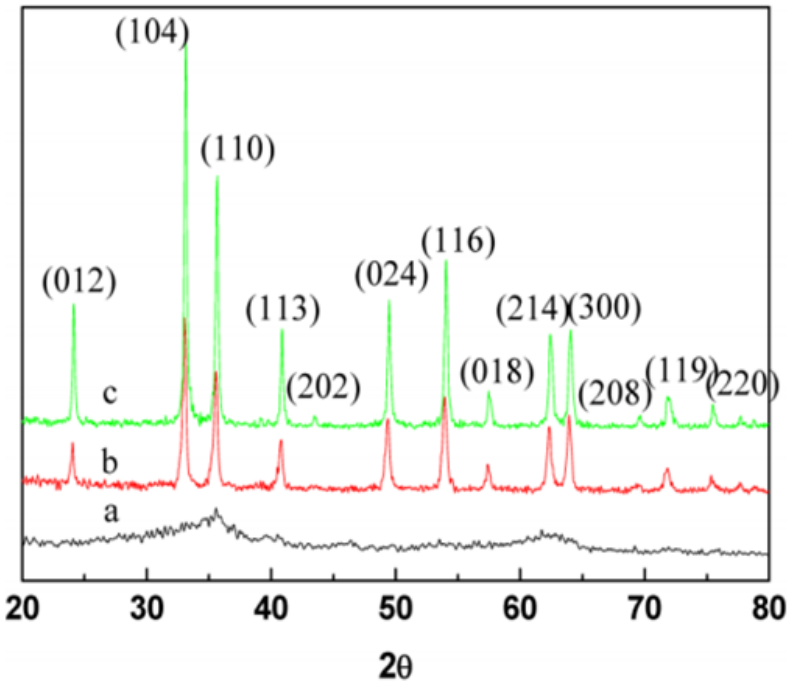

Figure 11. XRD patterns of resulting materials prepared at different reaction times: (a) 0.5, (b) 1, (c) 2 h.[163]

iron salt, $FeCl_3 \cdot 6H_2O$, and NH_4OH as a precipitation agent. The as-prepared materials were determined to be α-Fe_2O_3 with a high crystalline structure. Fouad et al. fabricated pure α-Fe_2O_3 nanoparticles with different degrees of crystallinity via a simple precipitation route by using different amount of ferric sulfate, $Fe_2(SO_4)_3 \cdot xH_2O$ precursor and ammonium hydroxide (NH_4OH) precipitant.[181] According to the XRD analysis, increased amount of urea improved the crystallization of as-prep α-Fe_2O_3.

Microwave synthesis has received much interest as a method to quickly obtain α-Fe_2O_3. The wavelengths of microwave are 1m to 1mm depending on their frequencies. The degree of interaction of microwaves with a dielectric medium is related to the dielectric constant and dielectric loss of materials.[182] There are several benefits of microwave synthesis compared to traditional synthesis strategies. At first, microwave irradiation can heat a substance uniformly, resulting in homogeneous nucleation and

crystallization. In addition, since microwave reaction only takes a few minutes, the fast heating can result in small particle sizes with high surface area but avoiding formation of intermediate products, increasing the purity of final materials. Furthermore, α-Fe_2O_3 nanoparticles prepared using microwave irritation typically have amorphous or low crystallinity structures as a result of short time reaction and low reaction temperatures.

Design criteria for fabricating α-Fe_2O_3 and Fe_3O_4 nano- and microstructures. Solvent volume: 80 ml; autoclave volume: 200 ml; temperature: 200 °C; reaction time: 24 h. DIW is for deionized water, and EG is for ethylene glycol.

No.	Product	Solvent	$FeCl_3 \cdot 6H_2O$ (mmol)	Urea (mmol)	Urea/Fe^{3+} (r)
1	W5	DIW	16	80	5
2	W10	DIW	16	160	10
3	W20	DIW	16	320	20
4	W30	DIW	16	480	30
5	W40	DIW	16	640	40

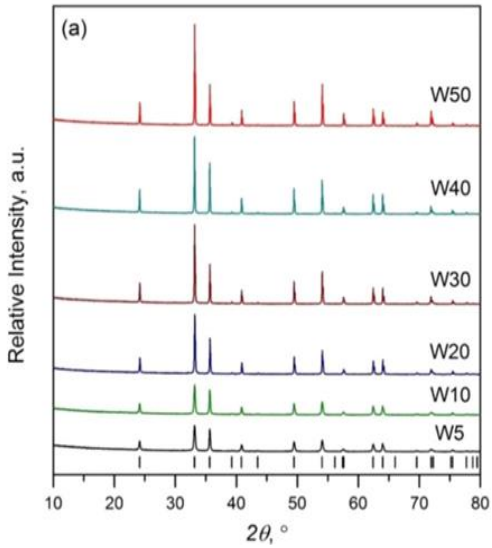

Figure 12. XRD patterns of as-prepared products from urea-water hydrothermal system.[152]

Kijima et al. reported preparing α-Fe_2O_3 nanoparticles via a microwave synthesis using 0.1 mol dm^{-3} $Fe(NO_3)_3 \cdot 9H_2O$ in a aqueous reaction medium.[182] The obtained materials had a high purity of α-Fe_2O_3 phase with a narrow particle size distribution of less than 10 nm, resulting in a high surface area of 217 m^2 g^{-1}. Due to a short reaction time of 120 s, obtained α-Fe_2O_3 showed broad XRD peaks, indicating a low crystalline structure.

Qiu et al. explored that the role of reaction time on fabrication of α-Fe_2O_3 nanoparticles using microwave synthesis.[183] The reaction was taken for 10, 20, 30 min with same precursor of $Fe(NO_3)_3 \cdot 9H_2O$ and urea at 120 ºC. As shown in Figure 13, products obtained different during reaction time were consistent with α-Fe_2O_3 phase but exhibiting various peak intensities. As the reaction time increased, peaks became more intense, indicating the degree of crystallinity of products was improved with increased reaction time.[183] Liao et al. prepared α-Fe_2O_3 nanoparticles by heating $FeCl_3 \cdot 6H_2O$ and urea in the mixture of water and PEG (polyethylene glycol-2000) for 10 minutes via microwave irradiation.[184] The resulting materials have a total amorphous structure without peaks observed in XRD. The particle sizes ranged from 3- 5 nm.

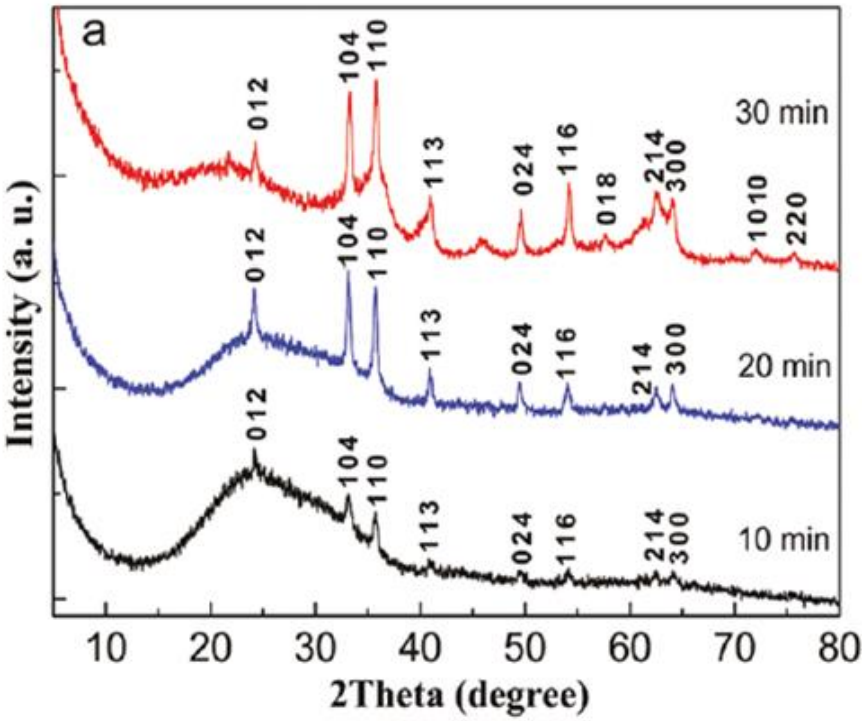

Figure 13. XRD patterns of the products synthesized at 120 ºC at different times in 0.1M $Fe(NO_3)_3$ and 0.5 M urea aqueous solutions.[173]

1.7.4 Synthesis of Hematite (α-Fe_2O_3) and Reduced Graphite Oxide (rGO) Nanocomposites

Because of the inherently low electronic conductivity and structural transformation over ion insertion/extraction, prior studies have introduced preparing the α-Fe_2O_3 and rGO nanocomposites in order to enhance the electron transfer and structure stability.[185-187] For the multiple synthesis methods explored to prepare α-Fe_2O_3/rGO nanocomposites, the fundamental principle is to react Fe^{3+} salts with functional groups on reduced graphene under appropriate temperatures. For example, Modafferi et al. fabricated α-Fe_2O_3/rGO nanocomposites by growing α-Fe_2O_3 nanoparticles on rGO nanosheets with precursors of $Fe(CH_3COO)_2$, ethanol, and GO.[188] The reaction was carried out in a hydrothermal reactor at 170 °C for 3 h. The resulting materials showed α-Fe_2O_3 nanoparticles decorated on the large sheets of rGO, which was further applied as an anode for Na-ion batteries. Zhang et al. added $Fe(NO_3)_3 \cdot 9H_2O$ salt into the GO solution with $CH_3COONa \cdot 3H_2O$ in aqueous solution.[189] The mixture was subsequently transferred to an autoclave at heated at 180 °C for 12 h. The obtained nanocomposites had rGO sheet with the size of several micrometers served as a platform, and which were decorated with a large number of uniform α-Fe_2O_3 nanoparticles with the average size of 40 nm. Similarly, Wang et al. also used $Fe(NO_3)_3 \cdot 9H_2O$ as Fe^{3+} salts and certain amount of urea as extra reservoir of OH^- groups as precursors and further decorated on GO.[190] The obtained mixture was transferred to a 100 mL Teflonlined autoclave and maintained at 180 ºC for 24 h. α-Fe_2O_3 nanoparticles decorated on rGO sheets had particle sizes in a range of 50 ~80 nm in size.

So far, α-Fe_2O_3/rGO nanocomposites have many applications, including

sensors,[187, 189] supercapacitors,[188] photoelectrochemistry,[191] anodes for Li-and Na-ion batteries,[192-193] but no work has been reported for α-Fe_2O_3/rGO nanocomposites as cathodes for Na-ion storage.

1.8 Objectives and Motivation

Motivated by urgent demand of high energy density, low-cost, and environmentally friendly cathodes for Na-ion batteries, the overall objectives of proposed work were (i) to understand factors that affect Na-ion storage in iron hydroxides/oxides-based cathodes, and (ii) to develop high electrochemical performance iron oxide (α-Fe_2O_3)/rGO nanocomposites as cathodes for Na-ion storage. The research work consisted of two primary objectives, as described below:

The first objective was to evaluate the effect of structural order of iron hydroxides on electrochemical Na-ion charge storage. The specific objectives were to:

- Synthesize and characterize iron hydroxides/oxides with different degrees of structural order (i.e. amorphous, crystalline) through varying synthesis conditions and thermal treatments
- Evaluate the effect of iron hydroxides with different degrees of structural order on electrochemical sodium-ion charge storage within the cathodic voltage range
- Investigate structural changes in iron hydroxides ($Fe(OH)_3$) with different degrees of structural order during the electrochemical charge/discharge process and its effect on the capacity degradation

The hypotheses of this project were firstly that the synthesis conditions (temperature and the molar ratio of reagents) would affect the degree of structural order (i.e. amorphous, crystalline structure). Secondly, the disordered (short-range order) iron

hydroxides ($Fe(OH)_3$) will have a better electrochemical capacity than that of high crystalline ($Fe(OH)_3$) or related oxide phases (α-Fe_2O_3) due to easier accommodation of Na^+ ions, whereas a well-crystallized structure has difficulty in expanding or contracting, limiting the diffusion of ions. Thirdly, the lower degree of structural order will result in an improved reversibility compared with the more crystalline material by accommodating reversible structural changes during repeated charging and discharging.

Prior studies have focused on less ordered nanomaterials containing iron, such as $FePO_4$, $FeVO_4$, and FeF_3.[138, 145, 194] However, to the best of my knowledge, prior studies have not focused on the design of low crystallinity iron hydroxides materials to improve the sodium-ion storage performance.

The second objective was to investigate low crystalline α-Fe_2O_3/rGO nanocomposites as high-performance cathodes for Na-ion storage. The specific objectives were to:

- Synthesize low crystalline α-Fe_2O_3/ rGO nanocomposites as well as bare low crystalline α-Fe_2O_3
- Investigate the effect of the degree of crystallinity on the Na-ion storage property of α-Fe_2O_3
- Evaluate if α-Fe_2O_3/rGO nanocomposites will exhibit better electrochemical properties than pristine α-Fe_2O_3

The hypotheses of this project were firstly that low crystalline α-Fe_2O_3 will exhibit better electrochemical properties than high crystalline commercial α-Fe_2O_3 due to the benefits of structure disorder which were explored in the first objective, and secondly, α-Fe_2O_3/rGO nanocomposites will exhibit better electrochemical properties than pristine

α-Fe_2O_3 because of a higher electronic conductivity, a higher surface area, and better structural stability.

Prior studies have demonstrated hybrization of carbonaceous materials, CNTs and rGO, could improve the Na-ion storage properties of γ-Fe_2O_3, β-FeOOH, and FeF_3 due to the enhanced electronic conductivity and ion transport.[60, 98, 121] However, α-Fe_2O_3/rGO nanocomposites have not been reported as cathodes for Na-ion storage.

2. EXPERIMENTAL METHODS

2.1 Chemicals

Iron (III) nitrate 9-hydrate ($Fe(NO_3)_3 \cdot 9H_2O$, lab grade, Ward's Science), urea (N_2COH, ACS grade, BDH), ethylene glycol ($C_2H_6O_2$, 99%, BDH), potassium permanganate ($KMnO_4$, ACS grade, AMRESCO), and hydrogen peroxide (H_2O_2, 30%, BDH) were obtained from VWR Internationals (Radnor, PA, USA). Sulfuric acid (H_2SO_4, 95%-98%), sodium nitrate ($NaNO_3$, ≥ 99.0%), and iron (III) oxide (powder, < 5μm, ≥99%) were obtained from Sigma-Aldrich (St. Louis, MO, USA). Graphite flakes (C, median 7-9 micro, 99%, LOT #T08B024) were obtained from Alfa Aesar (Ward Hill, MA, USA). All reagents were used without further purification.

2.2 Synthesis of Iron (III) Hydroxide Nanomaterials with Different Degrees of Crystallinity

$Fe(OH)_3$ nanomaterials with different degrees of structural order were synthesized in the presence of urea and ethylene glycol (EG) using a hydrothermal method. Synthetic conditions for preparing different $Fe(OH)_3$ nanostructures are shown in Table 7. 0.88g iron (III) nitrate 9-hydrate $Fe(NO_3)_3 \cdot 9H_2O$ and different amounts of urea were dissolved in 20 mL deionized (DI) water (⩾ 13 MΩ cm^{-1}), and then 25 mL EG was added to the solutions. The mixtures were further stirred at room temperature for 15 minutes to form homogenous dark yellow brown solutions. Then, mixtures were transferred into a Teflon-lined stainless-steel autoclave with a capacity of 60 mL and maintained at a temperature of 120 °C for 4.5 hours in an oven. The products were labeled as FE-0-120, FE-3-120, and FE-5-120. α-Fe_2O_3 nanomaterials were prepared at 180 °C for 4.5 hours using a molar ratio of urea to $Fe(NO_3)_3 \cdot 9H_2O$ as 1:3, as described in Table 1, and labeled as FE-

3-180. All the resulting materials were collected by centrifugation at 5000 rpm (Sorvall LYNX 600, Thermo Scientific, 4304 rcf) for 15 minutes and rinsed three times using DI water. All the synthesized nanomaterials were subsequently dried in an oven at 60 °C for 16 hours.

2.3 Synthesis of Pristine α-Fe_2O_3 Nanoparticles and α-Fe_2O_3/rGO Nanocomposites

Table 7. Synthetic conditions of different $Fe(OH)_3$ and α-Fe_2O_3 nanomaterials

Temperature (ºC)	**Fe^{3+}/urea (molar ratio)**	**Label**
120	1:0	FE-0-120
120	1:3	FE-3-120
120	1:5	FE-5-120
180	1:3	FE-3-180

Graphite oxide was synthesized from natural graphite flake using a modified Hummer's method.[195] 0.5g graphite flake powders were mixed with 1g sodium nitrate ($NaNO_3$) and 25 mL concentrated sulfuric acid (H_2SO_4) in an ice bath. After robust stirring for 10 minutes, 3g potassium permanganate ($KMnO_4$) was then added. The mixture was stirred at 35-40°C in an oil bath for 2 hours. Successively, 100 mL of DI water and 6 mL 30% hydrogen peroxide (H_2O_2) were added to the reaction, and the mixture color changed to gold yellow color. The products were collected by centrifugation at 5000 rpm for 15 minutes and rinsed three times using DI water. The graphite oxide (GO) was obtained by freeze drying under vacuum. To further reduce the graphite oxide and obtain reduced graphite oxide nanosheets, as-prepared GO powders were heated under flowing argon at 300°C for 2 hours. The resultant black fluffy materials were collected as powders.

α-Fe_2O_3 nanoparticles were synthesized using a microwave-assisted hydrothermal process. 0.8 g $Fe(NO_3)_3 \cdot 9H_2O$ was dissolved in 20 mL DI water and stirred for 15 min. Then the mixture and a magnetic stirrer were transferred into a Discover SP Microware Reactor and sealed. The reaction was operated at a temperature of 120 °C for 5 mins under active stirring. The obtained precipitates were recovered by centrifugation at 5000 rpm (Sorvall LYNX 600, Thermo Scientific, 4304 rcf) for 15 minutes and rinsed three times using DI water. The powder was dried at 60°C overnight under ambient atmosphere.

To prepare the α-Fe_2O_3/rGO nanocomposites, the first step was to prepare a homogeneous rGO aqueous solution. rGO powders were suspended in 10 mL DI and sonicated for 30 minutes. 0.8 g $Fe(NO_3)_3 \cdot 9H_2O$ was dissolved in 10 mL DI water and stirred for 15 min. The two solutions were then mixed together. The same procedures were subsequently used for the synthesis of pure α-Fe_2O_3 nanoparticles without rGO.

2.4 Structural, Physical and Electrical Characterization

Powder X-ray diffraction (XRD) was performed with a Bruker D8 Focus powder X-ray diffractometer using Cu Kα radiation (λ = 1.54060 Å). XRD patterns were recorded for 2θ between 20° and 65° using a step size of 0.0002° and an integration time of 5 s per step.

Raman spectra of rGO was obtained with a Horiba LabRam HR Evolution Confocal Raman Spectrometer equipped with an 1800 groove/mm grating. Sample excitation was performed using the 514 nm line of a Melles Griot (Carlsbad, CA) argon-ion laser. Raman scattered light was collected in a backscattering geometry using an Olympus (Center Valley, PA) 50 × (0.75 NA) MPlan N objective. Spectra were obtained

using a 24 s acquisition time and averaged over 10 accumulations. The laser power was set to 1% using neutral density filters, resulting in a measured power of 0.314 mw.

Scanning electron microscopy (SEM) images were obtained using a Helios NanoLab 400 DualBeam Field Emission Scanning Electron Microscopy. For sample preparation, powders were dispersed in isopropanol and deposited on an aluminum sample holder, which were further dried in an oven at 60 ºC for 10 minutes.

Transmission electron microscopy (TEM) images were obtained using a JEOL JEM 1200EXII microscope with an accelerating voltage of 120kV. TEM samples were prepared on lacy carbon grids by depositing a suspension of the dried powder in isopropanol. The lacy carbon grids with samples were dried overnight at room temperature.

Thermogravimetric analysis (TGA) was used to measure the weight loss of $Fe(OH)_3$ nanomaterials, α-Fe_2O_3 nanoparticles, rGO nanosheets, commercial α-Fe_2O_3 nanoparticles, and α-Fe_2O_3/rGO nanocomposites. TGA (TA Instruments Q50) was performed at a constant heating rate of 10 ºC/min in air from room temperature to 600 ºC.

Attenuated total (internal) reflectance-Fourier transform infrared (ATR-FT-IR) spectra were collected over the range of 4000−400 cm^{-1} using a Harrick Scientific (Pleasantville, NY) SplitPea attenuated total (internal) reflectance (ATR) microsampling accessory coupled to a Bruker (Billerica, MA) Tensor II FT-IR spectrometer which was controlled using Bruker OPUS 7.5 software (version 7.5.18). The ATR accessory contained a silicon hemispherical internal reflection element (IRE), and samples were brought into contact with the IRE using a loading of 0.5 kg. The infrared spectra represent the average of 64 individual scans collected at a spectral resolution of 4 cm^{-1}.

To measure electronic conductivities of $Fe(OH)_3$ and α-Fe_2O_3 nanomaterials, ~150 mg of powder was placed in a cell (Pred Materials, HS flat cell) with a 5 kg force spring. Two-point probe measurements were obtained using a constant voltage (±0.1 V) applied to the cell using an Arbin Instruments BT-2043 potentiostat/galvanostat. The current was monitored until quasi steady state was reached (~3 min), and the resistance was determined using Ohm's law, $R = V/I$. The thickness and diameter of the pellet were measured using a micrometer (Mitutoyo, United States). The electronic conductivity, σ_{elec} (S cm^{-1}), was calculated from the experimentally measured values using the equation $\sigma = l/(RA)$, where l is the thickness of the sample, R is the measured resistance (Ω), and A is the cross-sectional area.

2.5 Electrode Preparation and Cell Assembly

In order to have a good electronic conductivity and mechanical stability, Na-ion battery electrodes were prepared with active materials, polyvinylidene fluoride (PVDF, Kynar Flex 2801-00 Lot #10C8143) binder, conductive carbon (Timcal, Super 65), and N-methyl-2-pyrrolidone (NMP) solvent. Electrodes were fabricated from a slurry composed of 80% active materials, 10 wt% Super 65 carbon, 5 wt% binder and NMP. For a typical slurry, 200 mg of active materials used 0.4 g NMP. The slurry was stirred overnight and then cast onto a cleaned aluminum foil current collector. The obtained electrode sheets were dried overnight within a fume hood and then transferred to a 60 ºC oven and allowed to dry overnight. Discs (0.5 inch in diameter) of the dried electrode sheets were then pressed out and dried in a vacuum oven at 120 ºC for 16 hours. The electrode was assembled within a CR2032 coin cell (Pred Materials). The cell configuration as shown in Figure 14. Cells were fabricated in an inert atmosphere

glovebox (argon, ≤ 1 ppm H_2O) using electrode discs, separators (glass microfiber filter, GF/C, Whatman), a metallic sodium (Sigma-Aldrich) as counter/reference electrode, and the electrolyte (1M $NaClO_4$ in PC (Sigma-Aldrich)). To prepare the electrolyte, $NaClO_4$ powders were dried in vacuum over at 120 °C for 24 hours. In addition, 4 Å molecular sieves were activated by treatment within a muffle furnace for 24 hours at 500°C. The activated molecular sieves were removed before the temperature dropped below to 150°C and put into the vacuum chamber of an insert atmosphere glovebox. All the equipment and materials that were used for dehydration of PC were dried in a vacuum oven at 120°C for 24 hours. 20 mL PC were mixed with 2 mg activated molecular sieves (10% m/V). The mixture was stirred vigorously stirred for 24 hours to dehydrate in PC, which was filtered with 25 mm Syringe Filters (Acrodisc, Pall Laboratory) to remove the impurities and molecular sieves.

2.6 Electrochemical Measurements

Galvanostatic charge-discharge measurements were performed to investigate the voltage profile, rate capability, and cycling stability of the active cathode materials. The discharge capacity (Q) equals the total electrons during the time of full discharge, which can be obtained from the current (I) and the time (t) using the equation, $Q = I \times t$. Cells with $Fe(OH)_3$, α-Fe_2O_3, rGO nanosheets, commercial α-Fe_2O_3 nanoparticles, and α-Fe_2O_3/rGO nanocomposites, respectively were discharged and charged in the voltage window from 1.0-4.0 V vs. Na on an Arbin Instruments BT2043 test station using current rates of 0.1-2C (the theoretical capacity is 337 mAh g^{-1}) which resulted in mass-normalized currents of 47− 934 mA g^{-1} based on the active material mass. The discharge time at different mass-normalized currents was determined from the experimental data.

Cyclic voltammograms were measured using the same configuration over a voltage range of 1.0−4.0 V vs Na at scan rates of 0.1−0.5 mV s^{-1}.

.

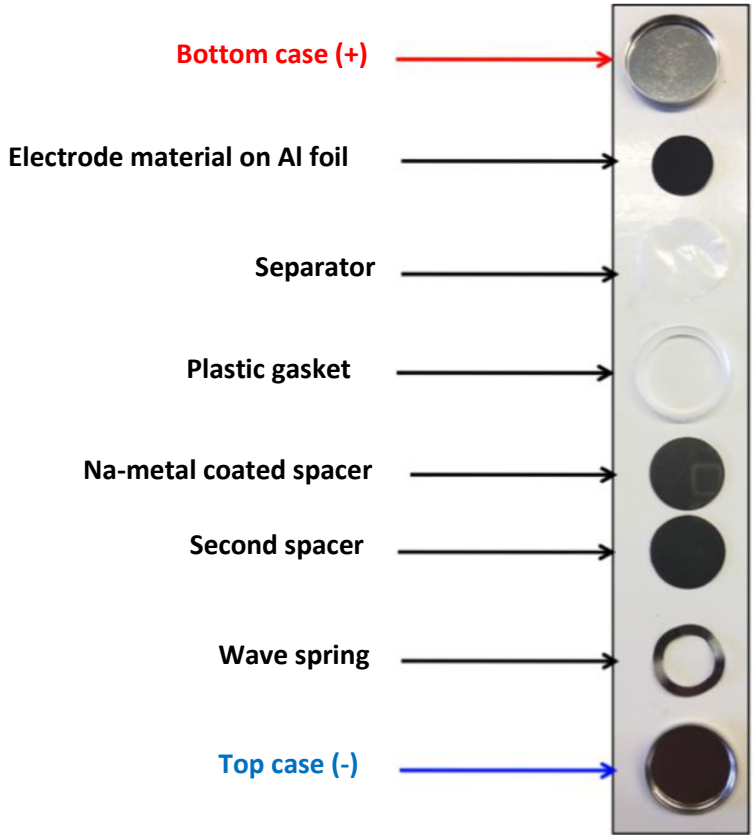

Figure 14. Schematic illustration of Na-ion coin cell assembly.

3. RESULTS AND DISCUSSION

3.1 The Effect of Structural Order on the Na-Ion Storage Properties of Iron Hydroxide/Oxides Cathodes

3.1.1 Study of Phase and Crystallinity of Iron Hydroxide/Oxides Nanocomposites

XRD patterns of products prepared at different temperatures or with various amount of urea are shown in Figure 15. Without urea (urea: Fe^{3+} = 0:1), the obtained materials, FE-0-120, exhibited a nearly amorphous structure without clearly observed peaks in the XRD plot. As the ratio of urea/Fe^{3+} is increased to 3:1, very weak peaks showed up and the peaks have similar 2θ values as peaks for the $Fe(OH)_3$ phase (JCPDS card no. 38-0032).[196] The peak position of the peak at two theta degree of 46.9° corresponds to a d-spacing of 1.94 Å. The d-spacing value is slightly shorter but in the range of Fe-O bond length (0.984-2.025 Å), suggesting some ordering of Fe-O bonds within the structure.[155] As the amount of urea increased, the XRD peak intensity of resulting material, FE-5-120, are enhanced but keeps the same phase, indicating a higher dose of urea facilitates the crystallization of $Fe(OH)_3$, which is in good agreement with the previous report that urea added in the reaction system increased the crystallization of α-Fe_2O_3 and $BiVO_4$ nanoparticles.[161, 197-198] $Fe(OH)_3$ has been reported as a naturally amorphous or a short-range order material.[152-153] Therefore, enhancing the dose of urea does not result in a highly crystalline $Fe(OH)_3$. However, as the reaction temperature was elevated to 180 °C, the XRD peak positions of resulting materials prepared at 180 °C are well indexed to the hematite phase, α-Fe_2O_3 (JCPDS card no. 33-0664), suggesting that the higher temperatures leads to the phase transition from $Fe(OH)_3$ to α-Fe_2O_3.[152, 199] Prior studies showed that $Fe(OH)_3$ was not thermally stable and converted to α-Fe_2O_3

phase via thermal treatment when the temperature was higher than 150 °C.[200] Therefore, the formation of α-Fe_2O_3 can be attributed to the dehydration of $Fe(OH)_3$ at higher temperatures. The mechanism of dehydration during the phase transition from $Fe(OH)_3$ to α-Fe_2O_3 can be by explained the removal of proton from an OH^- group combining with another OH^- group, leading to loss of one water molecule and formation of an oxo linkage, shown in equation as described in section 3.1.4.[156] Furthermore, FE-3-180 exhibited a higher degree of crystallinity compared to that of FE-3-120 due to the higher reaction temperature that can induce the crystallization process

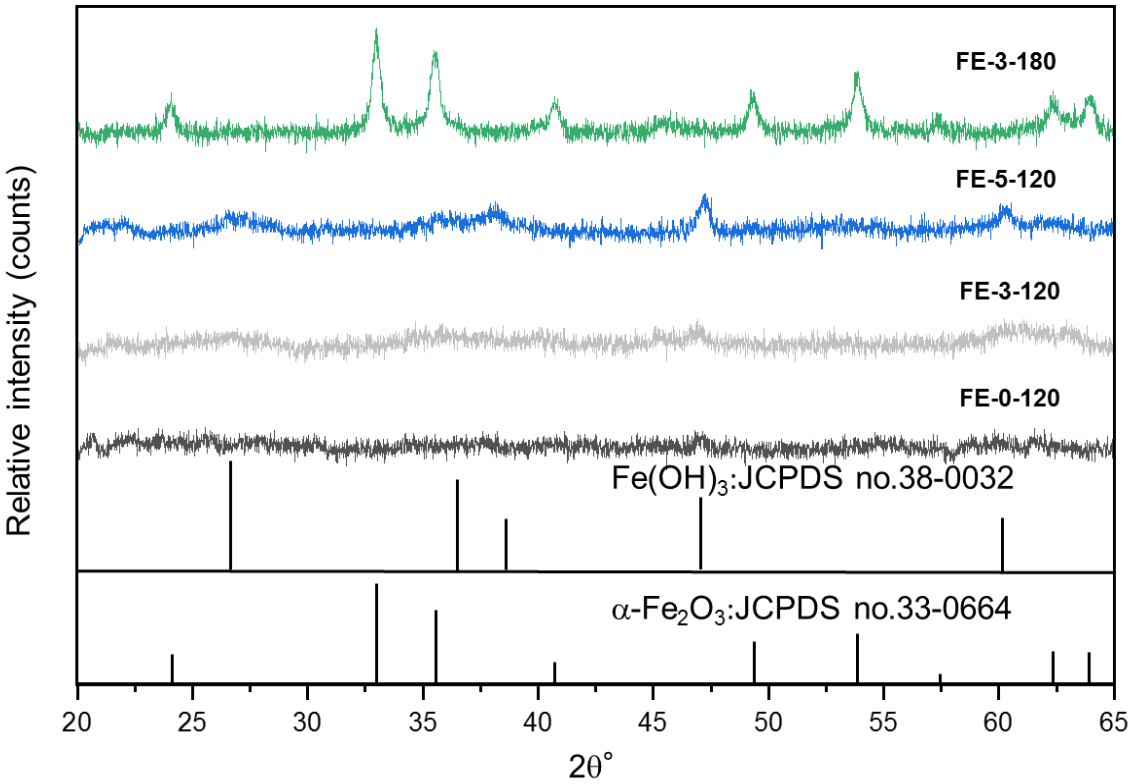

Figure 15. XRD patterns of $Fe(OH)_3$/α-Fe_2O_3 obtained with different amount of urea and temperatures.

3.1.2 Microscopy Analysis of $Fe(OH)_3$ and α-Fe_2O_3 Nanomaterials

The morphologies of the obtained nanomaterials were examined using scanning electron microscopy (SEM). As shown in Figure 16, without urea included within the synthesis, the amorphous $Fe(OH)_3$, FE-0-120, exhibited a nanoparticle morphology. By contrast, the sample prepared included urea, FE-3-120 and FE-5-120, had sheet-like morphologies, suggesting that included urea promotes the growth of $Fe(OH)_3$,

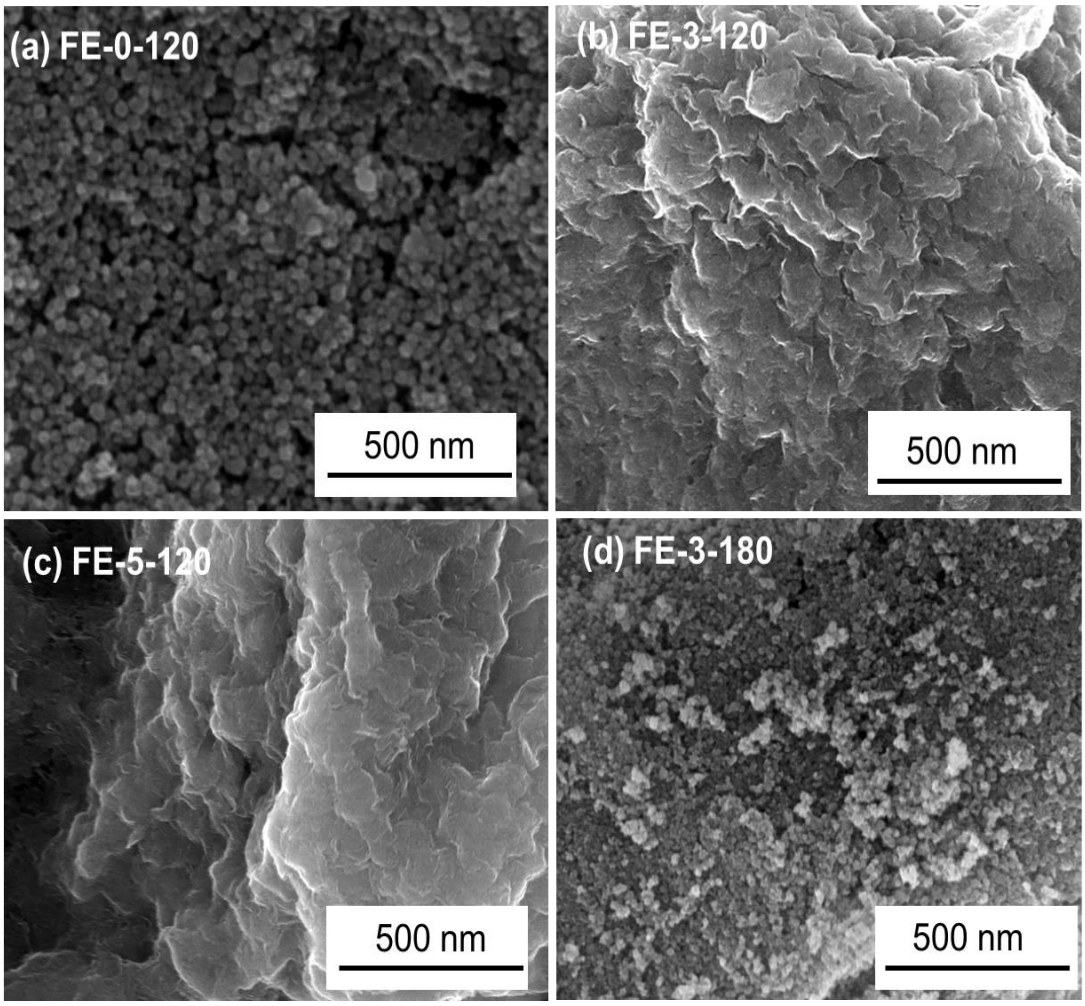

Figure 16. SEM images of $Fe(OH)_3$ and α-Fe_2O_3 obtained at: (a) 120 °C, urea/ Fe^{3+}= 0:1 (b) 120 °C, urea/ Fe^{3+}= 3: 1 (c) 120 °C, urea/ Fe^{3+}= 5:1 (d) 180 °C, urea/ Fe^{3+}= 3:1.

nanosheets, which is consistent with the prior study that the average crystalline sizes of $BiVO_4$ increased as the amount of urea enhanced.[197] FE-3-180, obtained at 180 °C,

showed α-Fe_2O_3 structure and exhibited a particle-like nanostructure, suggesting a higher temperature not only leads to phase transformation but also a morphology change.

3.1.3 Infrared Spectroscopic Analysis of $Fe(OH)_3$ and α-Fe_2O_3 Nanomaterials

Due to the amorphous/low crystalline nature of $Fe(OH)_3$, XRD results only provides limited information about the structure of $Fe(OH)_3$. Infrared spectroscopy is a useful tool to examine amorphous structures since it does not rely on crystallinity as does XRD. The obtained ATR-FT-IR spectra for the samples are presented in Figure 17. As shown in Figure 17 (d), Fe-O stretching modes are observed in the ~400-700 cm^{-1} region in the infrared spectra of four samples. The infrared spectrum of crystalline α-Fe_2O_3 nanoparticles, Fe-3-180 sample, the band at the high frequency of ~535 cm^{-1} can be referred to Fe–O deformation in the octahedral and tetrahedral sites, while the low frequency band ~435 cm^{-1} is attributed to Fe–O deformation in the octahedral site of hematite.[201] By contrast, in the infrared spectrum of amorphous $Fe(OH)_3$, FE-0-120, samples, the band at the high frequency completely disappeared, whereas the low frequency band was not clearly observed, suggesting that there is no Fe–O tetrahedral coordination but only a little Fe-O in the octahedral sites. In addition, the disappearance of the band at ~535 cm^{-1} could be attributed to the lack of a symmetric stretching mode of Fe-O in amorphous materials.[202] With respect to two semi-crystalline $Fe(OH)_3$ samples, FE-3-120 and FE-5-120, respectively, there is only one distinct band centered at ~445 cm^{-1} due to a different coordination environment of Fe-O. A strong and broad band in the range of 3000-3500 cm^{-1} is observed in spectra of all $Fe(OH)_3$ samples due to

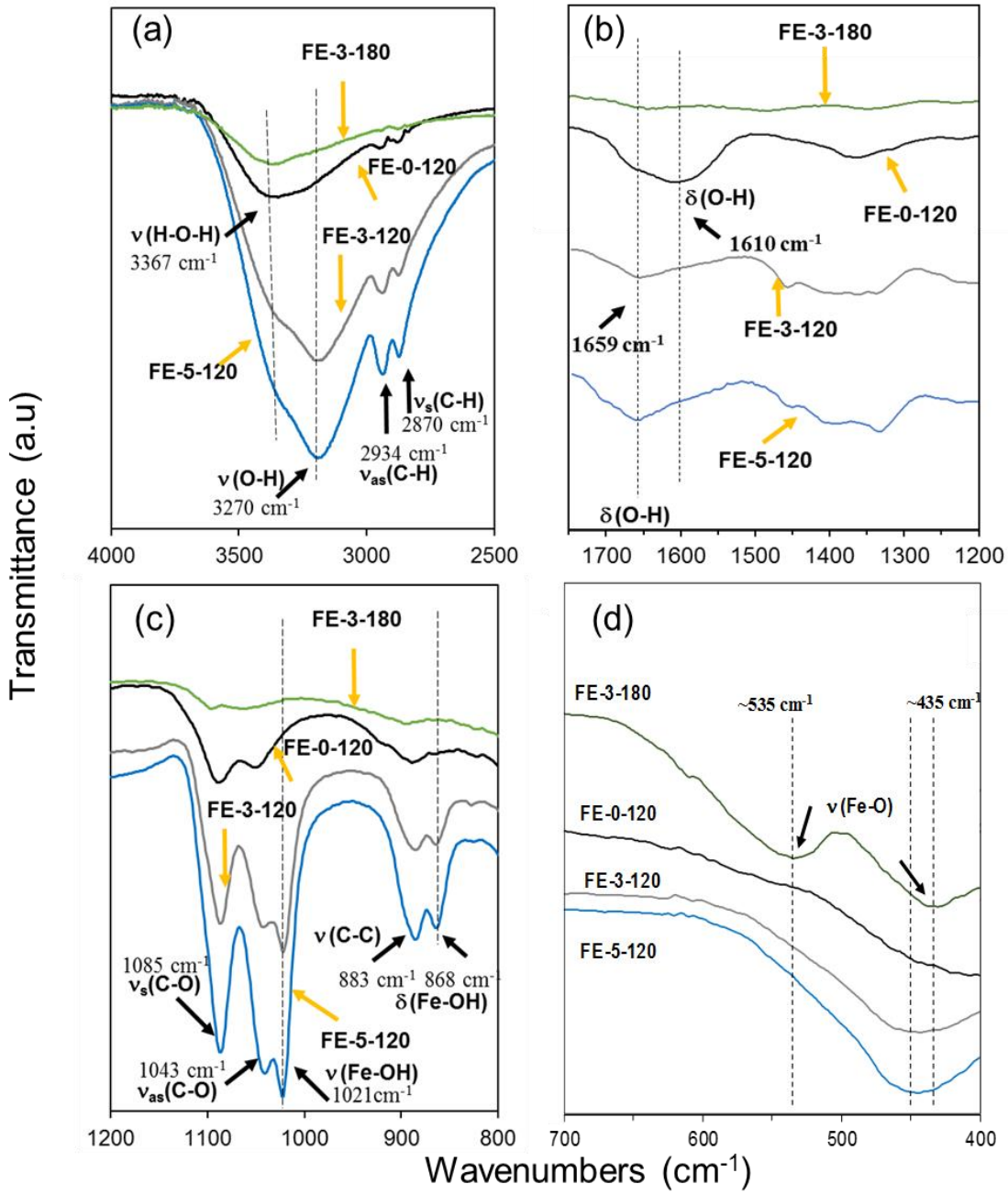

Figure 17. ATR-FT-IR spectra of as-prepared iron hydroxides/oxides with different degrees of crystallinity within the (a) 4000-400 cm^{-1} spectral range; (b) the expanded 4000-2500 cm^{-1} spectral range;(c) the expanded 1200-800 cm^{-1} spectral range; (d) the expanded 700-400 cm^{-1} spectral range.

overlapping OH group and H_2O stretching vibrations, shown in Figure 17 (a).[203]

Specifically, for the amorphous $Fe(OH)_3$ sample, FE-0-120, one band centered at ~3367

cm^{-1} can be attributed to contribution of bands due to the asymmetrical stretching vibrations of O-H group in adsorbed H_2O molecules (~ 3351 cm^{-1}) [161, 204] and EG (~ 3390 cm^{-1}).[205] Another band at ~3270 cm^{-1} could be assigned to the O-H symmetrical stretching mode in H_2O (~3261 cm^{-1}) [206] or $Fe(OH)_3$ (~3301 cm^{-1}).[204, 207] In contrast, the relative intensity of two bands switches in the spectra of two semi-crystalline $Fe(OH)_3$ samples. The band centered at ~3240 cm^{-1} becomes more intense as the degree of structural order of $Fe(OH)_3$ increases, suggesting this band can be mainly ascribed to O-H stretching vibration in $Fe(OH)_3$ due to higher crystalline $Fe(OH)_3$ samples containing larger amount of OH^- groups compared to the FE-0-120 sample. In addition, the amount of EG in two semi-crystalline $Fe(OH)_3$ samples appear to be very similar based on TGA analysis described below. The presence of EG in all $Fe(OH)_3$ samples is supported by two clearly observed bands at ~2934 cm^{-1} and 2870 cm^{-1} attributed to the asymmetric C–H and symmetric C–H stretching vibrations of EG.[208] Shown in the Figure 17 (b), for the amorphous $Fe(OH)_3$, FE-0-120 sample, there is a weak band and a very strong band at ~1650 cm^{-1} and ~1610 cm^{-1}, respectively. The band at a higher frequency (~1650 cm^{-1}) could be attributed to OH bending vibration in liquid water or physically absorbed water,[209] whereas the band at lower frequency (~1610 cm^{-1}) can be assigned as OH bending vibrations in structural water.[206] The band coming from urea's carbonyl (~1682 cm^{-1}) was not observed.[210] The high intensity of band at ~1610 cm^{-1} indicates amorphous $Fe(OH)_3$ may have a substantial amount of structural water. The weak band at ~1650 cm^{-1} is attributed to O-H groups in $Fe(OH)_3$ and the strong one at ~1610 cm^{-1} is assigned to the structural water molecules within amorphous structure.[206, 209] Without urea providing OH^-, Fe^{3+} may coordinate H_2O instead of OH^- to form amorphous $Fe(OH)_3$.[211] In

comparison, within the infrared spectra of two semi-crystalline $Fe(OH)_3$ samples, FE-3-120 and FE-5-120, the bands at ~1610 cm^{-1} have almost disappeared and only bands at ~1650 cm^{-1} are observed, suggesting that in these two samples, trace or no structural H_2O exists and a certain amount of physically absorbed water exists. Shown in Figure 17 (c), bands at ~1085 and 1043 cm^{-1} in the spectra of three $Fe(OH)_3$ samples are attributed to asymmetric C-O stretching and symmetric C-O stretching vibrations of EG, respectively.[212] Another two bands at ~1021 and 864 cm^{-1} are attributed to Fe–OH stretching and bending vibrations, respectively.[213] The intensity of these two bands (~1021 and 864 cm^{-1}) increased as crystallization of $Fe(OH)_3$ increased from FE-0-120 to FE-3-120 and FE-5-120. The band at ~883 cm^{-1} can be ascribed to the C-C stretching vibrations of EG.[214] With respect to high crystalline α-Fe_2O_3 nanoparticles, there is a much weaker band at ~3367 cm^{-1} compared to $Fe(OH)_3$ samples, suggesting α-Fe_2O_3 nanoparticles have a smaller amount of adsorbed H_2O molecules. Within the α-Fe_2O_3 sample, the band at ~3270 cm^{-1} disappears, suggesting there is no/little EG in the sample. Similarly, bands related to EG at ~2934, 2870, 1085, and 1047 cm^{-1} are also removed, confirming that crystalline α-Fe_2O_3 nanoparticles do not contain a significant amount of EG, which is significantly different from other three $Fe(OH)_3$ samples.

3.1.4 Thermogravimetric Analysis (TGA) of $Fe(OH)_3$ and α-Fe_2O_3 Nanomaterials

Figure 18 shows thermogravimetric analysis (TGA) curves for amorphous/ semi-crystalline $Fe(OH)_3$ and crystalline α-Fe_2O_3. The weight loss of amorphous/low crystalline $Fe(OH)_3$ can be attributed to the removal of loosely-bond adsorbed water and structural water, and EG. The dehydration of $Fe(OH)_3$ could result in phase transformation. From room temperature to 120 °C, the weight loss of FE-0-120,

FE-3-120, and FE-5-120 samples were calculated as 5.53%, 13.06%, and 10.05%, respectively. Differences in weight change for the three samples are due to $Fe(OH)_3$ materials having different amount of physically adsorbed water at the starting point.

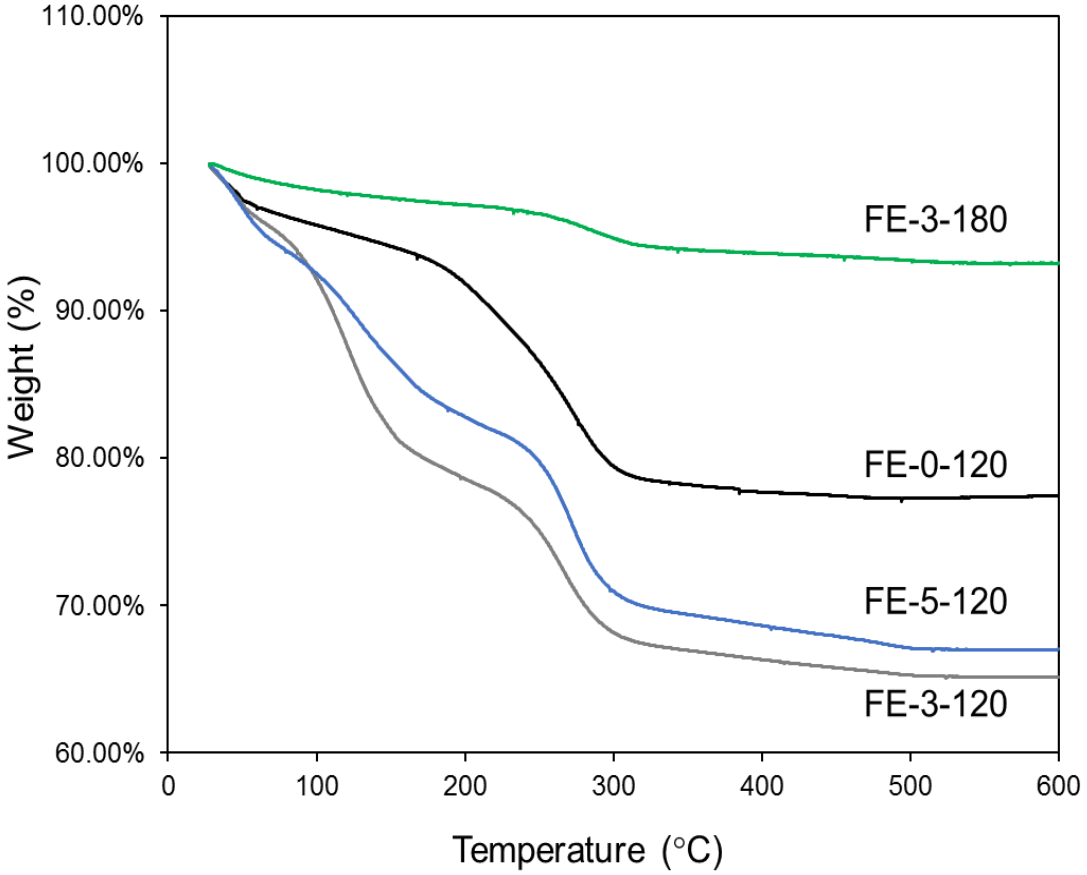

Figure 18. TGA curves of iron oxyhydroxides/oxides with different degrees of crystallinity.

From 120°C to 200°C, the weight loss of three samples is primarily ascribed to the decomposition of EG. Shown in the Figure 19, liquid EG are completely boiled at ~200°C. Maybe a small amount of hydrated H_2O is also removed. However, it is assumed that the weight loss of EG is dominate at this temperature range. Therefore, the formulas of FE-0-120, FE-3-120, and FE-5-120 sample are $Fe(OH)_3(C_2H_6O_2)_{0.069}$, $Fe(OH)_3(C_2H_6O_2)_{0.158}$, $Fe(OH)_3(C_2H_6O_2)_{0.133}$, respectively. Notably, the relative amount of EG within amorphous $Fe(OH)_3$ nanoparticles is significantly lower than two low

crystalline $Fe(OH)_3$ nanosheet samples, which contain similar content of EG. EG plays a critical role in directing growth and control morphology of iron-containing nanomaterials due to its ability to form hydrogen-bonded networks and chelating Fe^{3+} or Fe^{2+} ions.[161, 215-216] It has been found that increasing ratio of EG/H_2O as the reaction medium can greatly enlarge the size of synthetic iron-based materials.[104] Therefore, the variation in content of EG within $Fe(OH)_3$ nanoparticles and nanosheets could explain their significantly different morphologies besides the difference dose of urea. Within the temperature range between 200 °C and 500 °C, a sharp drop in weight loss was observed for all three samples, which is consistent with a phase transformation. In order to determine the phase at the temperature of 400 °C, the FE-3-120 sample was annealed in

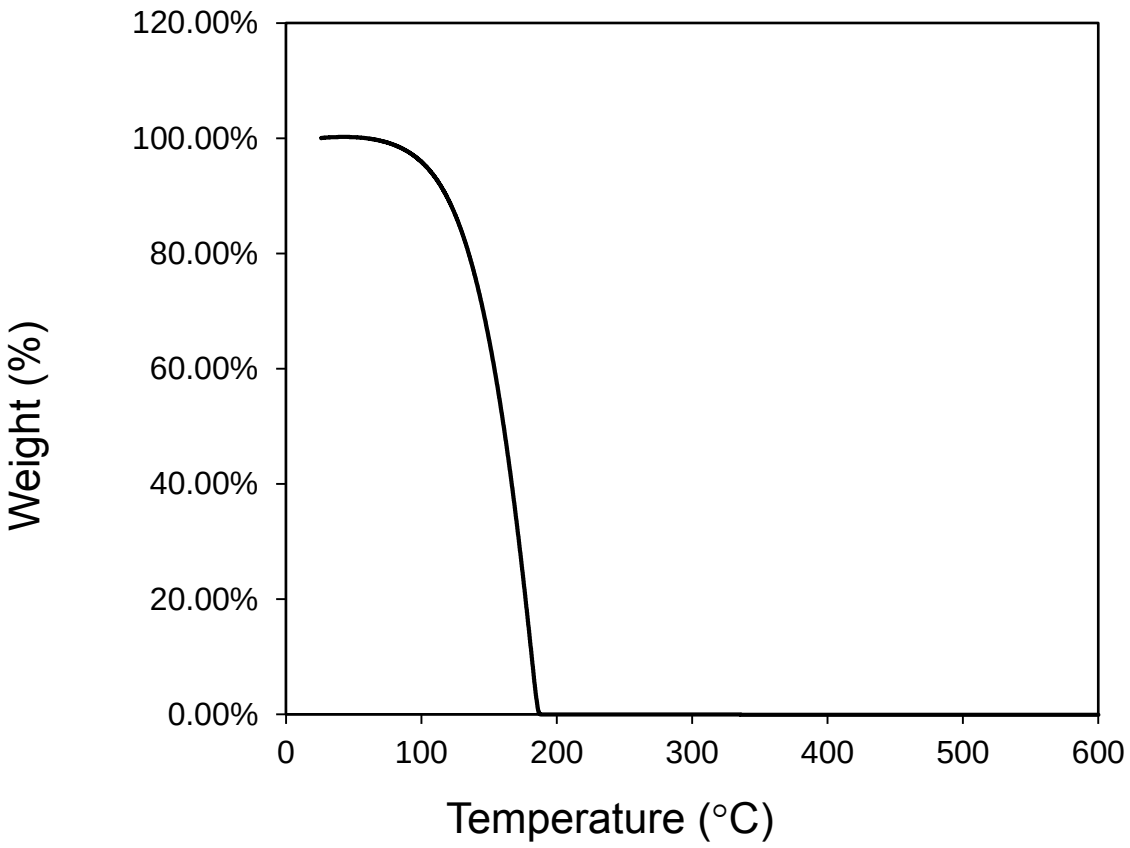

Figure 19. TGA curves of liquid EG

air at 400 °C for 2 h and the phase of obtained materials was examined by the XRD, shown in Figure 20. After treatment to 400 °C, low crystallinity $Fe(OH)_3$ nanosheets are transformed to high crystalline α-Fe_2O_3, which is consistent with prior studies.[217-218] The weight/phase change as a function of enhanced temperature can be described as below:

$$2Fe(OH)_3 \xrightarrow{\Delta} \alpha\text{-}Fe_2O_3 + 3H_2O \quad (26)$$

Therefore, the weight loss between 200 °C -500 °C can be may be primarily attributed to

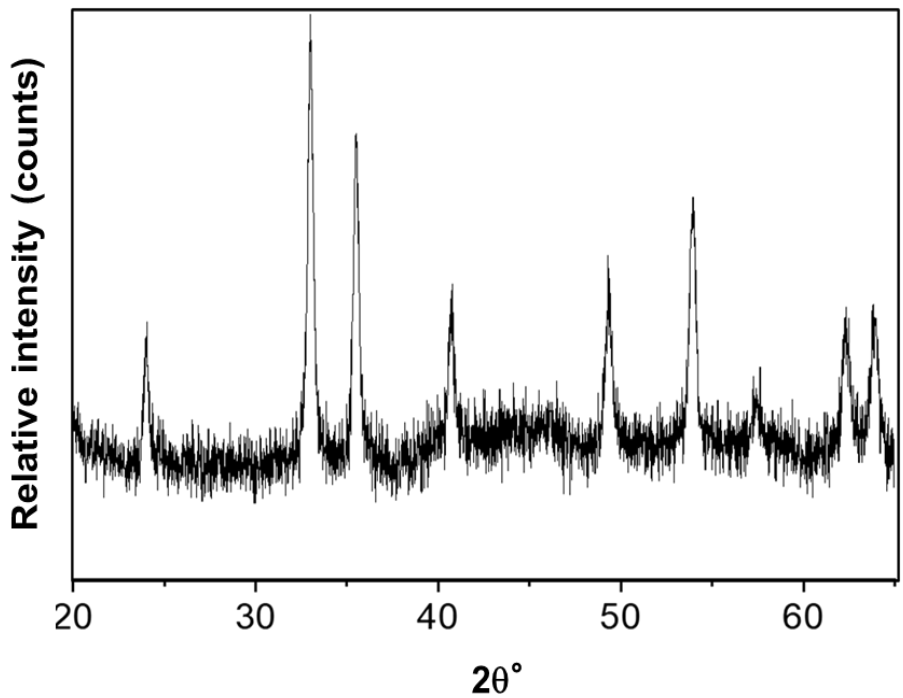

Figure 20. XRD pattern of $Fe(OH)_3$ nanomaterials (FE-3-120 sample) annealed at 400 ºC for 2h.

dehydration of $Fe(OH)_3$ to α-Fe_2O_3 based on the XRD result shown in Figure 20, and some EG may also be removed. The percentage of weight loss in amorphous and low crystalline $Fe(OH)_3$ during the dehydration were calculated as 12.68%, 13.19%, and 15.55%, respectively, suggesting that $Fe(OH)_3$ nanomaterials with a higher structural order have more water released, which could be attributed to coordinating more OH^- groups in higher molar ratio of urea/Fe^{3+} reaction medium. As temperature kept

increasing to 600 °C, no notable weight loss was observed in the TGA curves since α-Fe_2O_3 is very thermally stable in air. With respect to the crystalline α-Fe_2O_3 sample, it exhibits only 5.84% weight loss from room temperature to 500 °C overall. Below the temperature of 120 °C, the weight loss is as a result of removing surface absorbed water. Between 120 °C and 200 °C, it is only observed 0.74% weight loss, indicating that the there is only trace amount of EG, which is in agreement with the FT-IR spectrum showing very low intense bands of EG. The weight loss from 200 °C to 500 °C, the weight change (3.31%) was ascribed to removal of structural water. The formula of crystalline α-Fe_2O_3 sample can be calculated as α-$Fe_2O_3(OH_2)_{0.10}$ based on weight loss, suggesting that the crystalline α-Fe_2O_3 nanoparticles have a very low level of water in the structure.

3.1.5 Electrochemical Properties of Amorphous, Semi-Crystalline $Fe(OH)_3$, and Crystalline α-Fe_2O_3 Cathodes

3.1.5.1 Galvanostatic Charge-Discharge of Amorphous, Semi-Crystalline $Fe(OH)_3$, and Crystalline α-Fe_2O_3 Cathodes

In order to understand the effect of the degree of structural disorder on Na-ion storage, the electrochemical properties of amorphous $Fe(OH)_3$ nanoparticles, two semi-crystalline $Fe(OH)_3$ nanosheets, and high crystalline α-Fe_2O_3 nanoparticles were evaluated. The cells were galvanostatically cycled at room temperature. Figure 21 shows the charge–discharge profiles of $Fe(OH)_3$ and α-Fe_2O_3 cathodes against Na metal in the range 1.0–4.0 V at the mass-normalized current of 47 mA g^{-1} for the third cycle. All samples showed an average discharge voltage of ~2.2 V vs Na, which is ~0.2 V lower than the corresponding value in Li-ion batteries.[105]

The results are consistent with a prior study that Na insertion reduces the potential by 0.18–0.57 V compared to Li insertion in the compounds.[219] The amorphous

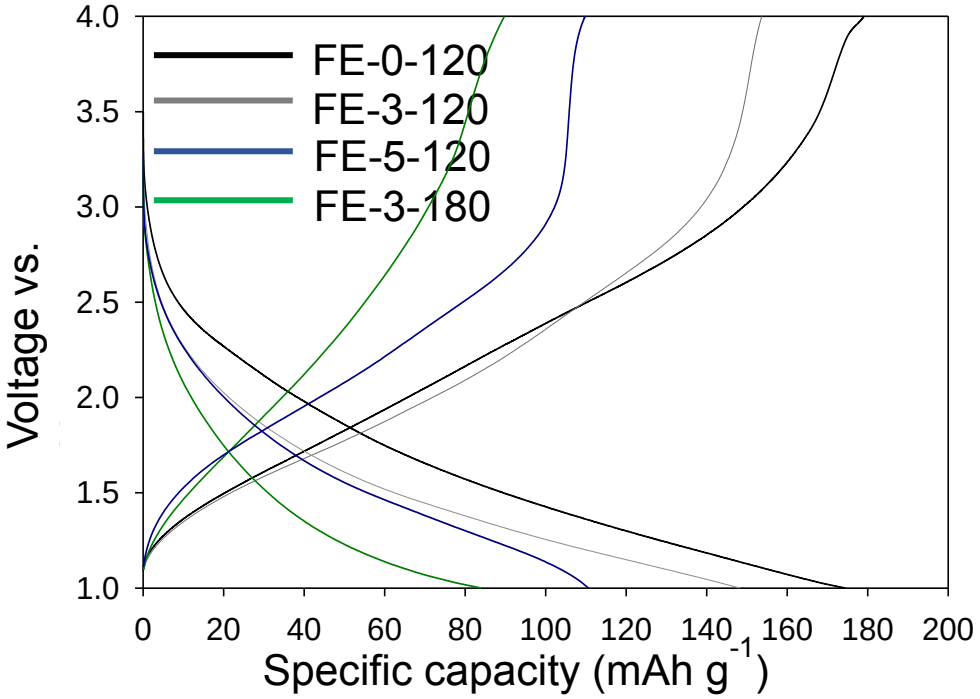

Figure 21. Galvanstatic charge-discharge tests of amorphous, semi-crystalline $Fe(OH)_3$, and high crystalline α-Fe_2O_3 cathodes for the 3rd cycle (electrolyte with 1 M $NaClO_4$ in PC; counter/reference metallic Na; voltage range of 1.0-4.0 V vs Na; mass-normalized current of 47 mA g^{-1}).

$Fe(OH)_3$ nanoparticles exhibited a discharge capacity of 173 mA h g^{-1}, which is much higher than crystalline α-Fe_2O_3 cathodes showing only ~83 mA h g^{-1}. In addition, two semi-crystalline $Fe(OH)_3$ nanosheets delivered discharge capacities of 148 mA h g^{-1} and 111 mA h g^{-1}, respectively, which are lower than the amorphous counterpart but higher than crystalline α-Fe_2O_3, suggesting that lower degrees of structural order improves Na-ion storage at a low current rate.

3.1.5.2 Rate Capability of Amorphous, Semi-Crystalline $Fe(OH)_3$, and Crystalline α-Fe_2O_3 Cathodes

The rate performance of the amorphous and crystalline materials was also investigated, as shown in Figure 22. Cells were cycled galvanostatically at different the mass-normalized current of 47 mA h g^{-1}, 85 mA h g^{-1}, 237 mA h g^{-1}, 472 mA h g^{-1}, and 934 mA h g^{-1}. The C rates were also calculated and shown in Table 8. At lower current rates of 47 mA h g^{-1} and 85 mA h g^{-1}, the discharge capacities of amorphous $Fe(OH)_3$ nanoparticles are higher than that of other two semi-crystalline $Fe(OH)_3$ nanosheets, and crystalline α-Fe_2O_3 cathodes. Nevertheless, when cells were charged/discharged at a higher rate of 237 mA g^{-1}, a lower degree of semi-crystalline $Fe(OH)_3$ nanosheets, the FE-3-120 sample, exhibited a higher discharge capacity of 108 mA h g^{-1}, which is higher than that of amorphous $Fe(OH)_3$ nanoparticles (FE-0-120), with a discharge capacity of 72 mAh g^{-1}, a higher degree of semi-crystalline $Fe(OH)_3$ nanosheets (FE-5-120), and crystalline α-Fe_2O_3 nanoparticles (FE-3-180). At the highest current of 934 mA g^{-1}, the discharge capacity (85 mA h g^{-1}) of a lower degree of semi-crystalline $Fe(OH)_3$ nanosheets (FE-3-120) is ~3.3 times higher than that of high crystalline α-Fe_2O_3 counterparts (26 mA h g^{-1}). Table 8 shows the discharge capacities of four iron-containing materials at different current rates.

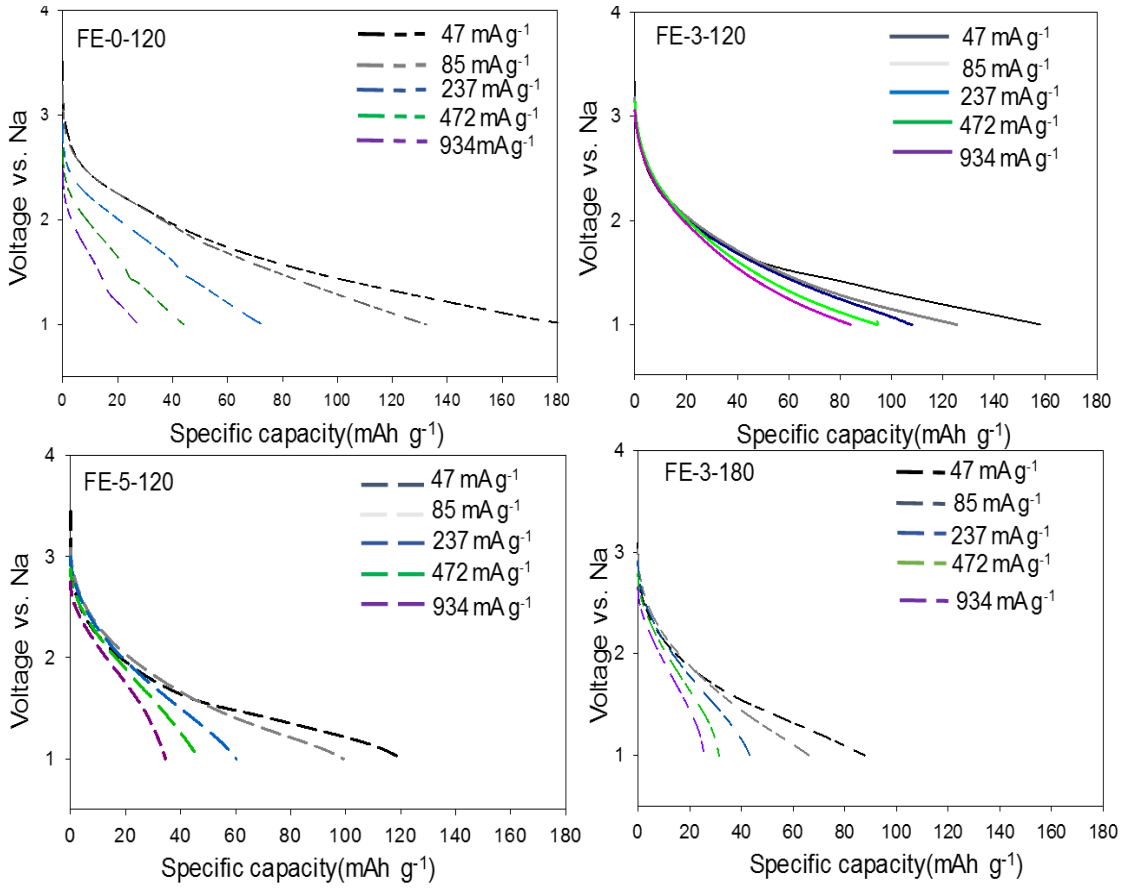

Figure 22. Rate capability of amorphous, semi-crystalline $Fe(OH)_3$, and high crystalline α-Fe_2O_3 cathodes (electrolyte with 1 M $NaClO_4$ in PC; counter/reference metallic Na; voltage range of 1.0-4.0 V vs Na).

Table 8. Average discharge capacities of amorphous, semi-crystalline $Fe(OH)_3$, and crystalline α-Fe_2O_3 cathodes at different current rates (the 2nd cycle).

Material ID	Average discharge capacity (mAh g^{-1}) at mass normalized current				
	47 mA g^{-1} (0.3 C)	85 mA g^{-1} (0.8 C)	237 mA g^{-1} (1.7 C)	472 mA g^{-1} (3.6 C)	934 mA g^{-1} (7.6 C)
FE-0-120	185	132	73	44	27
FE-3-120	158	125	100	95	84
FE-5-120	115	91	57	43	33
FE-3-180	97	69	46	38	24

3.1.5.3 Cycling Stability of Amorphous, Semi-Crystalline $Fe(OH)_3$, and Crystalline α-Fe_2O_3 Cathodes

Cycle performance is an essential parameter of electrode materials, and it is critical to investigate the effect of the degree of crystallinity on the cycling stability of iron hydroxide/oxide materials. All the samples were galvanostatically cycled for 30 cycles at a mass-normalized current of 20 mA g^{-1}. As shown in Figure 23, in the first cycle, amorphous $Fe(OH)_3$ nanoparticles exhibited a slightly higher discharge capacity of ~ 213.5 mAh g^{-1} than that of two semi-crystalline $Fe(OH)_3$ nanosheets with discharge

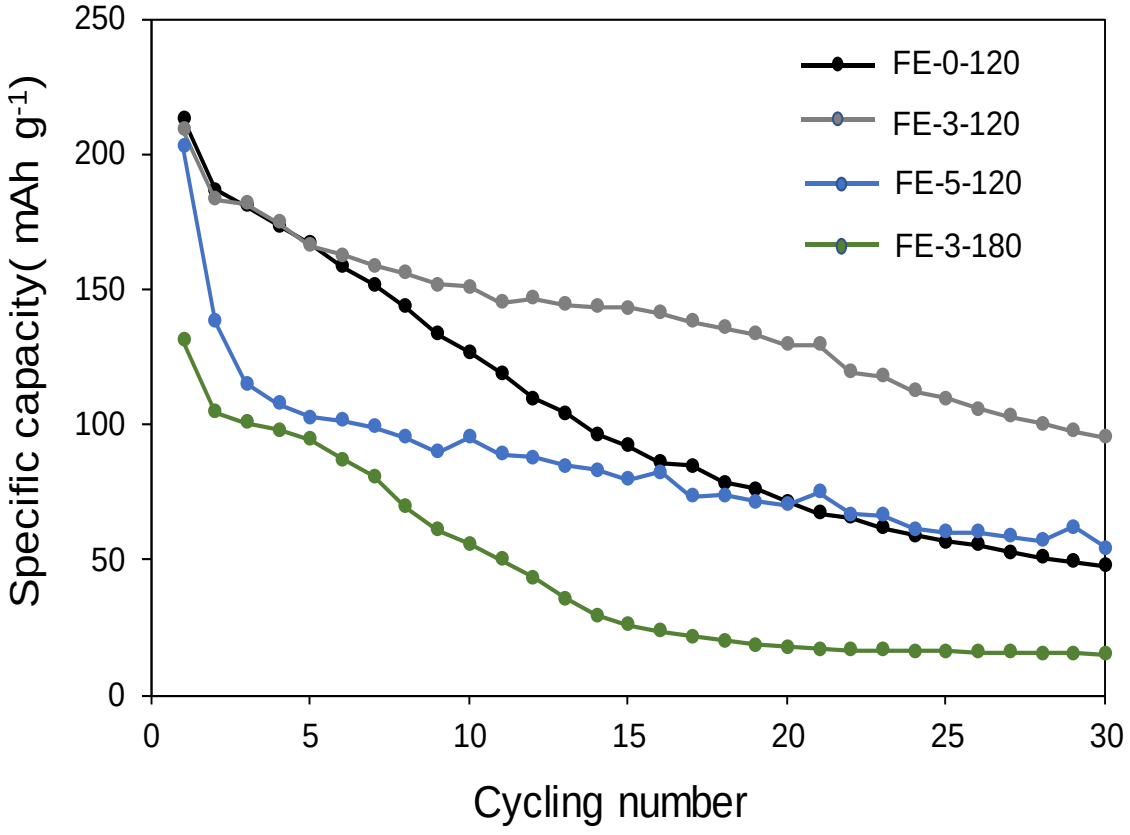

Figure 23. Cycling stability of amorphous, semi-crystalline $Fe(OH)_3$, and high crystalline α-Fe_2O_3 cathodes (electrolyte with 1 M $NaClO_4$ in PC; counter/reference metallic Na; voltage range of 1.0-4.0 V vs Na).

capacities of ~209.2 mAh g^{-1} and 202.5 mAh g^{-1}, respectively and much higher than that

of high crystalline α-Fe_2O_3 nanoparticles (~131.3 mAh g^{-1}). However, upon cycling, amorphous $Fe(OH)_3$ nanoparticles, FE-0-120, exhibited severe capacity degradation and only have a ~25.8% capacity retention after 30 cycles. By contrast, the lower degree of semi-crystalline $Fe(OH)_3$ nanosheets, FE-3-120, achieved ~95.1 mAh g^{-1} for the 30th cycle, showing a much better cycling stability with ~53.4% capacity retention compared to that of amorphous $Fe(OH)_3$ nanoparticles, FE-0-120, the higher degree of semi-crystalline $Fe(OH)_3$ nanosheets (~39.3% capacity retention), FE-5-120, and crystalline α-

Table 9. Average capacity retention and coulombic efficiency of amorphous, semi-crystalline $Fe(OH)_3$, and high crystalline α-Fe_2O_3 cathodes at different current rate (the 2nd to 30th cycle).

Material ID	Average capacity retention (%)	Average coulombic efficiency (%)
FE-0-120	25.8	98.9
FE-3-120	53.4	97.7
FE-5-120	39.3	86.2
FE-3-180	14.5	89.8

Fe_2O_3 nanoparticles (~14.5% capacity retention), FE-3-180, respectively. The average capacity retention and coulombic efficiency (CE) of four samples are shown in Table 9. The amorphous and a lower degree of semi-crystalline $Fe(OH)_3$ nanomaterials exhibited much higher coulombic efficiency compared to the higher degree of semi-crystalline $Fe(OH)_3$ and crystalline α-Fe_2O_3.

Based on results of electrochemistry tests, it was found that amorphous $Fe(OH)_3$ nanoparticles did not exhibit the best electrochemical properties as expected. Surprisingly, on the one hand, a lower degree of semi-crystalline $Fe(OH)_3$ nanosheets have a better rate capability and cycling stability than that the amorphous counterpart, which seemed to be contrary to prior studies.[138, 150] On the other hand, within the other

three samples except amorphous $Fe(OH)_3$ nanoparticles, the amorphization process indeed improved the Na-ion charge storage and structure stabilization.

In addition to the degree of crystallinity, other factors, such as electronic conductivity,[220] morphology,[221] particle size,[222] and charge-transfer at the interface,[223] significantly affected the electrochemical active of charge-carrying ions at high current rates. In particular, the electronic conductivity is highly important for retaining high capacities upon cycling.[60] Therefore, the electronic conductivity and the Na-ion diffusivity may have great influence on electrochemical performance of iron hydroxide/oxide cathodes.

3.1.6 Study of Na-Ion Diffusivity and Electric Properties Within Amorphous, Semi-Crystalline $Fe(OH)_3$, and Crystalline α-Fe_2O_3 Cathodes

3.1.6.1 Cyclic Voltammograms (CVs) of Amorphous, Semi-crystalline $Fe(OH)_3$, and Crystalline α-Fe_2O_3 Cathodes at Different Scan Rates

To understand the effect of the degree of structural order on Na-ion diffusion with amorphous, semi-crystalline, and high crystalline iron hydroxide/oxides cathodes, cyclic voltammograms (CVs) of the four samples at different scan rate from 0.1-0.5 mV/s were performed and analyzed. Figure 24 shows the CVs at different scan rates (0.1, 0.2, 0.3, and 0.5 mV s^{-1}) for amorphous $Fe(OH)_3$ nanoparticles. At a low scan rate of 0.1 mV/s, the CV curve exhibited an anodic peak at ~2.0 V vs Na and a cathodic peak at ~1.1 V vs Na. As the increasing scan rate was increased, anodic peaks shifted to more positive potentials, which is consistent with ohmic losses in the electrochemical cell including the electrode.[105]

Shown in Figure 25 are CVs of the lower degree of semi-crystalline $Fe(OH)_3$ nanosheets, there is an anodic peak at ~1.7 V vs Na, which is lower than the potential of the anodic peak of amorphous $Fe(OH)_3$ nanoparticles, indicating amorphous $Fe(OH)_3$ nanoparticles have an increased electric resistance compared to lower semi-crystalline $Fe(OH)_3$ nanosheets.[224] Noticeably, at a higher scan rate of 0.5 mV/s, for the anodic region, besides the predominant peak at ~2.0 V vs Na, there is a peak at ~2.6 V vs Na, which could be due to another type of Na-ion intercalation site that appears as a result of phase/structure transformation after a few cycles.

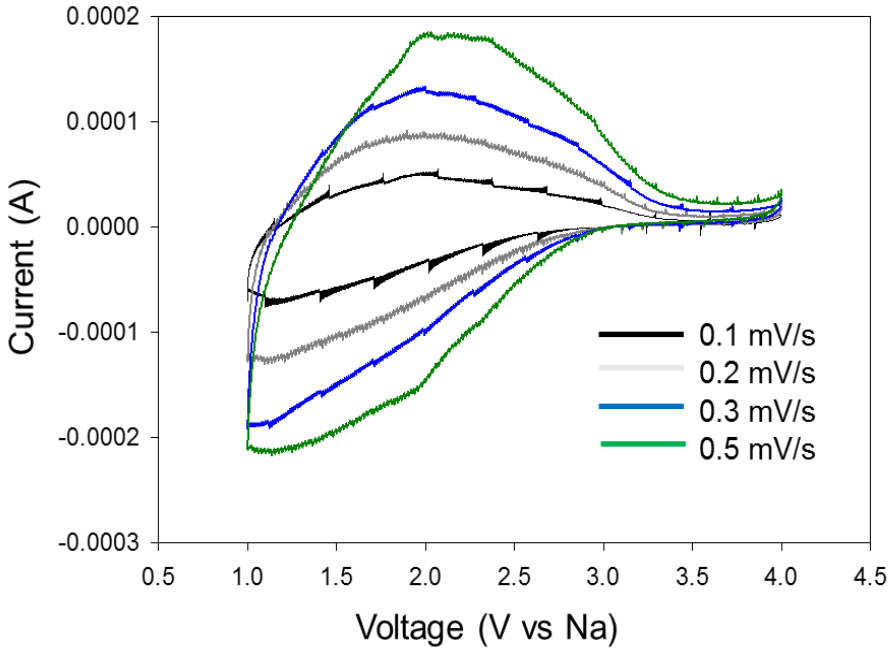

Figure 24. Comparison of CVs of amorphous $Fe(OH)_3$ nanoparticles (FE-0-120) at different scan rates of 0.1, 0.2, 0.3, and 0.5 mV s^{-1}. after a few cycles.

Similarly, shown in Figure 26 are CVs for a higher degree of semi-crystalline $Fe(OH)_3$ nanosheets at different scan rates. At the scan rate of 0.1 mV/s, there is an anodic peak at ~1.7 V vs Na and a cathodic peak at ~1.1 V vs Na. However, at a higher scan rate of 0.5 mV/s, there are two clearly observed anodic peaks at ~1.9 and 2.3 V vs Na, respectively. For the cathodic region, another peak arises at ~2.0 V vs Na. The appearance of the second anodic and cathodic peaks could be attributed to the structure changes during the Na-ion insertion/extraction. Figure 27 shows the CVs of the crystalline α-Fe_2O_3 nanoparticles, FE-3-180, at different scan rates. At a low scan rate,

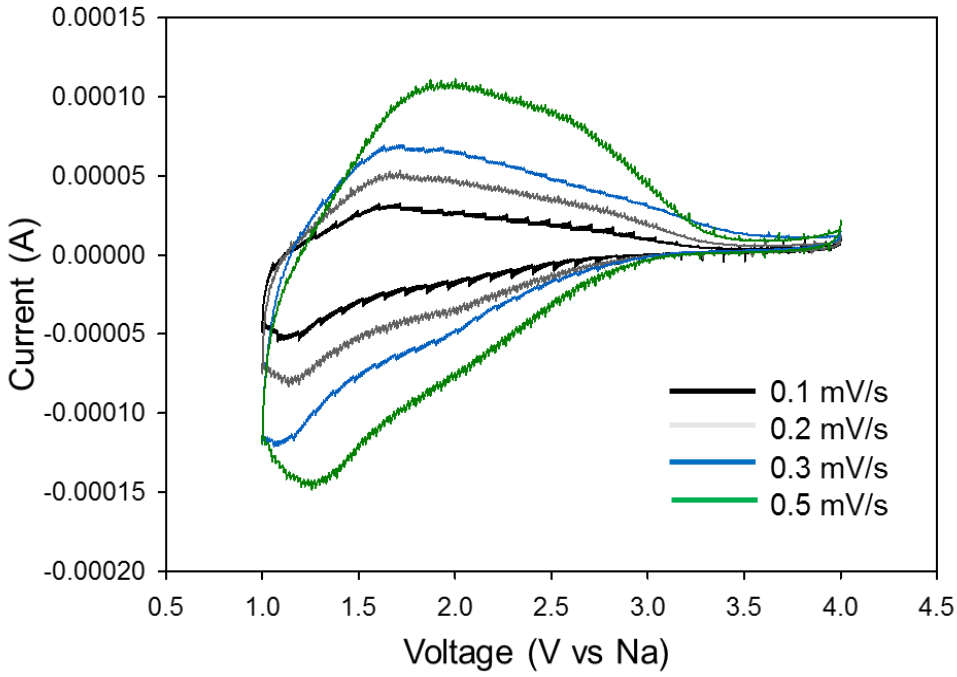

Figure 25. Comparison of CVs of a lower degree of semi-crystalline $Fe(OH)_3$ nanosheets (FE-3-120) at different scan rates of 0.1, 0.2, 0.3, and 0.5 mV s^{-1}.

the anodic peak is centered at ~1.6 V vs Na, which is at a significantly lower positive potential compared to amorphous as well as semi-crystalline $Fe(OH)_3$ nanomaterials,

suggesting that crystalline α-Fe_2O_3 nanoparticles have a lower electronic resistance than that of the other three $Fe(OH)_3$ nanomaterials or insertion occurs at a different potential within the crystalline α-Fe_2O_3 structure.

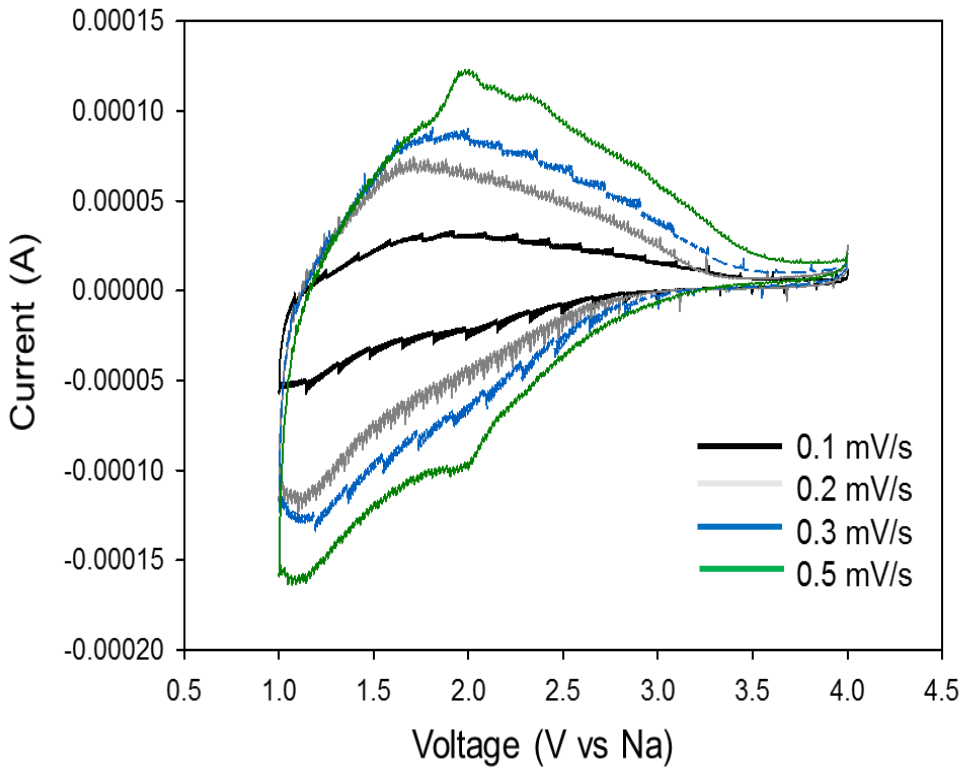

Figure 26. Comparison of CVs of a higher degree of semi-crystalline $Fe(OH)_3$ nanosheets (FE-5-120) at different scan rates of 0.1, 0.2, 0.3, and 0.5 mV s^{-1}.

3.1.6.2 Na-Ion Diffusion Coefficients of Amorphous, Semi-Crystalline $Fe(OH)_3$, and Crystalline α-Fe_2O_3 Nanomaterials

The Na-ion diffusion coefficients (D_{cv}, cm^2s^{-1}) within $Fe(OH)_3$ and α-Fe_2O_3 nanomaterials were calculated according to the Randles-Sevcik equation:[225]

$$I_P = 0.4463zFAC\sqrt{\frac{zFvD_{CV}}{RT}} \quad (27)$$

where I_p is the peak current value (A), z (z=1 for per mole $Fe(OH)_3$ and z=2 for per mole α-Fe_2O_3) is the n umber of electrons, F is the Faraday constant (96485 C mol^{-1}), A is the geometric area of the electrode, C is the Na^+ concentration within the lattice (mol cm^{-3}), ν is the scan rate (V s^{-1}), R is the gas constant (J K^{-1} mol^{-1}), and T is the temperature (K).

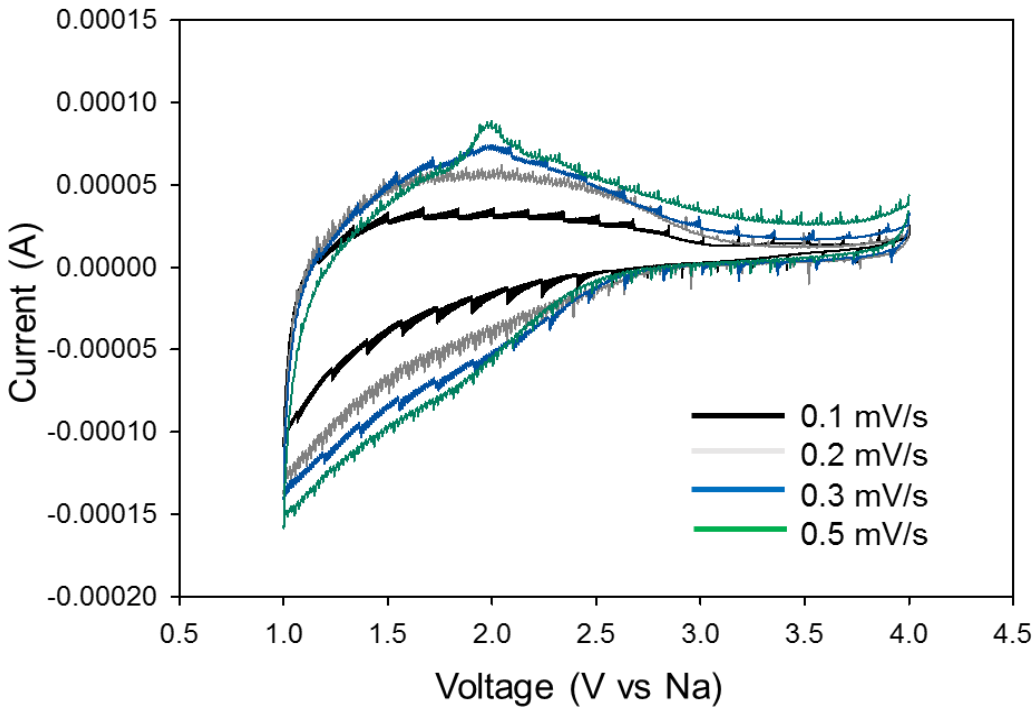

Figure 27. Comparison of CVs of high crystalline α-Fe_2O_3 nanoparticles (FE-3-180) at different scan rates of 0.1, 0.2, 0.3, and 0.5 mV s^{-1}.

In order to determine if the Na-ion charge storage follows diffusion-controlled kinetics, the current peak values (I_p) versus different scan rates was plotted. As shown in Figure 28, all four plots exhibited a linear behavior but with different slopes, suggesting that semi-infinite Na-ion diffusion process occur during the electrochemical reaction, but each cathode material has different Na-ion diffusivities.[226] The obtained diffusion coefficients are shown in Table 10. As the degree of crystallinity decreases, the diffusion coefficients increases, demonstrating that the disorder structure of iron hydroxide/oxides cathode promotes Na-ion diffusion within the structure.

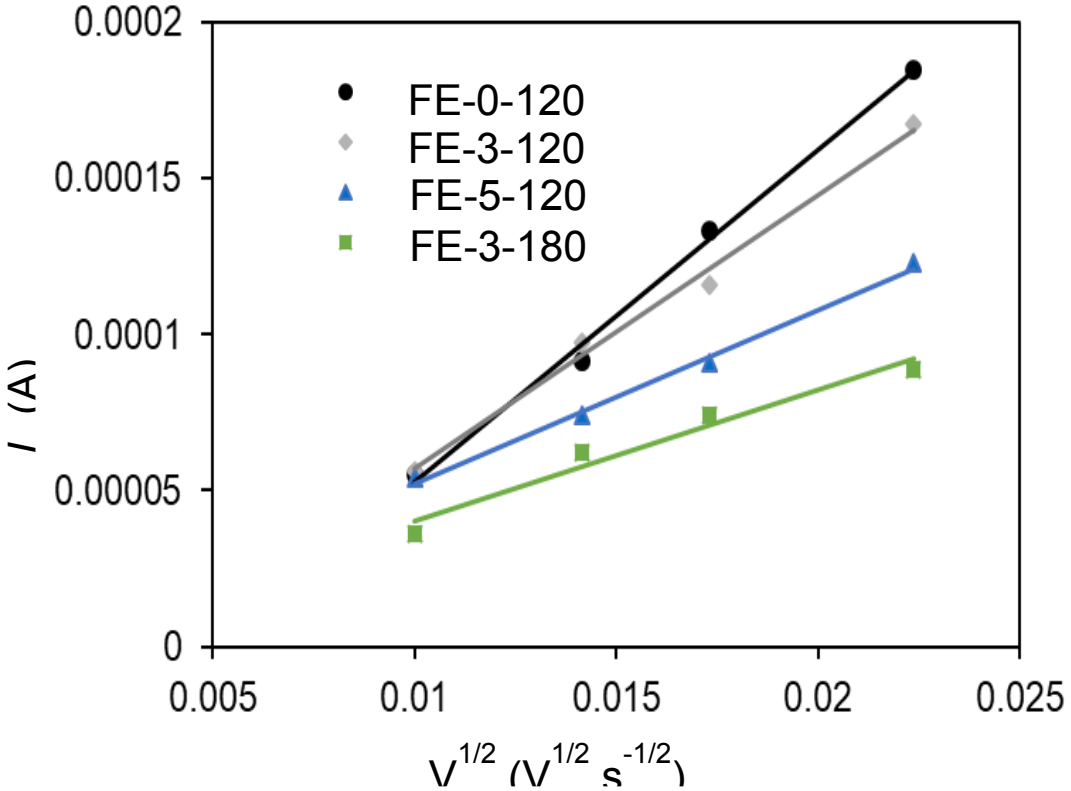

Figure 28. Peak current (I_p, A) vs. square root of scan rate ($V^{1/2}$, $V^{1/2}$ $s^{-1/2}$) and related linear fit within $Fe(OH)_3/\alpha\text{-}Fe_2O_3$ with different degrees of crystallinity.

Table 10. Diffusion coefficients of amorphous, semi-crystalline $Fe(OH)_3$, and high crystalline α-Fe_2O_3 cathodes

Material ID	Diffusion coefficient (D_{cv}, cm^2s^{-1})
FE-0-120	2.76×10^{-12}
FE-3-120	2.00×10^{-12}
FE-5-120	1.24×10^{-12}
FE-3-180	2.53×10^{-13}

3.1.6.3 Electronic Conductivities of Amorphous, Semi-Crystalline $Fe(OH)_3$, and Crystalline α-Fe_2O_3 Nanomaterials

Amorphous materials typically have a lower electronic conductivity than that of crystalline counterparts.[227-228] Electronic conductivities of these four materials with different degrees of crystallinity were obtained via a two-point probe method (shown in Table 11), and as expected, it was found that as the degree of structural order increases, electronic conductivities exhibit a proportional enhancement. Therefore, the better rate capability of a low degree of semi-crystalline $Fe(OH)_3$ than that of the amorphous counterpart can be explained in part as the combined contribution of ionic and electronic conductivities, which is consistent with prior work on manganese oxides.[220] In addition, the worse cycling stability of amorphous $Fe(OH)_3$ nanoparticles compared with a lower degree of semi-crystalline $Fe(OH)_3$ nanosheets could be influenced by its lower electronic conductivity.[60]

Table 11. Electronic conductivities of amorphous, semi-crystalline $Fe(OH)_3$, and high crystalline α-Fe_2O_3 cathodes

Material ID	σ_{elec} (S/cm)
FE-0-120	9.9×10^{-10}
FE-3-120	3.4×10^{-9}
FE-5-120	4.6×10^{-9}
FE-3-180	5.5×10^{-9}

3.2 Development of Novel High-Performance Low Crystalline Iron Oxide (α-Fe_2O_3)/Reduced Graphite Oxide (rGO) Cathodes for Na-Ion Storage

3.2.1 Characterization of As-Prep Reduced Graphite Oxides(rGO)

3.2.1.1 X-Ray Diffraction Analysis of Pristine Graphite, Graphite Oxides (GO), and Reduced Graphite Oxides (rGO)

The crystal structures of pristine graphite, graphite oxides (GO), and reduced graphite oxides (rGO) were characterized using XRD as shown in Figure 29. Pristine graphite exhibited a sharp peak at 2θ ~26.4°, which corresponds to the diffraction of (002) planes with an interlayer distance of 0.337 nm calculated using Bragg's law as described below:[229]

$$2d\sin\theta = n\lambda \tag{28}$$

where n is a positive integer (n=1), λ is the wavelength of the incident wave (λ = 1.54060 Å), θ is the scattering angle, and d is the interlayer distance of separated lattice planes. The diffraction peak of GO shifts to 2θ ~10.38° and the corresponding interlayer spacing was expanded to 0.852 nm, which is a result of the introduction of a number of oxygen-containing groups on the layers, which increase the distance between the graphitic layers upon oxidation.[230] However, after reduction of GO in argon, reduced graphite oxide

(rGO), the peak at 2θ =10.38° disappears and no obvious peaks are observed, indicating the resulting materials become amorphous. After reduction in a high temperature, the graphitic layers may distribute randomly and therefore not have long-range order.

3.2.1.2 Analysis of As-Prep rGO Using Raman Spectroscopy

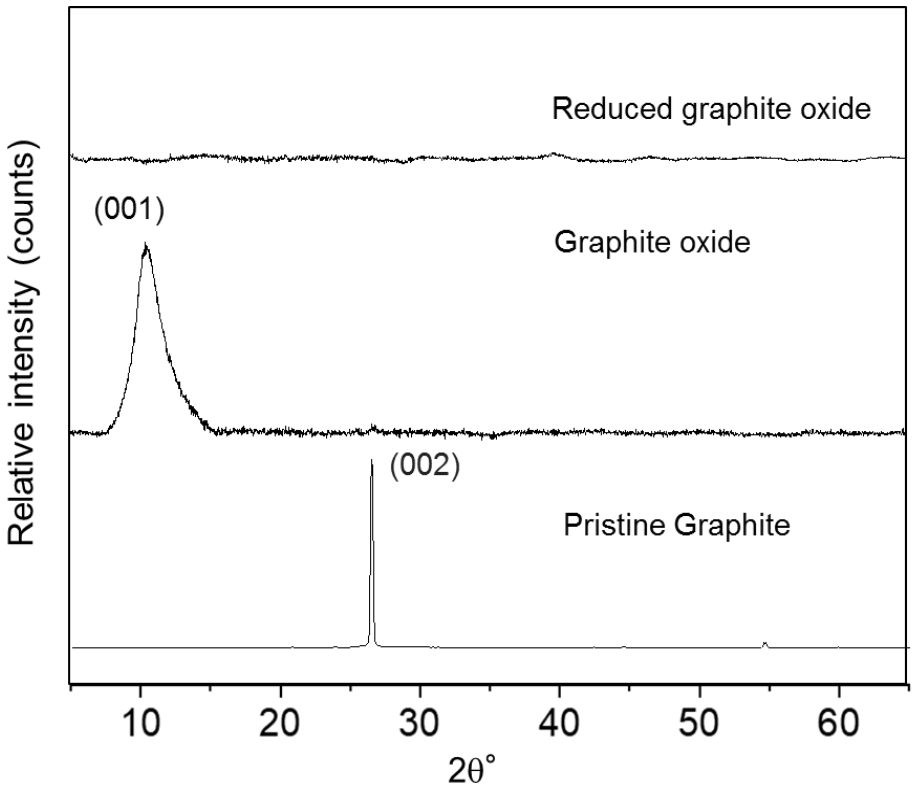

Figure 29. XRD patterns of pristine graphite, GO, and rGO.

Raman spectroscopy was used to characterize the structure and quality of rGO. As shown in Figure 30, the Raman spectrum of rGO shows two distinct major peaks at 1363 and 1601 cm^{-1}, corresponding to the typical D-band and G-band, respectively. The G-band reflects the hexagonal structure associated with the E_{2g} vibration mode of sp^2 hybridized carbon atoms, and the D-band is related to the disordered A_{1g} breathing mode of the six-fold aromatic ring near the basal edge and structural defects of the sp^2 domain.[231-232] The ratio of D and G bands intensities, I_D/I_G, is used to characterize the degree of disorder in graphene-related nanomaterials.[233] The D-/G-band ratio was

calculated to be 0.89, suggesting that the ordered hexagonal structure is several nanometers in size.[232] Thus, the amorphous carbon structure comprises numerous nanometer-sized crystallites with random orientation. As the defect density increases, I_D/I_G decreases due to a more amorphous graphitic domain.[234]

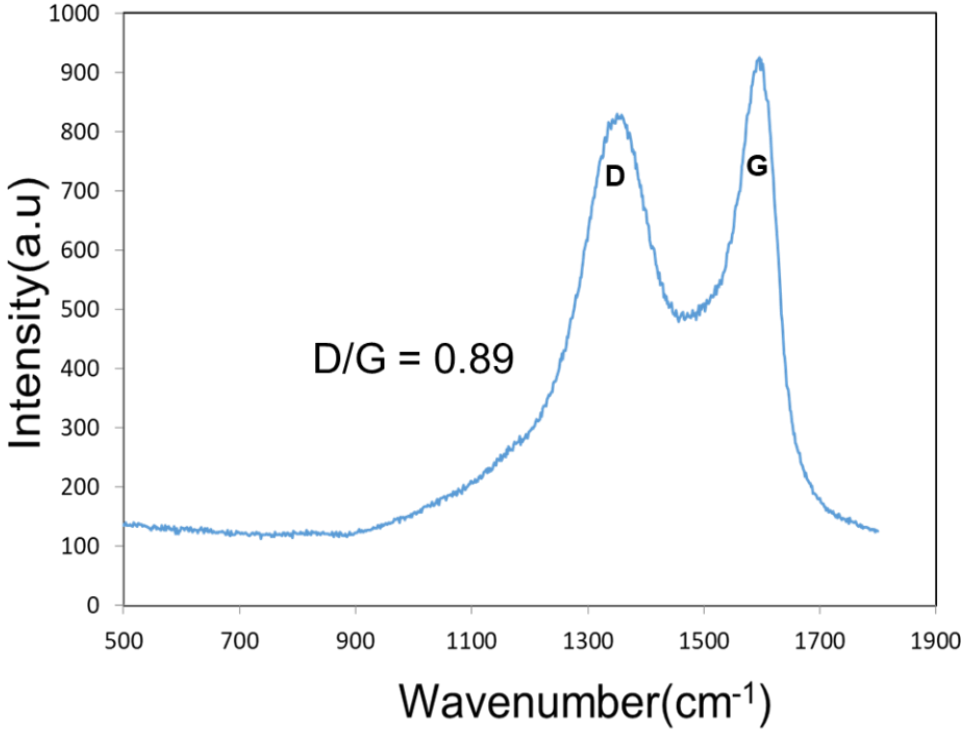

Figurer 30. Raman spectra of as prep rGO.

3.2.1.3 Morphological Analysis of As-Prep rGO Using TEM

The morphological characteristics of as prep rGO was examined using TEM. Figure 31 shows reduced graphite oxides have a thin extended sheet-like structure, which is similar to graphene nanosheets and thus may have a high surface area.

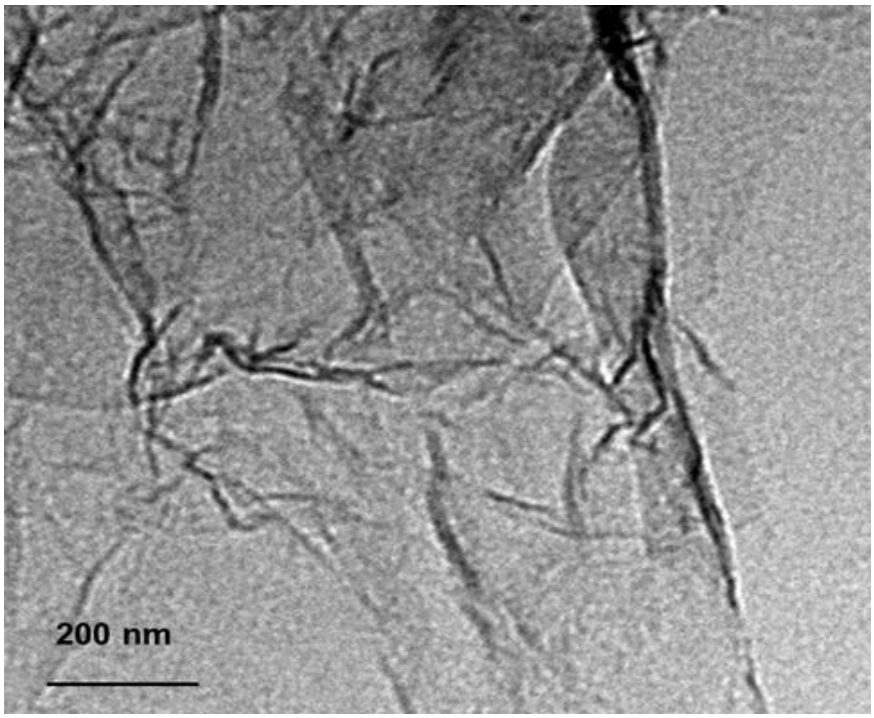

Figure 31. Transmission electron microscopy (TEM) image of rGO.

3.2.1.4 TGA Analysis of As-Prep rGO

Figure 32 displays the TGA curve of rGO that shows weight loss as a function of temperature under an air atmosphere from room temperature to 600 °C. The as-prep rGO sample showed a weight loss of ~10 % from room temperature to 300 °C, which was attributed to the removal of moisture on the surface and the oxygen-containing functional

groups.[235] In a temperature range from 300°C to 450°C, a significant weight loss was observed as a result of decomposition of carbon.[236]

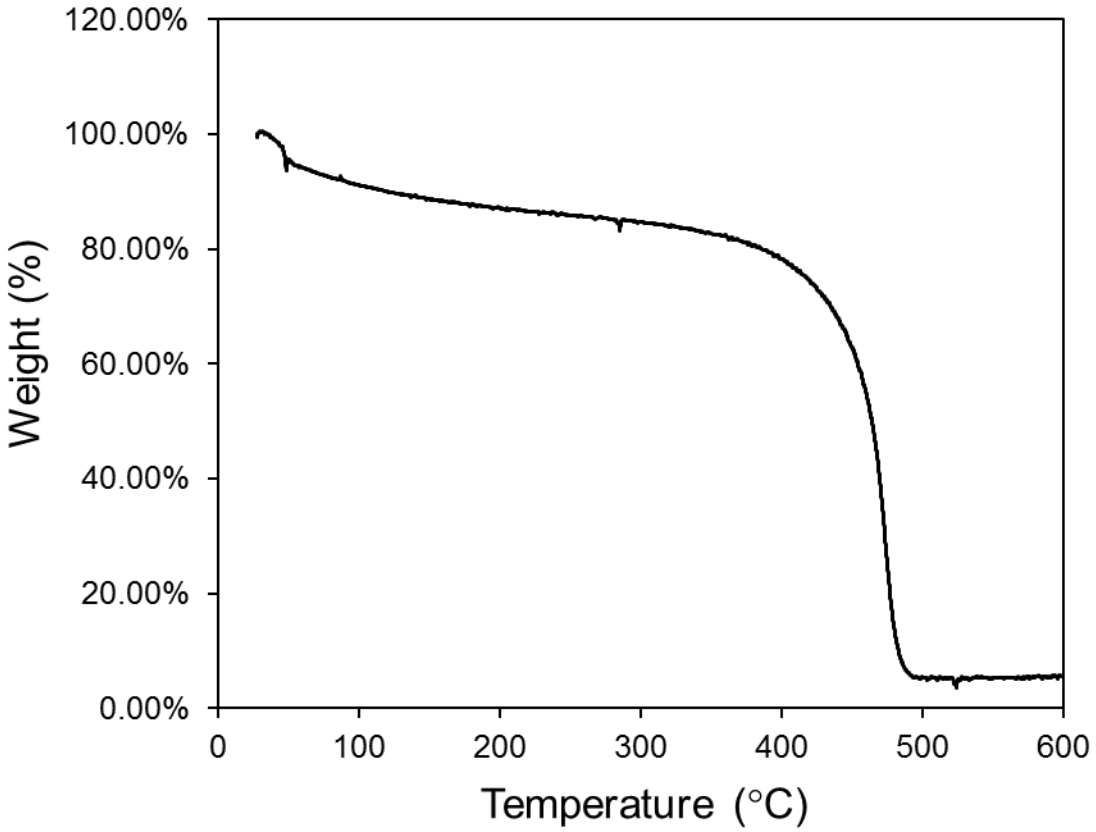

Figure 32. TGA curves of as-prep rGO.

3.2.1.5. The Na-Ion Storage Behavior of rGO nanosheets As Cathodes

Galvanostatic measurements were performed at a mass-nominated current of 37 mA g^{-1} in a voltage range of 1.0-4.0 V and the charge-discharge profile of rGO cathode is shown in Figure 33. The rGO cathodes exhibited a reasonable discharge capacity of 120 mAh g^{-1} during the second cycle, which is much higher compared to the reported literature where a rGO cathode showed a discharge capacity of 78 mAh g^{-1} obtained within a potential between 1.5-4.5 V versus Na metal.[121] Also, it has been reported that rGO exhibited a discharge capacity of 240 mAh g^{-1} within a wider potential between 1.2 and 4.5 V versus Na metal at a current rate of 30 mA g^{-1}.[237]

3.2.1.6 Cyclic Voltammogram (CV) of rGO

CV tests were performed to evaluate the sodium-ion storage behavior of the rGO cathode. Figure 34 shows the CV plot of rGO at a scan rate of 1 mV s^{-1} in a voltage range of 1.0–4.0 V vs Na. The CV curve of the rGO cathode exhibited a broad shape without obvious peaks, suggesting that there are multiple storage sites instead of a single site interacting with Na^+. Furthermore, the typical rectangular shape for both anodic and cathodic regions is displayed, indicating that Na-ion storage follows a pseudocapacitance behavior, which is usually observed in supercapacitor-based materials.[237-238] The shape of the CV curve indicates that the reaction mechanism in the rGO cathode is confined to the

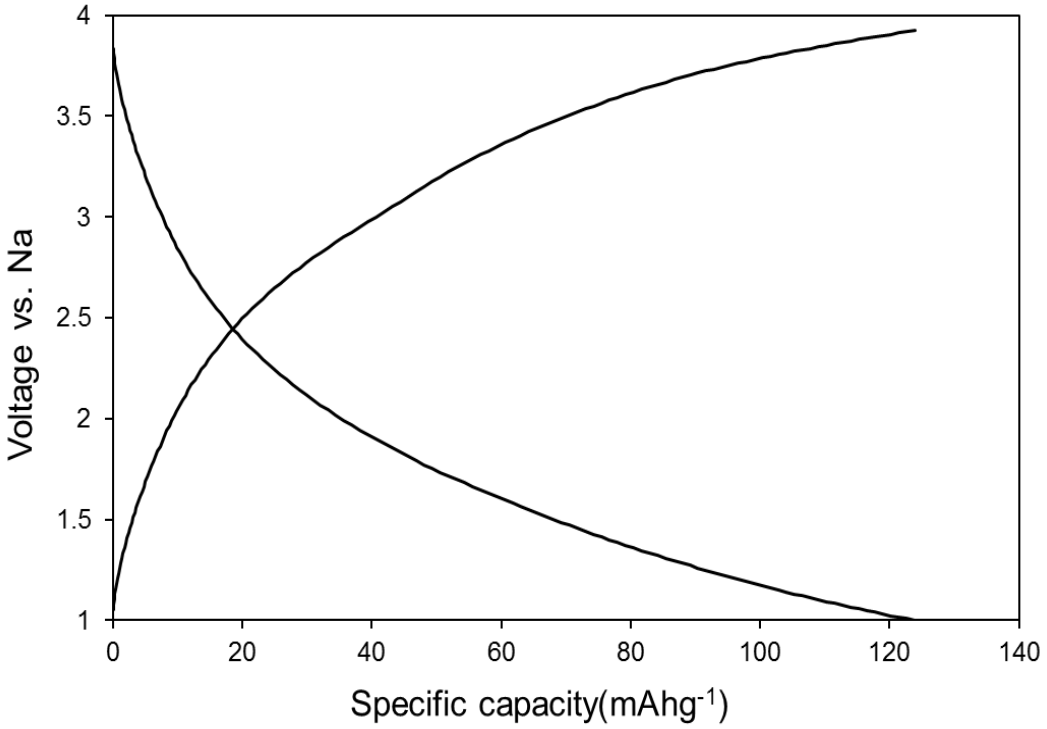

Figure 33. Galvanostatic charge and discharge voltage profiles (second cycle) of rGO nanosheets (electrolyte 1 M $NaClO_4$ in PC; counter/reference metallic Na).

surface reactions but is not diffusion-limited.[239]

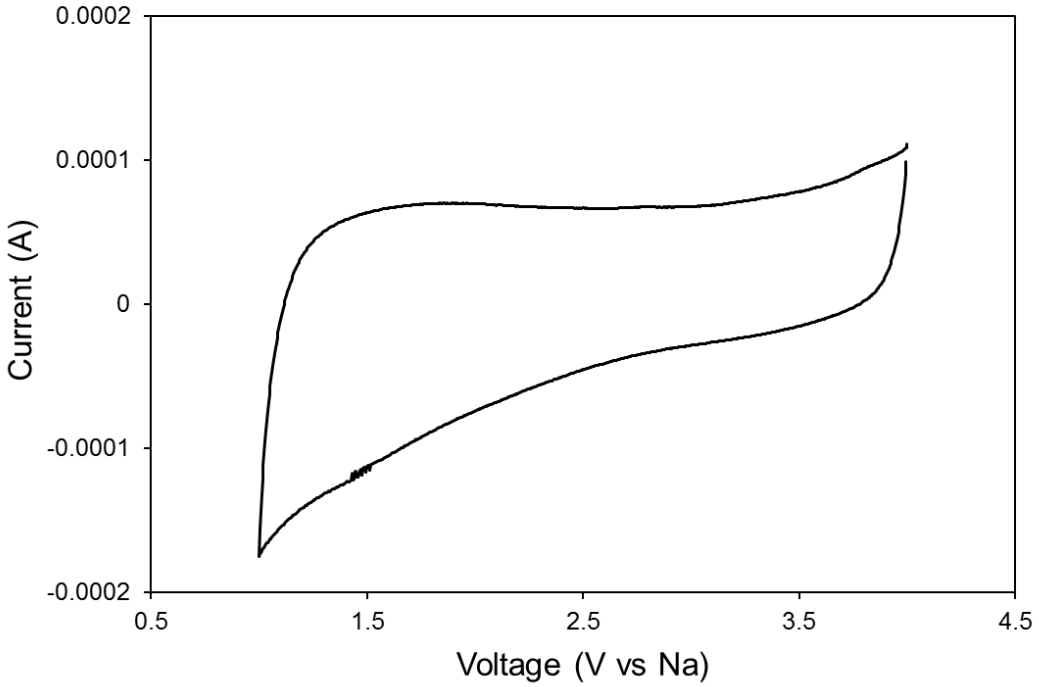

Figure 34. CV scan of rGO at a scan rate of 1 mV s^{-1} in a voltage range of 1.0–4.0 V vs Na.

3.2.2 Characterization of Pristine α-Fe_2O_3 Nanoparticles and α-Fe_2O_3/rGO Nanocomposites

3.2.2.1 Scanning Electron Microscopy Analysis

FeO_x nanomaterials and FeO_x/rGO nanocomposites were prepared via a microwave synthesis, which took 5 minutes at 120 °C in pure aqueous solution. Figure 35 shows the morphologies of the commercial α-Fe_2O_3, the pristine FeO_x, and FeO_x/rGO nanocomposites. Both commercial α-Fe_2O_3 and the pristine FeO_x exhibited a roughly sphere or nanoparticle shape and aggregate together. In contrast, for FeO_x/rGO

nanocomposites, the FeO_x nanoparticles appear to be randomly dispersed on rGO nanosheets.

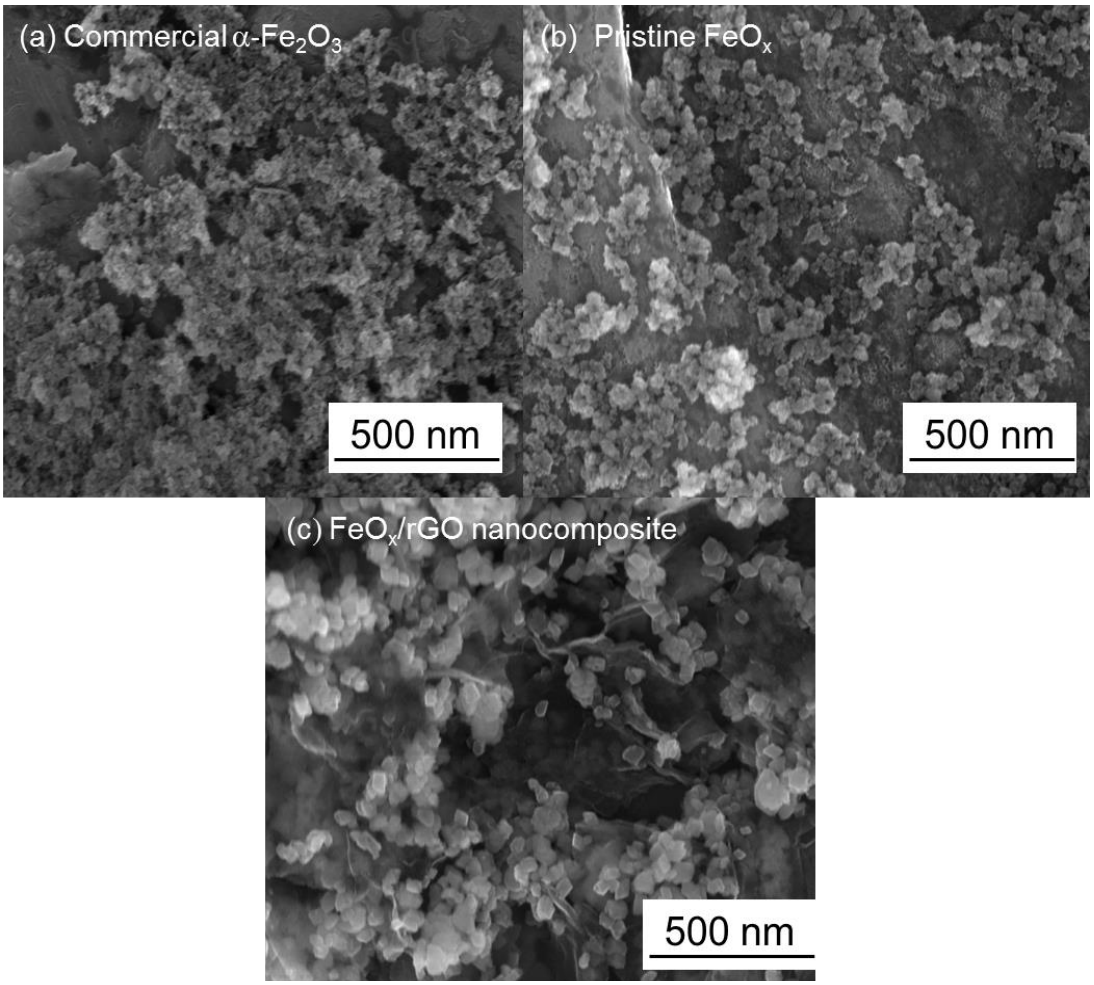

Figure 35. SEM images of (a) the commercial α-Fe_2O_3, (b) pristine FeO_x, (c) FeO_x/rGO nanocomposites.

3.2.2.2 X-Ray Diffraction

XRD was performed in order to examine the phase and crystallinity of the obtained materials. Figure 36 presents the XRD patterns of products formed by rapid microwave heating with and without rGO as well as commercial α-Fe_2O_3 nanoparticles for comparison. According to their XRD patterns, The phase of two obtained products is

well indexed to the α-Fe_2O_3 phase. Furthermore, the low degree of crystallinity of these two products are also demonstrated by the XRD spectra, showing broader and much

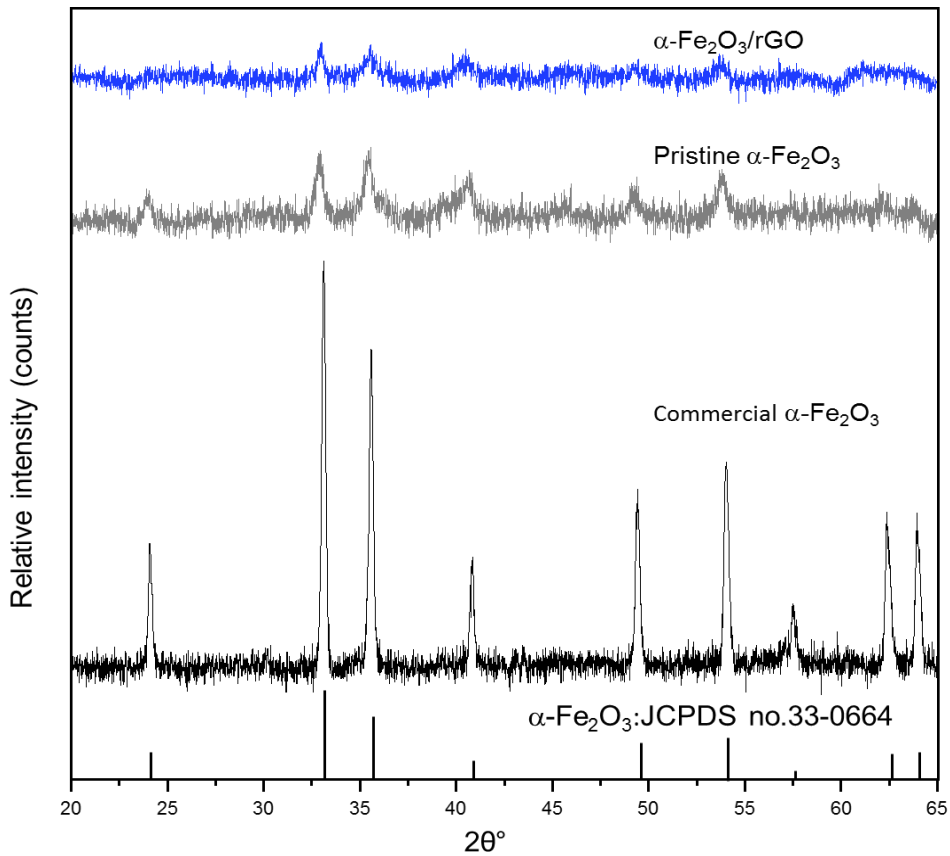

Figure 36. XRD patterns of high crystalline commercial α-Fe_2O_3, low crystalline α- Fe_2O_3,and α-Fe_2O_3/rGO nanocomposites.

lower intensity peaks compared to the sharp and high intensity peaks of commercial α-Fe_2O_3 nanoparticles. The XRD peaks of α-Fe_2O_3/rGO nanocomposites are slightly broader and less intense than that of pristine α-Fe_2O_3 nanoparticles due to integration of rGO promote the amorphization of α-Fe_2O_3 growth. The formation mechanism for α-Fe_2O_3 in pure aqueous solution was proposed as follows:[183, 240]

$$H_2O + H_2O \overset{\Delta}{\leftrightarrow} H_3O^+ + OH^- \quad (27)$$

$$Fe^{3+} + 6H_2O \rightarrow [Fe(OH_2)_6]^{3+} \quad (28)$$

$$[Fe(OH_2)_6]^{3+} + 3OH^- \xrightarrow{\Delta} Fe(OH)_3 \quad (29)$$

$$Fe(OH)_3 \xrightarrow{\Delta} \alpha\text{-}Fe_2O_3 + H_2O \quad (30)$$

The low crystalline nature of α-Fe_2O_3 nanoparticles can be attributed to the characteristics of microwave synthesis as well as the pure aqueous reaction medium. Prior studies showed that by using microwave synthesis, pure amorphous or low crystalline α-Fe_2O_3 nanoparticles were obtained because of short reaction time and rapid heating up leading to high structural disorder of products.[182-183] Moreover, in the first objective, it has been found that a higher amount of OH^- groups facilitate the crystallization of $Fe(OH)_3$. In this reaction, the small amount of OH^- groups provided by pure water (without urea and other OH^- reservoirs) via self-ionization contributes to the low crystallinity of pristine α-Fe_2O_3 nanoparticles. With rGO nanosheets, Fe^{3+} may nucleate with oxygen-containing functional groups on the surface of rGO via electrostatic interactions, consequently forming α-Fe_2O_3 nanoparticles that uniformly distribute over the surface of the rGO, which suppress restacking of rGO layers.

The crystallite size of the highly crystalline commercial α-Fe_2O_3 nanoparticles, low crystalline α-Fe_2O_3 nanoparticles, and α-Fe_2O_3/rGO nanocomposites was also calculated based on the Scherrer equation, $L = K\lambda/\beta cos\theta$, in which L is crystallite size, λ (Å) is wavelength, β is full width at half maximum of peaks in radian located at any 2θ in the pattern, K is constant related to crystallite shape, normally taken at 0.9. The θ can be in degrees or radians, since the $\cos\theta$ corresponds to the same number.[241] The crystallite size was determined to be 35.5 nm, 22.5 nm, and 18.3 nm for commercial α-Fe_2O_3

nanoparticles, low crystalline α-Fe_2O_3 nanoparticles, and α-Fe_2O_3/rGO nanocomposites, respectively.

3.2.2.3 TGA Analysis

TGA analysis was mainly used to determine the rGO content in α-Fe_2O_3/rGO nanocomposites as well as the structural water content in pristine α-Fe_2O_3 nanoparticles. Figure 37 shows the TGA plots of commercial α-Fe_2O_3, bare α-Fe_2O_3, and α-Fe_2O_3/rGO nanocomposites from room temperature to 600 °C in air. Commercial α-Fe_2O_3 nanoparticles only exhibited trace amount of weight loss (~0.9%), suggesting there is a very small amount of moisture in the commercial sample. For pristine α-Fe_2O_3 nanoparticles, the weight loss between room temperature to 120 °C is ~3.8%, which can be attributed to elimination of physically absorbed water on the surface. As the temperature was elevated to 350 °C, an clear weight change of ~8.5% was observed, which is attributed to removal of tightly bounded structural water. The chemical formula can be determined as α-Fe_2O_3· 0.53H_2O according to the weight loss. The high content of structural water could be a factor that contributes to the low crystallinity of pristine α-Fe_2O_3. With respective to α-Fe_2O_3/rGO nanocomposites, similar to pristine α-Fe_2O_3 nanoparticles, the weight loss (~3.7%) between room temperature to 120 °C is as a result of removal of loosely bond water. Then, there is a small stage of weight loss below 300°C, which could be ascribed to the loss of functional groups in the rGO and possibly structural water. However, there is significantly sharp drop in weight from 300°C to 400 °C, which is due to the combustion of carbon in air. This is confirmed by the TGA curve of the bare rGO in the same temperature range, as shown in Figure 29. Thus,

according to the above analysis, the weight percentages of carbon content in the α-Fe_2O_3/rGO nanocomposite can be determined to be about ~9.1%.

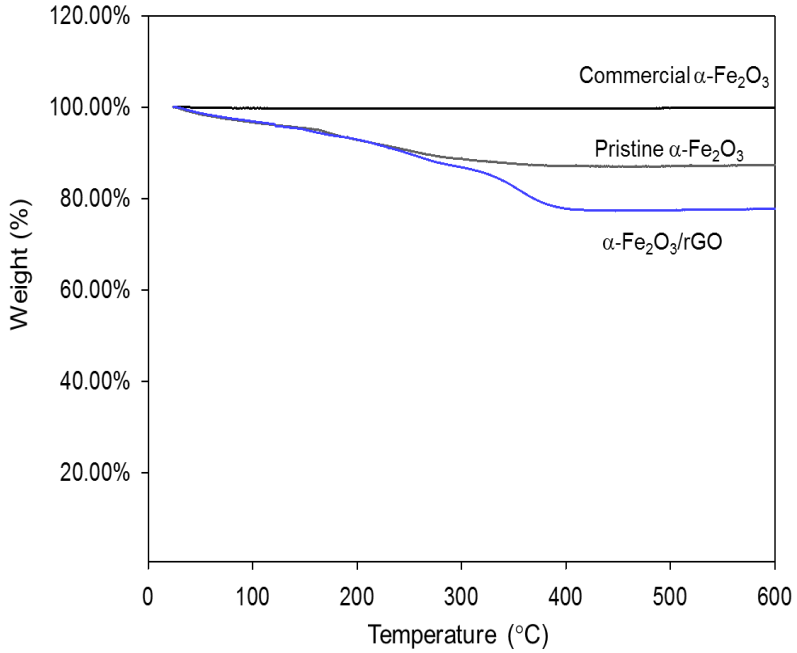

Figure 37. TGA curves of high crystalline commercial α-Fe_2O_3, low crystalline α-Fe_2O_3, and α-Fe_2O_3/rGO nanocomposites.

3.2.3 Electrochemical Properties of High Crystalline Commercial α-Fe_2O_3, Low Crystalline α-Fe_2O_3 and α-Fe_2O_3/rGO Nanocomposites

In order to investigate how the degree of structural order plays a critical role in Na-ion storage for α-Fe_2O_3 cathodes as well as the benefits of rGO for enhancing the electronic conductivity and stability, the electrochemical properties of highly crystalline commercial α-Fe_2O_3 nanoparticles, low crystalline pristine α-Fe_2O_3 nanoparticles, and α-Fe_2O_3/rGO nanocomposites were evaluated. Figure 38 shows the charge and discharge voltage profiles of various cathode materials at a current of 20 mA g^{-1} within a fixed voltage window (1.0 to 4.0 V vs Na) for the third cycle. α-Fe_2O_3/rGO nanocomposites, low crystalline pristine α-Fe_2O_3, and highly crystalline commercial α-Fe_2O_3 exhibited

discharge capacities of 169, 139, and 6 mA h g^{-1} respectively. The discharge capacity of low crystallinity α-Fe_2O_3 nanoparticles is significantly higher (~24.8 times) than that of highly crystalline commercial α-Fe_2O_3 nanoparticles, suggesting that structural disorder indeed improves the charge storage of Na-ion within α-Fe_2O_3 cathodes. Furthermore, a slightly higher specific capacity of α-Fe_2O_3/rGO nanocomposites compared to bare α-Fe_2O_3 nanoparticles could be attributed to additional Na-ion storage from rGO nanosheets, enhanced electronic conductivities or a higher surface area.

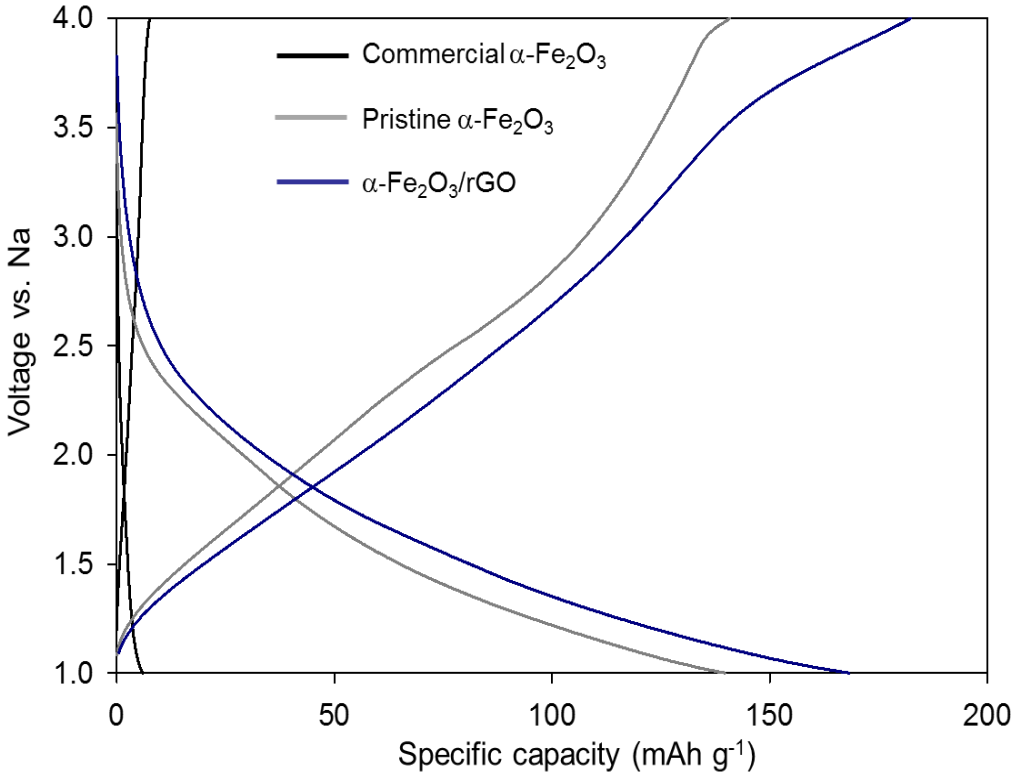

Figure 38. Galvanstatic charge-discharge tests of high crystalline commercial α-Fe_2O_3, low crystalline α-Fe_2O_3, and α-Fe_2O_3/rGO nanocomposites (electrolyte with 1 M $NaClO_4$ in PC; counter/reference metallic Na; voltage range of 1.0-4.0 V vs Na; mass-normalized current of 16.7 mA g^{-1})

Figure 39 illustrates the rate capability of α-Fe_2O_3/rGO nanocomposites, low crystalline pristine α-Fe_2O_3, and high crystalline commercial α-Fe_2O_3 at different mass normalized currents. Initially, cells were cycled at a mass normalized current of 16.7 mAg^{-1} for 5 cycles. α-Fe_2O_3/rGO nanocomposites delivered an initial discharge capacity of 195 mA h g^{-1}, which is higher than that bare α-Fe_2O_3 with an initial discharge of 174 mA h g^{-1}. Noticeably, pristine α-Fe_2O_3 nanoparticles with a low degree of crystallinity showed much higher discharge capacities compared to highly crystalline commercial α-Fe_2O_3 nanoparticles, which only exhibited a discharge capacity of 7.5 mA h g^{-1}, suggesting that α-Fe_2O_3 cathodes with a lower degree of structural order improve the Na-ion charge storage compared to that of highly crystalline counterparts in which Na-ion can barely intercalate/deintercalate into/out of the lattice. The discharge capacities of α-Fe_2O_3/rGO nanocomposites and pristine α-Fe_2O_3 nanoparticles significantly dropped to 170 mA h g^{-1} and 144 mA h g^{-1}, respectively, which could be largely due to the irreversible capacity loss occurred in the formation of solid electrolyte interface (SEI) film.[242] The highly crystalline commercial α-Fe_2O_3 cathodes did not exhibit significant decrease in discharge capacities possibly due to the extremely low initial discharge capacity. As the mass-normalized current rate was increased to 33.6 mA g^{-1}, the discharge capacity of α-Fe_2O_3/rGO nanocomposites was 151 mA h g^{-1}, which is much higher than pristine α-Fe_2O_3 with a discharge capacity of 103 mA h g^{-1}. Furthermore, in the subsequent cycles at the same C-rate**,** the discharge capacities delivered by α-Fe_2O_3/rGO nanocomposites kept constant, whereas the capacities of pristine α-Fe_2O_3

were significantly degraded, indicating α-Fe_2O_3/rGO cathodes have a much better cycling reversibility compared to

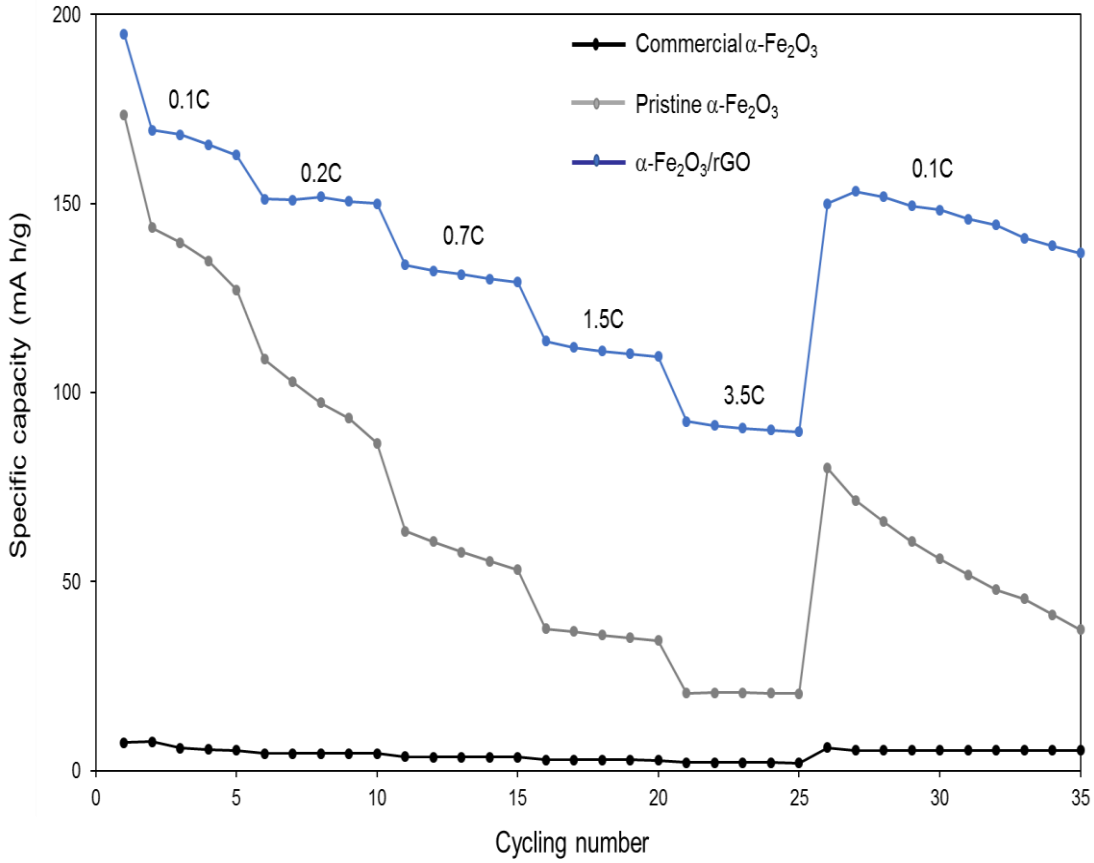

Figure 39. Rate capability tests of high crystalline commercial α-Fe_2O_3, low crystalline α-Fe_2O_3, and α-Fe_2O_3/rGO nanocomposites (electrolyte with 1 M $NaClO_4$ in PC; counter/reference metallic Na; voltage range of 1.0-4.0 V vs Na.) .

that of pristine α-Fe_2O_3. Moreover, at a mass-normalized current of 323 mA g^{-1} (3.5 C, ~17 minutes discharging), α-Fe_2O_3/rGO nanocomposites exhibited a discharge capacity of 91 mA h g^{-1}, whereas pristine α-Fe_2O_3 only delivered a capacity of 21 mA h g^{-1}, which is due to integration of rGO with α-Fe_2O_3 that can drastically enhance the electronic conductivity and Na-ion charge transfer.[242-243] In the first objective, it has been demonstrated that iron based materials with a high degree of structural disorder typically

have poor electronic conductivities. Therefore, low crystalline α-Fe_2O_3 nanoparticles showed a very low discharge capacity at a high rate. When the current rate was returned to 0.1 C, the discharge capacity of the composite powders recovered very well to 153 mA h g^{-1} (90.4% recovery). In contrast, pristine α-Fe_2O_3 nanoparticles only had a discharge capacity of 72 mA h g^{-1} (49.8 % recovery). The discharge capacity of high crystalline commercial α-Fe_2O_3 at a high rate of 3.5 C was extremely low, only ~2.2 mA h g^{-1} due to α-Fe_2O_3 with a highly crystalline structure could have a very poor Na-ion diffusivity that

Table 12. Average discharge capacities of high crystalline commercial α-Fe_2O_3, low crystalline α-Fe_2O_3, and α-Fe_2O_3/rGO nanocomposites at different mass-normalized currents (the 2nd cycle).

Material ID	Average discharge capacity (mAh g^{-1}) at different mass-normalized currents					
	16.7 (0.1C)	33.6 (0.2 C)	83.9 (0.7 C)	168.1 (1.5 C)	323.4 (3.5 C)	16.7 (0.1C)
α-Fe_2O_3/rGO	170	150	129	110	91.7	154
Pristine α-Fe_2O_3	137	101	59.9	35.9	19.3	70.2
commercial α-Fe_2O_3	7.8	4.6	3.6	2.9	2.2	5.4

leads to very low discharge capacities. The average discharge capacities of various cathodes at different current rates are listed in Table 12.

Figure 40 shows the cycling performances of high crystalline commercial α-Fe_2O_3, pristine low crystalline α-Fe_2O_3, and α-Fe_2O_3/rGO nanocomposites at 0.1 C. Pristine low crystalline α-Fe_2O_3 exhibited a very fast capacity fading with only ~10.4%

capacity retention from second cycle 144.9 mA h g^{-1} to 13.3 mA h g^{-1} after 50 cycles, which could be due to the phase transformation/lattice distortion upon Na-ion diffusion.

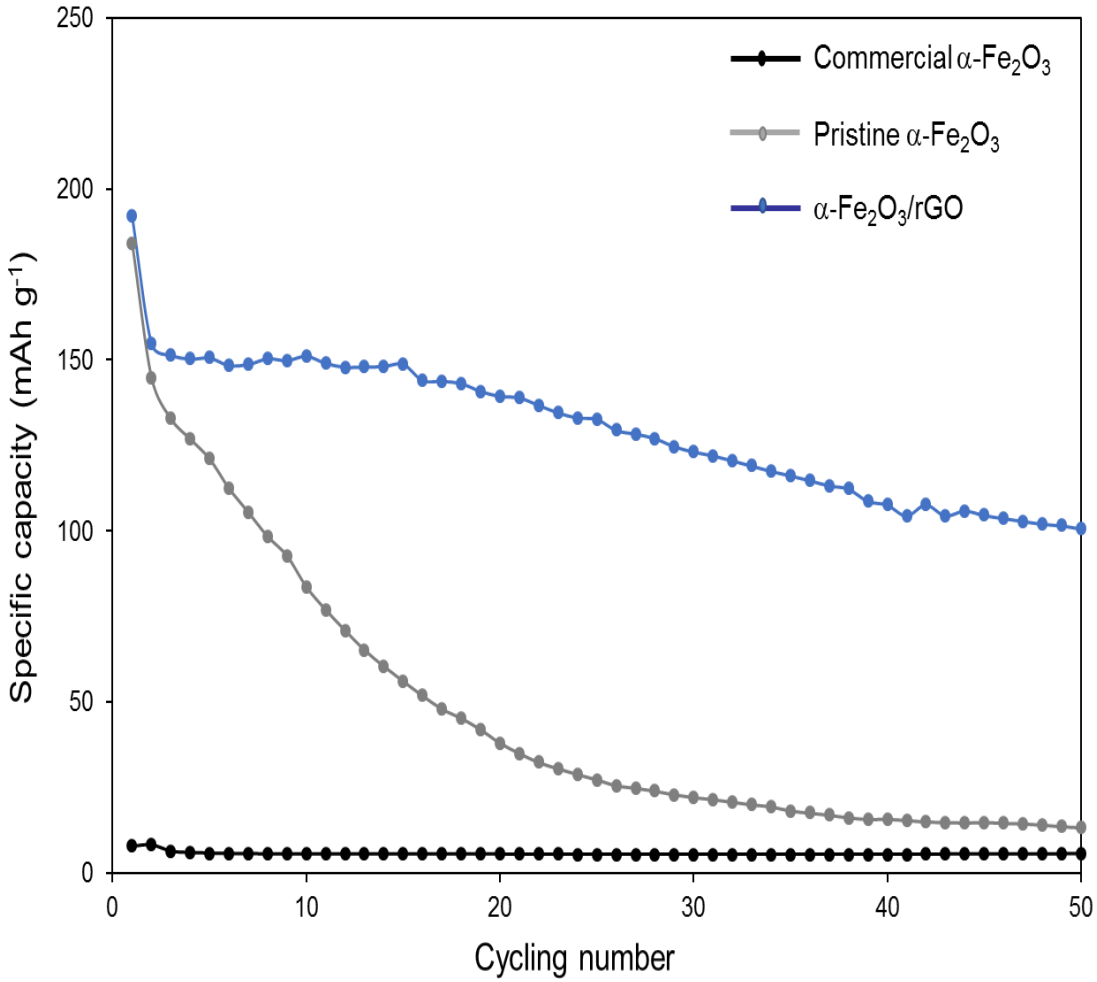

Figure 40. Cycling stability tests of high crystalline commercial α-Fe_2O_3, low crystalline α-Fe_2O_3, and α-Fe_2O_3/rGO nanocomposites (electrolyte with 1 M $NaClO_4$ in PC; counter/reference metallic Na; voltage range of 1.0-4.0 V vs Na; C-rate ~0.1 C (mass-normalized current of 20 mA g^{-1})).

Highly crystalline commercial α-Fe_2O_3 cathodes displayed a 67.5% capacity retention (from second cycle to 50 cycles). However, the discharge capacities were very low. After 50 cycles, commercial α-Fe_2O_3 cathodes only delivered a capacity of 5.7 mA h g^{-1}. On one hand, a low degree of crystallinity is beneficial for α-Fe_2O_3 cathodes to

store Na-ions. However, a significant amount of the large radius Na^+ can substantially distort the lattice and lead to tremendous capacity degradation.[244] In comparison, α-Fe_2O_3/rGO nanocomposites shows a much better cycling performance after 50 cycles. A much higher discharge capacity of 101 mA h g^{-1} was observed after 50 cycles. The substantially improved cycling stability (~61.2% capacity retention) can be attributed to the benefits of rGO. Prior studies have demonstrated that rGO can accommodate the volume change and prevent pulverization of the α-Fe_2O_3 cathodes upon reversible intercalation/deintercalation of ions due to the nature of robustness and flexibility provided by integration of α-Fe_2O_3 with rGO.[245] Furthermore, α-Fe_2O_3/rGO nanocomposites had a higher coulombic efficiency (CE) than that of low crystalline pristine α-Fe_2O_3 nanoparticles and high crystalline commercial α-Fe_2O_3 nanoparticles, as shown in Table 13.

Figure 41 shows the high-rate cycling performances of various cathodes at ~1.7 C (170 mA g^{-1}). At the high current rate, even though high crystalline commercial α-Fe_2O_3 nanoparticles exhibited a very good stability with 96.7% capacity retention after 150 cycles, the discharge capacity was extremely low, ~ 2.9 mA h g^{-1}, indicating only a trace amount of Na^+ diffuse into the rigid crystalline lattice, leading to no/very slight lattice distortion. In comparison, low crystalline α-Fe_2O_3 nanoparticles delivered a much higher discharge capacity of 82.3 mA h g^{-1} for the second cycle, however, the discharge capacity was only 7.9 mA h g^{-1} at the end of 150 cycles, displaying a very serious amount of

Table 13. Average discharge capacity of the 2nd cycle and the 50th cycle, capacity retention, and coulombic efficiency of high crystalline commercial α-Fe_2O_3, low crystalline α-Fe_2O_3, and α-Fe_2O_3/rGO nanocomposites (the 2nd to 50th cycle) at 0.1 C.

Material ID	Discharge capacity (mAh g^{-1}) for the 2nd cycle	Discharge capacity (mAh g^{-1}) for the 50th cycle	Capacity Retention after 50 cycles (%)	Coulombic efficiency (%)
α-Fe_2O_3/rGO	183	111	61	97.0
Pristine α-Fe_2O_3	147	15.3	10.4	94.1
commercial α-Fe_2O_3	7.9	5.4	67.5	96.0

Na^+ diffuse into the rigid crystalline lattice, leading to no/very slight lattice distortion. In comparison, low crystalline α-Fe_2O_3 nanoparticles delivered a much higher discharge capacity of 82.3 mA h g^{-1} for the second cycle, however, the discharge capacity was only 7.9 mA h g^{-1} at the end of 150 cycles, displaying a very serious capacity degradation, more than about 90% capacity fading, which can be attributed to the low electronic conductivity of α-Fe_2O_3 as well as substantial cathode pulverization after repeated Na-ion insertion/de-insertion. However, by interacting with rGO nanosheets, the cycling stability of α-Fe_2O_3 nanoparticles was significantly improved. Upon repeatedly 150 cycles, α-Fe_2O_3/rGO nanocomposites exhibited a good capacity retention of 50.1%, which is ~5 times higher than pristine α-Fe_2O_3. In addition, discharge capacities were substantially increased with an initial capacity of 135 mA h g^{-1} and achieved 57.4 mA h g^{-1} after 150 cycles. The enhanced Na-ion storage at a high current rate could be due to a highly

conductive matrix for the electron transport and low degree of crystallinity that enhances diffusion of Na^+ during Na-ion insertion and extraction.

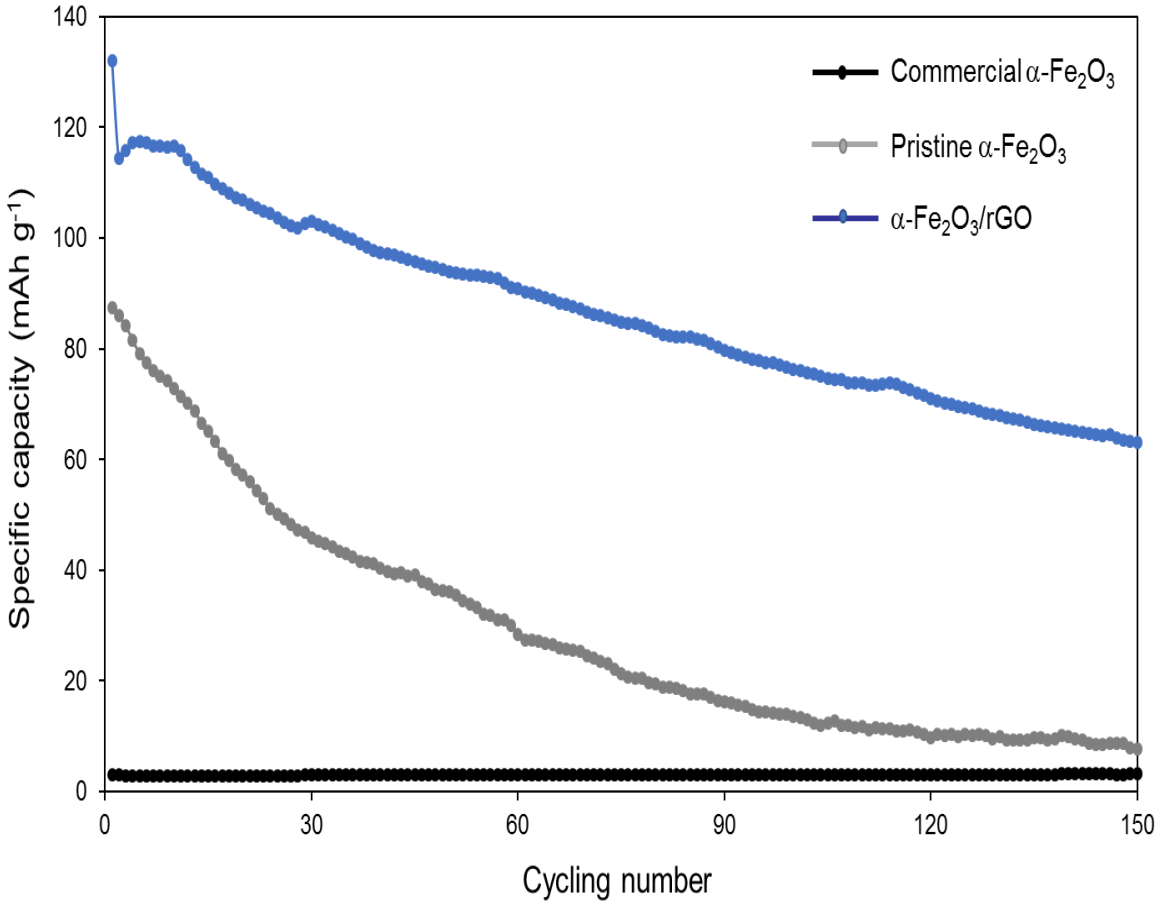

Figure 41. Cycling stability tests of high crystalline commercial α-Fe_2O_3, low crystalline α-Fe_2O_3, and α-Fe_2O_3/rGO nanocomposites (electrolyte with 1 M $NaClO_4$ in PC; counter/reference metallic Na; voltage range of 1.0-4.0 V vs Na; C-rate = 1.7 C (mass-normalized current of 170 mA g^{-1})).

Table 14. Average discharge capacity of the 2nd cycle and the 50th cycle, capacity retention, and coulombic efficiency of high crystalline commercial α-Fe_2O_3, low crystalline α-Fe_2O_3, and α-Fe_2O_3/rGO nanocomposites (the 2nd to 150th cycle) at 1.7 C (34 minutes discharge time).

Material ID	Discharge capacity (mAh g^{-1}) for the 2nd cycle	Discharge capacity (mAh g^{-1}) for the 150th cycle	Capacity Retention after 150 cycles (%)	Coulombic efficiency (%)
α-Fe_2O_3/rGO	115	57.4	50.1	99.0
Pristine α-Fe_2O_3	82.3	7.9	9.6	93.7
commercial α-Fe_2O_3	3.0	2.9	96.7	99.6

4. CONCLUSIONS

In the first objective, iron hydroxide/oxides ($Fe(OH)_3/\alpha\text{-}Fe_2O_3$) nanomaterials with different degrees of crystallinity were prepared by adjusting the reaction ratio of urea/Fe^{3+} and temperature via a facile hydrothermal synthesis. The role of the degree of structural order on the Na-ion charge storage was also investigated. Using a higher amount of urea and elevated temperature were found to have a significant effect on promoting structural order within iron hydroxides. Interestingly, it was also found that the morphologies of obtained $Fe(OH)_3/\alpha\text{-}Fe_2O_3$ were also significantly influenced by molar ratio of precursors and temperature. At a lower reaction temperature (120 °C) and with the participation of urea, the resulting materials were semi-crystalline $Fe(OH)_3$ nanosheets, whereas without urea or at enhanced temperature (180 °C), products were transformed to amorphous $Fe(OH)_3$ or $\alpha\text{-}Fe_2O_3$ nanoparticles, respectively. At a low current rate of 20 mA g^{-1}, amorphous $Fe(OH)_3$ nanoparticles exhibited a higher discharge capacity of ~214 mAh g^{-1} compared to semi-crystalline $Fe(OH)_3$ nanosheets (~209 mAh g^{-1}) and high crystalline $\alpha\text{-}Fe_2O_3$ nanoparticles (~131 mAh g^{-1}) as a result of an improved Na-ion diffusivity. However, a lower degree of semi-crystallinity $Fe(OH)_3$ nanosheets demonstrated the best rate capability and cycling stability due to combination of the faster electron transfer and a higher ionic conductivity.

In the second objective, low crystalline $\alpha\text{-}Fe_2O_3$ nanoparticles and $\alpha\text{-}Fe_2O_3$/rGO nanocomposites were fabricated by a rapid microwave synthesis method. The effect of structural order and integration with rGO were explored. Compared to high crystalline commercial $\alpha\text{-}Fe_2O_3$ nanoparticles, $\alpha\text{-}Fe_2O_3$ nanoparticles, and $\alpha\text{-}Fe_2O_3$/rGO nanocomposites with a low degree of crystallinity exhibited much higher specific

capacity. In addition, α-Fe_2O_3/rGO nanocomposites were found to more suitable for reversible Na-ion storage than low crystalline pristine α-Fe_2O_3 nanoparticles, which delivered a superior high specific capacity of ~183 mAh g^{-1} at 0.1 C and achieved ~111 mAh g^{-1} after 50 cycles. Furthermore, α-Fe_2O_3/rGO nanocomposites exhibited an excellent rate capacity with a reversible capability of 91.7 mAh g^{-1} at a current rate of 3.5 C(34 minutes charging/discharging time), whereas pristine α-Fe_2O_3 nanoparticles and high crystalline commercial α-Fe_2O_3 only showed a specific capacity of 19.3 mAh g^{-1} and 2.2 mAh g^{-1} at the same rate, respectively. At a high current rate (1.7 C), α-Fe_2O_3/rGO nanocomposites exhibited an initial reversible capacity of ~135.4 mAh g^{-1}, and a decent capacity of ~50.1 mAh g^{-1} retained after 150 cycles. The substantially improved electrochemical properties can be attributed to a low degree of structural order and interaction between α-Fe_2O_3 and rGO.

The significance of this study was to improve fundamental understanding of the important role of multiple factors, such as material crystallinity, electronic conductivity, and composites, in the improvement of Na-ion charge storage properties of iron hydroxide/oxide cathodes and to further the development of potential commercial and affordable cathode materials for Na-ion batteries beyond Li.

Further studies could be designed to improve the cycling stability and rate capability of iron hydroxide/oxide cathodes via optimizing their morphologies. The development of low crystalline iron hydroxide/oxide with a hollow structure, such as nanorings, hollow nanotubes, and hollow fibers could facilitate Na-ion transport without significantly pulverizing the structure upon cycling. Moreover, doping a small amount of metal cations , such as Co^{2+}, Ni^{2+}, Al^{3+}, and V^{5+}, into iron hydroxide/oxide nanomaterials

would increase their electronic conductivities, consequently being beneficial for better rate capabilities and cycling stabilities. In addition, hematite phase iron oxides, amorphous iron hydroxides, and maghemite (γ-Fe_2O_3) could be a potentially good cathodes with intrinsic cation vacancies for Na-ion storage. Studies focusing on increasing extra cation vacancies within γ-Fe_2O_3 structure would improve their Na-ion storage properties.

REFERENCES

1. Cox, P. M.; Betts, R. A.; Jones, C. D.; Spall, S. A.; Totterdell, I. J., Acceleration of global warming due to carbon-cycle feedbacks in a coupled climate model. *Nature* **2000,** *408*, 184-187.

2. Sarmiento, J. L.; Hughes, T. M. C.; Stouffer, R. J.; Manabe, S., Simulated response of the ocean carbon cycle to anthropogenic climate warming. *Nature* **1998,** *393*, 245-249.

3. Candelaria, S. L.; Shao, Y.; Zhou, W.; Li, X.; Xiao, J.; Zhang, J. G.; Wang, Y.; Liu, J.; Li, J.; Cao, G., Nanostructured carbon for energy storage and conversion. *Nano Energy* **2012,** *1*, 195-220.

4. Tans, P.; Keeling, R., *http://www.esrl.noaa.gov/gmd/ccgg/trends/* **2015**.

5. Schimel, D., The Science of Climate Change. *Cambridge Univ. Press, Cambridge* **1995**, 65–131.

6. Roberts, A. D.; Li, X.; Zhang, H., Porous carbon spheres and monoliths: morphology control, pore size tuning and their applications as Li-ion battery anode materials. *Chem. Soc. Rev.* **2014,** *43*, 4341-4356.

7. Abbasi, T.; Abbasi, S. A., "Renewable" hydrogen: prospects and challenges. *Renewable and Sustainable Energy Rev.* **2011,** *15*, 3034-3040.

8. Liu, C.; Li, F.; Ma, L. P.; Cheng, H. M., Advanced materials for energy storage. *Adv. Mater.* **2010,** *22*, E28-E62.

9. Tarascon, J. M.; Armand, M., Issues and challenges facing rechargeable lithium batteries. *Nature* **2001,** *414*, 359–367.

10. Goodenough, J. B.; Park, K. S., The Li-ion rechargeable battery: a perspective. *J. Am. Chem. Soc.* **2013,** *135*, 1167-1176.

11. Liu, C.; Neale, Z. G.; Cao, G., Understanding electrochemical potentials of cathode materials in rechargeable batteries. *Mater. Today* **2016,** *19*, 109-123.

12. Saha, P.; Datta, M. K.; Velikokhatnyi, O. I.; Manivannan, A.; Alman, D.; Kumta, P. N., Rechargeable magnesium battery: Current status and key challenges for the future. *Prog Mater Sci.* **2014,** *66*, 1-86.

13. Islam, M. S.; Fisher, C. A. J., Lithium and sodium battery cathode materials: computational insights into voltage, diffusion and nanostructural properties. *Chem. Soc. Rev.* **2014,** *43*, 185-204.

14. Yuan, L. X.; Wang, Z. H.; Zhang, W. X.; Hu, X. L.; Chen, J. T.; Huang, Y. H.; Goodenough, J. B., Development and challenges of $LiFePO_4$ cathode material for lithium-ion batteries. *Energy Environ. Sci.* **2011,** *4*, 269-284.

15. Tian, R.; Park, S.-H.; King, P. J.; Cunningham, G.; Coelho, J.; Nicolosi, V.; Coleman, J. N., Quantifying the factors limiting rate performance in battery electrodes. *Nat. Commun.* **2019,** *10*, 1933.

16. Wang, A.; Kadam, S.; Li, H.; Shi, S.; Qi, Y., Review on modeling of the anode solid electrolyte interphase (SEI) for lithium-ion batteries. *Npj Comput. Mater.* **2018,** *4*, 15.

17. Tarascon, J.-M., Is lithium the new gold? *Nat. chem.* **2010,** *2*, 510.

18. Practical Handbook of Physcial Properties of Rocks and Minerals. *Carmichael, R. S.* **1989**.

19. *https://www.metalary.com/lithium-price/*.

20. Tian, H.; Gao, T.; Li, X.; Wang, X.; Luo, C.; Fan, X.; Yang, C.; Suo, L.; Ma, Z.; Han, W., High power rechargeable magnesium/iodine battery chemistry. *Nat. Commun.* **2017,** *8*, 14083.

21. Zhao-Karger, Z.; Fichtner, M., Beyond intercalation chemistry for rechargeable Mg batteries: a short review and perspective. *Front Chem.* **2018,** *6*, 656-668.

22. Sa, N.; Kinnibrugh, T. L.; Wang, H.; Sai Gautam, G.; Chapman, K. W.; Vaughey, J. T.; Key, B.; Fister, T. T.; Freeland, J. W.; Proffit, D. L., Structural Evolution of Reversible Mg Insertion into a Bilayer Structure of V2O5· n H2O Xerogel Material. *Chem. Mater.* **2016,** *28*, 2962-2969.

23. Mizuno, Y.; Okubo, M.; Hosono, E.; Kudo, T.; Zhou, H.; Oh-ishi, K., Suppressed activation energy for interfacial charge transfer of a Prussian blue analog thin film electrode with hydrated ions (Li^+, Na^+, and Mg^{2+}). *J. Phys. Chem. C* **2013,** *117*, 10877-10882.

24. Zhang, R.; Yu, X.; Nam, K. W.; Ling, C.; Arthur, T. S.; Song, W.-G.; Knapp, A. M.; Ehrlich, S. N.; Yang, X. Q.; Matsui, M., α-MnO_2 as a cathode material for rechargeable Mg batteries. *Electrochem. commun.* **2012,** *23*, 110-113.

25. Tepavcevic, S.; Liu, Y.; Zhou, D.; Lai, B.; Maser, J.; Zuo, X.; Chan, H.; Král, P.; Johnson, C. S.; Stamenkovic, V., Nanostructured layered cathode for rechargeable Mg-ion batteries. *Acs Nano* **2015,** *9*, 8194-8205.

26. Sun, X.; Bonnick, P.; Nazar, L. F., Layered TiS_2 positive electrode for Mg batteries. *ACS Energy Lett.* **2016,** *1*, 297-301.

27. Li, Z.; Mu, X.; Zhao-Karger, Z.; Diemant, T.; Behm, R. J.; Kübel, C.; Fichtner, M., Fast kinetics of multivalent intercalation chemistry enabled by solvated magnesium-ions into self-established metallic layered materials. *Nat. Commun.* **2018,** *9*, 5115-5128.

28. Yoshimoto, N.; Matsumoto, M.; Egashia, M.; Morita, M., Mixed electrolyte consisting of ethylmagnesiumbromide with ionic liquid for rechargeable magnesium electrode. *J. Power Sources* **2010,** *195*, 2096-2098.

29. Ma, Z.; MacFarlane, D. R.; Kar, M., Mg cathode materials and electrolytes for rechargeable Mg batteries: A review. *Batteries & Supercaps* **2019,** *2*, 115-127.

30. Levi, E.; Gofer, Y.; Aurbach, D., On the way to rechargeable Mg batteries: the challenge of new cathode materials. *Chem. Mater.* **2009,** *22*, 860-868.

31. Kundu, D.; Vajargah, S. H.; Wan, L.; Adams, B.; Prendergast, D.; Nazar, L. F., Aqueous vs. nonaqueous Zn-ion batteries: consequences of the desolvation penalty at the interface. *Energy Environ. Sci.* **2018,** *11*, 881-892.

32. Wang, Y.; Yi, J.; Xia, Y., Recent progress in aqueous Lithium-ion batteries. *Adv. Energy Mater.* **2012,** *2*, 830-840.

33. Winter, M.; Brodd, R. J., What are batteries, fuel cells, and supercapacitors? Chem. Rev.: 2004; Vol. 104, pp 4245-4270.

34. Chen, X.; Wang, L.; Li, H.; Cheng, F.; Chen, J., Porous V_2O_5 nanofibers as cathode materials for rechargeable aqueous zinc-ion batteries. *J. Energy Chem.* **2019,** *38*, 20-25.

35. Li, W.; Wang, K.; Cheng, S.; Jiang, K., A long-life aqueous Zn-ion battery based on $Na_3V_2(PO_4)_2F_3$ cathode. *Energy Storage Mater.* **2018,** *15*, 14-21.

36. Alfaruqi, M. H.; Gim, J.; Kim, S.; Song, J.; Pham, D. T.; Jo, J.; Xiu, Z.; Mathew, V.; Kim, J., A layered δ-MnO_2 nanoflake cathode with high zinc-storage capacities for eco-friendly battery applications. *Electrochem. commun.* **2015,** *60*, 121-125.

37. Zhang, X. G., Corrosion and Electrochemistry of Zinc. *Springer US* **1996**.

38. Zhang, L.; Chen, L.; Zhou, X.; Liu, Z., Towards high-voltage aqueous metal-ion batteries beyond 1.5 V: the zinc/zinc hexacyanoferrate system. *Adv. Energy Mater.* **2015,** *5*, 1400930-1400935.

39. Ming, J.; Guo, J.; Xia, C.; Wang, W.; Alshareef, H. N., Zinc-ion batteries: Materials, mechanisms, and applications. *Materials Science and Engineering: R: Reports* **2019,** *135*, 58-84.

40. Zhang, W.; Liu, Y.; Guo, Z., Approaching high-performance potassium-ion batteries via advanced design strategies and engineering. *Sci Adv.* **2019,** *5*, 7412-7425.

41. Liu, Y.; Tai, Z.; Zhang, J.; Pang, W. K.; Zhang, Q.; Feng, H.; Konstantinov, K.; Guo, Z.; Liu, H. K., Boosting potassium-ion batteries by few-layered composite anodes prepared via solution-triggered one-step shear exfoliation. *Nat. Commun.* **2018,** *9*, 3645-3658.

42. Zhang, W.; Mao, J.; Li, S.; Chen, Z.; Guo, Z., Phosphorus-based alloy materials for advanced potassium-ion battery anode. *J. Am. Chem. Soc.* **2017,** *139*, 3316-3319.

43. Kim, H.; Ji, H.; Wang, J.; Ceder, G., Next-generation cathode materials for non-aqueous potassium-ion batteries. *Trends in Chemistry* **2019**.

44. Yu, X.; Manthiram, A., Toward reversible room-temperature calcium-ion batteries. *Chem* **2018,** *4*, 1200-1202.

45. Ponrouch, A.; Frontera, C.; Bardé, F.; Palacín, M. R., Towards a calcium-based rechargeable battery. *Nat. Mater.* **2016,** *15*, 169-173.

46. Gummow, R. J.; Vamvounis, G.; Kannan, M. B.; He, Y., Calcium-ion batteries: Current state-of-the-art and future perspectives. *Adv. Mater.* **2018,** *30*, 1801702.

47. Rong, Z.; Malik, R.; Canepa, P.; Sai Gautam, G.; Liu, M.; Jain, A.; Persson, K.; Ceder, G., Materials design rules for multivalent ion mobility in intercalation structures. *Chem. Mater.* **2015,** *27*, 6016-6021.

48. Leisegang, T.; Meutzner, F.; Zschornak, M.; Münchgesang, W.; Schmid, R.; Nestler, T.; Eremin, R. A.; Kabanov, A. A.; Blatov, V. A.; Meyer, D. C., The aluminum-ion battery: A sustainable and seminal concept? *Front Chem.* **2019,** *7*, 1-21.

49. Das, S. K.; Mahapatra, S.; Lahan, H., Aluminium-ion batteries: developments and challenges. *J. Mater. Chem. A* **2017,** *5*, 6347-6367.

50. Wang, M.; Tang, Y., A review on the features and progress of dual-ion batteries. *Adv. Energy Mater.* **2018,** *8*, 1703320.

51. Heckmann, A.; Thienenkamp, J.; Beltrop, K.; Winter, M.; Brunklaus, G.; Placke, T., Towards high-performance dual-graphite batteries using highly concentrated organic electrolytes. *Electrochim. Acta* **2018,** *260*, 514-525.

52. Pei, C.; Xiong, F.; Sheng, J.; Yin, Y.; Tan, S.; Wang, D.; Han, C.; An, Q.; Mai, L., VO2 nanoflakes as the cathode material of hybrid magnesium–lithium-ion batteries with high energy density. *ACS Appl. Mater. Interfaces* **2017,** *9*, 17060-17066.

53. Yabuuchi, N.; Kubota, K.; Dahbi, M.; Komaba, S., Research development on sodium-ion batteries. *Chem. rev.* **2014,** *114*, 11636-11682.

54. Böhm, H.; Beyermann, G., ZEBRA batteries, enhanced power by doping. *J Power Sources.* **1999,** *84*, 270-274.

55. Hueso, K. B.; Armand, M.; Rojo, T., High temperature sodium batteries: status, challenges and future trends. *Energy Environ. Sci.* **2013,** *6*, 734-749.

56. Whittingham, M. S., Chemistry of intercalation compounds: metal guests in chalcogenide hosts. *Prog. Solid State Chem.* **1978,** *12*, 41-99.

57. Slater, M. D.; Kim, D.; Lee, E.; Johnson, C. S., Sodium-ion batteries. *Adv. Func. Mater.* **2013,** *23*, 947-958.

58. Li, Y.; Lu, Y.; Zhao, C.; Hu, Y. S.; Titirici, M. M.; Li, H.; Huang, X.; Chen, L., Recent advances of electrode materials for low-cost sodium-ion batteries towards practical application for grid energy storage. *Energy Storage Materials* **2017,** *7*, 130-151.

59. Ong, S. P.; Chevrier, V. L.; Hautier, G.; Jain, A.; Moore, C.; Kim, S.; Ma, X.; Ceder, G., Voltage, stability and diffusion barrier differences between sodium-ion and lithium-ion intercalation materials. *Energy & Environmental Science* **2011,** *4*, 3680-3688.

60. Cho, M. K.; Jo, J. H.; Choi, J. U.; Kim, J.; Yashiro, H.; Yuan, S.; Shi, L.; Sun, Y.-K.; Myung, S.-T., Tunnel-type β-FeOOH cathode material for high rate sodium storage via a new conversion reaction. *Nano Energy* **2017,** *41*, 687-696.

61. Dai, Z.; Mani, U.; Tan, H. T.; Yan, Q., Advanced cathode materials for sodium-ion batteries: what determines our choices? *Small Methods* **2017,** *1*, 1700098.

62. Xiang, X.; Zhang, K.; Chen, J. T., Recent advances and prospects of cathode materials for sodium-ion batteries. *Adv. Mater.* **2015,** *27*, 5343-5364.

63. Hausbrand, R.; Cherkashinin, G.; Ehrenberg, H.; Gröting, M.; Albe, K.; Hess, C.; Jaegermann, W., Fundamental degradation mechanisms of layered oxide Li-ion battery cathode materials: Methodology, insights and novel approaches. *Materials Science and Engineering: B* **2015,** *192*, 3-25.

64. You, Y.; Wu, X.-L.; Yin, Y.-X.; Guo, Y.-G., A zero-strain insertion cathode material of nickel ferricyanide for sodium-ion batteries. *J. Mater. Chem. A* **2013,** *1*, 14061-14065.

65. Nitta, N.; Wu, F.; Lee, J. T.; Yushin, G., Li-ion battery materials: present and future. *Materials today* **2015,** *18*, 252-264.

66. Zhang, K.; Hu, Z.; Tao, Z.; Chen, J. T., Inorganic & organic materials for rechargeable Li batteries with multi-electron reaction. *Science China Materials* **2014,** *57*, 42-58.

67. Zhang, K.; Han, X.; Hu, Z.; Zhang, X.; Tao, Z.; Chen, J., Nanostructured Mn-based oxides for electrochemical energy storage and conversion. *Chemical Society Reviews* **2015,** *44*, 699-728.

68. Wang, Y.; Li, H.; He, P.; Hosono, E.; Zhou, H., Nano active materials for lithium-ion batteries. *Nanoscale* **2010,** *2*, 1294-1305.

69. Shewmon, P., Diffusion in Solids. *Springer, Cham* **2016**.

70. Fergus, J. W., Recent developments in cathode materials for lithium ion batteries. *J Power Sources.* **2010,** *195* (.), 939-954.

71. Mizushima, K.; Jones, P. C.; Wiseman, P. J.; Goodenough, J. B., Li_xCoO_2 (0< x<-1): A new cathode material for batteries of high energy density. *Materials Research Bulletin* **1980,** *15*, 783-789.

72. Billaud, J.; Clément, R. J.; Armstrong, A. R.; Canales-Vázquez, J.; Rozier, P.; Grey, C. P.; Bruce, P. G., β-$NaMnO_2$: a high-performance cathode for sodium-ion batteries. *J. Am. Chem. Soc.* **2014,** *136*, 17243-17248.

73. Zhao, J.; Zhao, L.; Dimov, N.; Okada, S.; Nishida, T., Electrochemical and thermal properties of α-$NaFeO_2$ cathode for Na-ion batteries. *J Electrochem Soc.* **2013,** *160*, A3077-A3081.

74. Vassilaras, P.; Ma, X.; Li, X.; Ceder, G., Electrochemical properties of monoclinic $NaNiO_2$. *J Electrochem Soc.* **2013,** *160*, A207-A211.

75. Hwang, J.-Y.; Myung, S.-T.; Sun, Y.-K., Sodium-ion batteries: present and future. *Chem. Soc. Rev.* **2017,** *46*, 3529-3614.

76. Mendiboure, A.; Delmas, C.; Hagenmuller, P., Electrochemical intercalation and deintercalation of Na_xMnO_2 bronzes. *J. Solid State Chem* **1985,** *57*, 323-331.

77. Zhao, J.; Zhao, L.; Dimov, N.; Okada, S.; Nishida, T., Electrochemical and thermal properties of α-$NaFeO_2$ cathode for Na-ion batteries. *J. Electrochem. Soc* **2013,** *160*, A3077-A3081.

78. Yuan, D. D.; Wang, Y. X.; Cao, Y. L.; Ai, X. P.; Yang, H. X., Improved electrochemical performance of Fe-substituted $NaNi_{0.5}Mn_{0.5}O_2$ cathode materials for sodium-ion batteries. *ACS Appl Mater Interfaces* **2015,** *7*, 8585-8591.

79. Yu, S.; Zhang, P.; Wu, S. Q.; Li, A. Y.; Zhu, Z. Z.; Yang, Y., Understanding the structural and electronic properties of the cathode material $NaFeF_3$ in a Na-ion battery. *J. Solid State Chem* **2014,** *18*, 2071-2075.

80. Gocheva, I. D.; Nishijima, M.; Doi, T.; Okada, S.; Yamaki, J.; Nishida, T., Mechanochemical synthesis of $NaMF_3$ (M= Fe, Mn, Ni) and their electrochemical properties as positive electrode materials for sodium batteries. *J Power Sources* **2009,** *187*, 247-252.

81. Kitajou, A.; Komatsu, H.; Chihara, K.; Gocheva, I. D.; Okada, S.; Yamaki, J., Novel synthesis and electrochemical properties of perovskite-type $NaFeF_3$ for a sodium-ion battery. *J Power Sources.* **2012,** *198*, 389-392.

82. Yamada, Y.; Doi, T.; Tanaka, I.; Okada, S.; Yamaki, J., Liquid-phase synthesis of highly dispersed $NaFeF_3$ particles and their electrochemical properties for sodium-ion batteries. *J Power Sources.* **2011,** *196*, 4837-4841.

83. Kravchyk, K. V.; Zünd, T.; Wörle, M.; Kovalenko, M. V.; Bodnarchuk, M. I., $NaFeF_3$ nanoplates as low-cost sodium and lithium cathode materials for stationary energy storage. *Chem. Mater.* **2018,** *30l*, 1825-1829.

84. Su, D.; Wang, G., Single-crystalline bilayered V_2O_5 nanobelts for high-capacity sodium-ion batteries. *ACS nano* **2013,** *7*, 11218-11226.

85. Bélanger, D.; Brousse, L.; Long, J. W., Manganese oxides: battery materials make the leap to electrochemical capacitors. *The Electrochemical Society Interface* **2008,** *17*, 49.

86. Komaba, S.; Mikumo, T.; Yabuuchi, N.; Ogata, A.; Yoshida, H.; Yamada, Y., Electrochemical insertion of Li and Na ions into nanocrystalline Fe_3O_4 and α-Fe_2O_3 for rechargeable batteries. *J. Electrochem. Soc* **2010,** *157*, A60-A65.

87. Liu, S.; Tong, Z.; Zhao, J.; Liu, X.; Ma, X.; Chi, C.; Yang, Y.; Liu, X.; Li, Y., Rational selection of amorphous or crystalline V_2O_5 cathode for sodium-ion batteries. *Phys. Chem. Chem. Phys.* **2016,** *18*, 25645-25654.

88. Leong, C. C.; Pan, H.; Ho, S. K., Two-dimensional transition-metal oxide monolayers as cathode materials for Li and Na ion batteries. *Phys Chem Chem Phys* **2016,** *18*, 7527-7534.

89. Tian, Y.; Shi, T.; Richards, W. D.; Li, J.; Kim, J. C.; Bo, S.-H.; Ceder, G., Compatibility issues between electrodes and electrolytes in solid-state batteries. *Energy Environ. Sci.* **2017,** *10*, 1150-1166.

90. Ellis, B. L.; Nazar, L. F., Sodium and sodium-ion energy storage batteries. *Curr. Opin. Solid State Mater. Sci.* **2012,** *16*, 168-177.

91. https://markets.businessinsider.com/commodities/iron-ore-price.

92. Li, K.; Chen, H.; Shua, F.; Chen, K.; Xue, D., Low temperature synthesis of Fe_2O_3 and $LiFeO_2$ as cathode materials for lithium-ion batteries. *Electrochim. Acta* **2014,** *136*, 10-18.

93. http://www.infomine.com/investment/cobalt/.

94. Yu, S.; Ng, V. M. H.; Wang, F.; Xiao, Z.; Li, C.; Kong, L. B.; Que, W.; Zhou, K., Synthesis and application of iron-based nanomaterials as anodes of lithium-ion batteries and supercapacitors. *J. Mater. Chem. A* **2018,** *6*, 9332-9367.

95. Cornell, R. M.; Schwertmann, U., The iron oxides: structure, properties, reactions, occurrences and uses. *Wiley VCH* **2003**.

96. Hu, Q.; Kim, D. Y.; Yang, W.; Yang, L.; Meng, Y.; Zhang, L.; Mao, H. K., FeO_2 and FeOOH under deep lower-mantle conditions and Earth's oxygen–hydrogen cycles. *Nature* **2016,** *534*, 241-244.

97. Ye, H.; Wang, Y.; Zhao, F.; Huang, W.; Han, N.; Zhou, J.; Zeng, M.; Li, Y., Iron-based sodium-ion full batteries. *J. Mater. Chem. A* **2016,** *4*, 1754-1761.

98. Koo, B.; Chattopadhyay, S.; Shibata, T.; Prakapenka, V. B.; Johnson, C. S.; Rajh, T.; Shevchenko, E. V., Intercalation of sodium ions into hollow iron oxide nanoparticles. *Chem. Mater.* **2013,** *25*, 245-252.

99. Rao, C. N. R.; Muller, A.; Cheetham, A. K., *The chemistry of nanomaterials*. Wiley Online Library: 2004; Vol. 1.

100. Du, W.; Gupta, A.; Zhang, X.; Sastry, A. M.; Shyy, W., Effect of cycling rate, particle size and transport properties on lithium-ion cathode performance. *Int. J. Heat Mass Transf.* **2010,** *53*, 3552-3561.

101. Das, S.; Li, J.; Hui, R. In *Impact of electrode surface/volume ratio on Li-ion battery performance*, Proceedings of the COMSOL Conference, Boston, MA, USA, 2014; pp 8-10.

102. Duan, Y.; Zhang, B.; Zheng, J.; Hu, J.; Wen, J.; Miller, D. J.; Yan, P.; Liu, T.; Guo, H.; Li, W., Excess Li-ion storage on reconstructed surfaces of nanocrystals to boost battery performance. *Nano lett* **2017,** *17*, 6018-6026.

103. Teja, A. S.; Koh, P. Y., Synthesis, properties, and applications of magnetic iron oxide nanoparticles. *Prog. Cryst. Growth Charact. Mater.* **2009,** *55*, 22-45.

104. Ma, M.; Zhang, Y.; Guo, Z.; Gu, N., Facile synthesis of ultrathin magnetic iron oxide nanoplates by Schikorr reaction. *Nanoscale Res. Lett.* **2013,** *8*, 8-16.

105. Niu, S.; McFeron, R.; Godínez-Salomón, F.; Chapman, B. S.; Damin, C. A.; Tracy, J. B.; Augustyn, V.; Rhodes, C. P., Enhanced Electrochemical Lithium-Ion Charge Storage of Iron Oxide Nanosheets. *Chem. Mater.* **2017,** *29*, 7794-7807.

106. Das, R.; Cardarelli, J. A.; Phan, M. H.; Srikanth, H., Magnetically tunable iron oxide nanotubes for multifunctional biomedical applications. *J. Alloys Compd.* **2019,** *789*, 323-329.

107. Zhu, Y.; Lei, J.; Tian, Y., Uniform iron oxide hollow spheres for high-performance delivery of insoluble anticancer drugs. *Dalton Trans.* **2014,** *43*, 7275-7281.

108. Zhong, L. S.; Hu, J. S.; Liang, H. P.; Cao, A. M.; Song, W. G.; Wan, L. J., Self-Assembled 3D flowerlike iron oxide nanostructures and their application in water treatment. *Adv. Mater.* **2006,** *18*, 2426-2431.

109. Butler, S. Z.; Hollen, S. M.; Cao, L.; Cui, Y.; Gupta, J. A.; Gutiérrez, H. R.; Heinz, T. F.; Hong, S. S.; Huang, J.; Ismach, A. F., Progress, challenges, and opportunities in two-dimensional materials beyond graphene. *ACS nano* **2013,** *7*, 2898-2926.

110. Heine, T., Transition metal chalcogenides: ultrathin inorganic materials with tunable electronic properties. *Acc. Chem. Res.* **2014,** *48*, 65-72.

111. Zhuiykov, S.; Kats, E., Atomically thin two-dimensional materials for functional electrodes of electrochemical devices. *Ionics* **2013,** *19*, 825-865.

112. Zhang, Z.; Han, Y.; Xu, J.; Ma, J.; Zhou, X.; Bao, J., Construction of amorphous $FePO_4$ nanosheets with enhanced sodium storage properties. *ACS Appl. Mater. Interfaces* **2018,** *1*, 4395-4402.

113. Wang, J.; Cui, Y.; Wang, D., Design of hollow nanostructures for energy storage, conversion and production. *Adv. Mater.* **2018,** *1801993*, 1-24.

114. Wang, S.; Wang, W.; Zhan, P.; Jiao, S., Hollow α-Fe_2O_3 nanospheres synthesized using a carbon template as novel anode materials for Na-ion batteries. *Chem. Electro. Chem.* **2014,** *1*, 1636-1639.

115. Amine, K.; Yasuda, H.; Yamachi, M., β-FeOOH, a new positive electrode material for lithium secondary batteries. *J. Power Sources* **1999,** *81*, 221-223.

116. Gong, K.; Yan, Y.; Zhang, M.; Su, L.; Xiong, S.; Mao, L., Electrochemistry and electroanalytical applications of carbon nanotubes: a review. *Analytical sciences* **2005,** *21*, 1383-1393.

117. Khan, M.; Tahir, M. N.; Adil, S. F.; Khan, H. U.; Siddiqui, M. R. H.; Al-warthan, A. A.; Tremel, W., Graphene based metal and metal oxide nanocomposites: synthesis, properties and their applications. *J. Mater. Chem. A* **2015,** *3*, 18753-18808.

118. Pei, S.; Cheng, H.-M., The reduction of graphene oxide. *Carbon* **2012,** *50*, 3210-3228.

119. Georgakilas, V.; Otyepka, M.; Bourlinos, A. B.; Chandra, V.; Kim, N.; Kemp, K. C.; Hobza, P.; Zboril, R.; Kim, K. S., Functionalization of graphene: covalent and non-covalent approaches, derivatives and applications. *Chem. Rev.* **2012,** *112*, 6156-6214.

120. Zhang, L.; Wu, H. B.; Lou, X. W., Iron-oxide-based advanced anode materials for lithium-ion batteries. *Adv. Energy Mater.* **2014,** *4*, 1300958.

121. Ali, G.; Oh, S. H.; Kim, S. Y.; Kim, J. Y.; Cho, B. W.; Chung, K. Y., An open-framework iron fluoride and reduced graphene oxide nanocomposite as a high-capacity cathode material for Na-ion batteries. *J. Mater. Chem. A* **2015,** *3*, 10258-10266.

122. Liu, Y.; Xu, S.; Zhang, S.; Zhang, J.; Fan, J.; Zhou, Y., Direct growth of $FePO_4$/reduced graphene oxide nanosheet composite for sodium-ion battery *J. Mater. Chem. A* **2015,** *3*, 5501-5508

123. Qi, T.; Jiang, J.; Chen, H.; Wan, H.; Miao, L.; Zhang, L., Synergistic effect of Fe_3O_4/reduced graphene oxide nanocomposites for supercapacitors with good cycling life. *Electrochimica Acta* **2013,** *114*, 674-680.

124. Qu, J.; Yin, Y.-X.; Wang, Y.-Q.; Yan, Y.; Guo, Y.-G.; Song, W.-G., Layer structured α-Fe_2O_3 nanodisk/reduced graphene oxide composites as high-performance anode materials for lithium-ion batteries. *ACS Appl. Mater. Interfaces* **2013,** *5*, 3932-3936.

125. Sun, B.; Jiang, Z.; Fang, D.; Xu, K.; Pei, Y.; Yan, S.; Qiao, M.; Fan, K.; Zong, B., One-pot approach to a highly robust iron oxide/reduced graphene oxide nanocatalyst for fischer–tropsch synthesis. *Chem.Cat. Chem.* **2013,** *5* (3), 714-719.

126. Wang, Z.; Liu, C.-J., Preparation and application of iron oxide/graphene based composites for electrochemical energy storage and energy conversion devices: current status and perspective. *Nano Energy* **2015,** *11*, 277-293.

127. Xu, R.; Xu, Y., *Modern inorganic synthetic chemistry*. Elsevier: 2010.

128. Hosono, E.; Saito, T.; Hoshino, J.; Okubo, M.; Saito, Y.; Nishio-Hamane, D.; Kudo, T.; Zhou, H., High power Na-ion rechargeable battery with single-crystalline $Na_{0.44}MnO_2$ nanowire electrode. *J Power Sources.* **2012,** *217*, 43-46.

129. Tilley, R. J. D., Defects in solids. *John Wiley & Sons, Inc. A* **2008**.

130. Hahn, B. P.; Long, J. W.; Rolison, D. R., Something from nothing: enhancing electrochemical charge storage with cation vacancies. *Accounts of chemical research* **2012,** *46*, 1181-1191.

131. Ahmed, S. I.; Heiba, Z. K.; Mostafa, N. Y.; Shaltout, A. A.; Aljoudy, H. S., The role of high-valent (Mo and V) cations in defect spinel iron oxide nanomaterials: toward improving Li-ion storage. *Ceramics International* **2018,** *In Press, Accepted Manuscript*.

132. Chervin, C. N.; Ko, J. S.; Miller, B. W.; Dudek, L.; Mansour, A. N.; Donakowski, M. D.; Brintlinger, T.; Gogotsi, P.; Chattopadhyay, S.; Shibata, T., Defective by design: vanadium-substituted iron oxide nanoarchitectures as cation-insertion hosts for electrochemical charge storage. *J. Mater. Chem. A* **2015,** *3*, 12059-12068.

133. Hahn, B. P.; Long, J. W.; Mansour, A. N.; Pettigrew, K. A.; Osofsky, M. S.; Rolison, D. R., Electrochemical Li-ion storage in defect spinel iron oxides: the critical role of cation vacancies. *Energy & Environmental Science* **2011,** *4*, 1495-1502.

134. Yan, S.; Abhilash, K. P.; Tang, L.; Yang, M.; Ma, Y.; Xia, Q.; Guo, Q.; Xia, H., Research advances of amorphous metal oxides in electrochemical energy storage and conversion. *Small* **2019,** *15*, 1804371-1804401.

135. Ide, K.; Nomura, K.; Hiramatsu, H.; Kamiya, T.; Hosono, H., Structural relaxation in amorphous oxide semiconductor, a-In-Ga-Zn-O. *J. Appl. Phys.* **2012,** *111*, 073513-073519.

136. Buchholz, D. B.; Ma, Q.; Alducin, D.; Ponce, A.; Jose-Yacaman, M.; Khanal, R.; Medvedeva, J. E.; Chang, R. P. H., The structure and properties of amorphous indium oxide. *Chem. Mater.* **2014,** *26*, 5401-5411.

137. Chen, K.; Xue, D., Searching for electrode materials with high electrochemical reactivity. *Journal of Materiomics* **2015,** *1*, 170-187.

138. Ma, X.-H.; Zhang, F.; Wei, Y.-Y.; Zhou, J.-H.; Wang, J.; Jia, W.; Zi, Z.-F.; Dai, J.-M., Facile synthesis of amorphous $FeVO_4$ nanoparticles as novel cathode materials for sodium-ion batteries. *Journal of Alloys and Compounds* **2018,** *768*, 181-189.

139. Wang, Z.; Wang, Z.; Liu, W.; Xiao, W.; Lou, X. W. D., Amorphous $CoSnO_3$@C nanoboxes with superior lithium storage capability. *Energy Environ. Sci.* **2013,** *6*, 87-91.

140. Lytle, J. C.; Rhodes, C. P.; Long, J. W.; Pettigrew, K. A.; Stroud, R. M.; Rolison, D. R., The importance of combining disorder with order for Li-ion insertion into cryogenically prepared nanoscopic ruthenia. *J. Mater. Chem.* **2007,** *17*, 1292-1299.

141. Jiang, Z.; Lu, W.; Li, Z.; Ho, K. H.; Li, X.; Jiao, X.; Chen, D., Synthesis of amorphous cobalt sulfide polyhedral nanocages for high performance supercapacitors. *J. Mater. Chem. A* **2014,** *2*, 8603-8606.

142. Heitjans, P.; Tobschall, E.; Wilkening, M., Ion transport and diffusion in nanocrystalline and glassy ceramics. *The European Physical Journal Special Topics* **2008,** *161*, 97-108.

143. Venkatesh, G.; Pralong, V.; Lebedev, O. I.; Caignaert, V.; Bazin, P.; Raveau, B., Amorphous sodium vanadate $Na_{1.5+y}VO_3$, a promising matrix for reversible sodium intercalation. *Electrochem. commun.* **2014,** *40*, 100-102.

144. Mathew, V.; Kim, S.; Kang, J.; Gim, J.; Song, J.; Baboo, J. P.; Park, W.; Ahn, D.; Han, J.; Gu, L., Amorphous iron phosphate: potential host for various charge carrier ions. *NPG Asia Materials* **2014,** *6*, e138-e148.

145. Zhang, L.; Ji, S.; Yu, L.; Xu, X.; Liu, J., Amorphous FeF_3/C nanocomposite cathode derived from metal–organic frameworks for sodium ion batteries. *RSC Advances* **2017,** *7*, 24004-24010.

146. Liu, Y.; Xu, Y.; Han, X.; Pellegrinelli, C.; Zhu, Y.; Zhu, H.; Wan, J.; Chung, A. C.; Vaaland, O.; Wang, C., Porous amorphous $FePO_4$ nanoparticles connected by single-wall carbon nanotubes for sodium ion battery cathodes. *Nano Lett.* **2012,** *12*, 5664-5668.

147. Shiratsuchi, T.; Okada, S.; Yamaki, J.; Nishida, T., $FePO_4$ cathode properties for Li and Na secondary cells. *J. Power Sources* **2006,** *159*, 268-271.

148. Liu, Y.; Zhou, Y.; Zhang, J.; Zhang, S.; Xu, S., The transformation from amorphous iron phosphate to sodium iron phosphate in sodium-ion batteries. *Phys. Chem. Chem. Phys.* **2015,** *17*, 22144-22151.

149. Zhou, Y.; Chen, T.; Zhang, J.; Liu, Y.; Ren, P., Amorphous MnO_2 as cathode material for sodium-ion batteries. *Chinese Journal of Chemistry* **2017,** *35*, 1294-1298.

150. Uchaker, E.; Zheng, Y. Z.; Li, S.; Candelaria, S. L.; Hu, S.; Cao, G. Z., Better than crystalline: amorphous vanadium oxide for sodium-ion batteries. *J. Mater. Chem. A* **2014,** *2*, 18208-18214.

151. Nagata, Y.; Nagao, K.; Deguchi, M.; Sakuda, A.; Hayashi, A.; Tsukasaki, H.; Mori, S.; Tatsumisago, M., Amorphization of sodium cobalt oxide active materials for high-capacity all-solid-state sodium batteries. *Chem. Mater.* **2018,** *30*, 6998-7004.

152. Fischer, W. R.; Schwertmann, U., The formation of hematite from amorphous iron (III) hydroxide. *Clays Clay Miner.* **1975,** *23*, 33-37.

153. Schwertmann, U.; Fischer, W. R., Natural "amorphous" ferric hydroxide. *Geoderma* **1973,** *10*, 237-247.

154. Shinoda, K.; Matsubara, E.; Muramatsu, A.; Waseda, Y., Local structure of ferric hydroxide $Fe(OH)_3$ in aqueous solution by the anomalous X-ray scattering and EXAFS methods. *Materials Transactions, JIM* **1994,** *35*, 394-398.

155. McCammon, C. A.; Pring, A.; Keppler, H.; Sharp, T., A study of bernalite, $Fe(OH)_3$, using Mössbauer spectroscopy, optical spectroscopy and transmission electron microscopy. *Phys. Chem. Miner.* **1995,** *22*, 11-20.

156. Cornell, R. M.; Giovanoli, R.; Schneider, W., Review of the hydrolysis of iron (III) and the crystallization of amorphous iron (III) hydroxide hydrate. *J. Chem. Technol. Biotechnol.* **1989,** *46*, 115-134.

157. Popov, V. V.; Gorbunov, A. I., Effect of organic acids on the hydrothermal crystallization of $Fe(OH)_3$. *Inorg. Mater.* **2006,** *42*, 769-776.

158. Au-Yeung, S. C. F.; Eaton, D. R.; Birchall, T.; Dénès, G.; Greedan, J. E.; Hallett, C.; Ruebenbauer, K., The preparation and characterization of iron trihydroxide, $Fe(OH)_3$. *Canadian journal of chemistry* **1985,** *63*, 3378-3385.

159. Chen, X. Q.; Wu, S. B.; Cao, R. B.; Tao, J. S., Preparation and characterization of nanosized hematite colloids using green vitriol as ferrum source. *Journal of Nanomaterials* **2014,** *2014*, 46-54.

160. Du, M.; Xu, C.; Sun, J.; Gao, L., Synthesis of α-Fe_2O_3 nanoparticles from $Fe(OH)_3$ sol and their composite with reduced graphene oxide for lithium ion batteries. *J. Mater. Chem. A* **2013,** *1*, 7154-7158.

161. Su, M.; He, C.; Shih, K., Facile synthesis of morphology and size-controlled α-Fe_2O_3 and Fe_3O_4 nano-and microstructures by hydrothermal/solvothermal process: the roles of reaction medium and urea dose. *Ceramics International* **2016,** *42*, 14793-14804.

162. Zhang, Y.; Wang, S.; Wang, X.; Qian, Y.; Zhang, Z., Assembled CuO hollow spheres from nanoparticles. *Journal of nanoscience and nanotechnology* **2006,** *6*, 1423-1426.

163. Yu, J.; Yu, X.; Huang, B.; Zhang, X.; Dai, Y., Hydrothermal synthesis and visible-light photocatalytic activity of novel cage-like ferric oxide hollow spheres. *Crystal Growth and Design* **2009,** *9*, 1474-1480.

164. Gulina, L.; Tolstoy, V.; Kuklo, L.; Mikhailovskii, V.; Panchuk, V.; Semenov, V., Synthesis of $Fe(OH)_3$ microtubes at the gas–solution interface and their use for the fabrication of Fe_2O_3 and Fe microtubes. *Eur. J. Inorg. Chem.* **2018,** *2018*, 1842-1846.

165. Shah, A. K.; Prathap, K. J.; Kumar, M.; Abdi, S. H. R.; Kureshy, R. I.; Noor-ul, H. K.; Bajaj, H. C., $Fe(OH)_3$ nano solid material: An efficient catalyst for regioselective ring opening of aryloxy epoxide with amines under solvent free condition. *Applied Catalysis A: General* **2014,** *469*, 442-450.

166. Pauling, L.; Hendricks, S. B., The crystal structures of hematite and corundum. *J. Am. Chem. Soc.* **1925,** *47*, 781-790.

167. Tamirat, A. G.; Rick, J.; Dubale, A. A.; Su, W. N.; Hwang, B. J., Using hematite for photoelectrochemical water splitting: a review of current progress and challenges. *Nanoscale Horiz.* **2016,** *1*, 243-267.

168. Tiquia-Arashiro, S.; Rodrigues, D., Nanoparticles synthesized by microorganisms. In *Extremophiles: Applications in Nanotechnology*, Springer: 2016; pp 1-51.

169. Dzade, N.; Roldan, A.; de Leeuw, N., A density functional theory study of the adsorption of benzene on hematite (⟨-Fe_2O_3) surfaces. *Minerals* **2014,** *4*, 89-115.

170. Jain, G.; Balasubramanian, M.; Xu, J. J., Structural studies of lithium intercalation in a nanocrystalline ⟨-Fe_2O_3 compound. *Chem. Mater.* **2006,** *18*, 423-434.

171. Tadić, M.; Čitaković, N.; Panjan, M.; Stojanović, Z.; Marković, D.; Spasojević, V., Synthesis, morphology, microstructure and magnetic properties of hematite submicron particles. *J. Alloys Compd.* **2011,** *509*, 7639-7644.

172. Zhu, M.; Wang, Y.; Meng, D.; Qin, X.; Diao, G., Hydrothermal synthesis of hematite nanoparticles and their electrochemical properties. *J. Phys. Chem. C* **2012,** *116*, 16276-16285.

173. Liao, P.; Toroker, M. C.; Carter, E. A., Electron transport in pure and doped hematite. *Nano Lett.* **2011,** *11*, 1775-1781.

174. Russell, H. B., Characterization of hematite nanowire arrays synthesized by atmospheric plasma. **2011**.

175. Pant, P.; Naik, B. D.; Ghosh, N. N., Synthesis of α-Fe_2O_3 nano powder by simple chemical method. *Mater Technol.* **2009,** *24*, 213-216.

176. Dawy, M.; Safaa, K.; Mahy, E.; Aziz, E. A., Synthesis, characterization and electrical properties of α-Fe_2O_3 nanoparticle. *Aust J Basic Appl Sci* **2012,** *6*, 55-62.

177. Li, L.; Chu, Y.; Liu, Y.; Dong, L., Template-free synthesis and photocatalytic properties of novel Fe_2O_3 hollow spheres. *J. Phys. Chem. C* **2007,** *111*, 2123-2127.

178. Akbar, S.; Hasanain, S. K.; Azmat, N.; Nadeem, M., Synthesis of Fe_2O_3 nanoparticles by new Sol-Gel method and their structural and magnetic characterizations. **2004**.

179. Kopanja, L.; Milosevic, I.; Panjan, M.; Damnjanovic, V.; Tadic, M., Sol–gel combustion synthesis, particle shape analysis and magnetic properties of hematite (α-Fe_2O_3) nanoparticles embedded in an amorphous silica matrix. *Appl Surf Sci.* **2016,** *362*, 380-386.

180. Lassoued, A.; Lassoued, M. S.; Dkhil, B.; Ammar, S.; Gadri, A., Synthesis, photoluminescence and magnetic properties of iron oxide (α-Fe_2O_3) nanoparticles through precipitation or hydrothermal methods. *Physica E: Low-dimensional Systems and Nanostructures* **2018,** *101*, 212-219.

181. Fouad, D. E.; Zhang, C.; El-Didamony, H.; Yingnan, L.; Mekuria, T. D.; Shah, A. H., Improved size, morphology and crystallinity of hematite (α-Fe_2O_3) nanoparticles synthesized via the precipitation route using ferric sulfate precursor. *Results in Physics* **2019,** *12*, 1253-1261.

182. Kijima, N.; Yoshinaga, M.; Awaka, J.; Akimoto, J., Microwave synthesis, characterization, and electrochemical properties of α-Fe_2O_3 nanoparticles. *Solid State Ion.* **2011,** *192*, 293-297.

183. Qiu, G.; Huang, H.; Genuino, H.; Opembe, N.; Stafford, L.; Dharmarathna, S.; Suib, S. L., Microwave-assisted hydrothermal synthesis of nanosized α-Fe_2O_3 for catalysts and adsorbents. *J. Phys. Chem. C* **2011,** *115*, 19626-19631.

184. Liao, X.; Zhu, J.; Zhong, W.; Chen, H. Y., Synthesis of amorphous Fe_2O_3 nanoparticles by microwave irradiation. *Mater. Lett.* **2001,** *50*, 341-346.

185. Zhu, X.; Zhu, Y.; Murali, S.; Stoller, M. D.; Ruoff, R. S., Nanostructured reduced graphene oxide/Fe_2O_3 composite as a high-performance anode material for lithium ion batteries. *ACS nano* **2011,** *5*, 3333-3338.

186. Han, S.; Hu, L.; Liang, Z.; Wageh, S.; Al-Ghamdi, A. A.; Chen, Y.; Fang, X., One-step hydrothermal synthesis of 2D hexagonal nanoplates of α-Fe_2O_3/graphene composites with enhanced photocatalytic activity. *Adv. Funct. Mater.* **2014,** *24*, 5719-5727.

187. Liang, S.; Zhu, J.; Wang, C.; Yu, S.; Bi, H.; Liu, X.; Wang, X., Fabrication of α-Fe_2O_3@graphene nanostructures for enhanced gas-sensing property to ethanol. *Appl. Surf. Sci.* **2014,** *292*, 278-284.

188. Modafferi, V.; Fiore, M.; Fazio, E.; Patanè, S.; Triolo, C.; Santangelo, S.; Ruffo, R.; Neri, F.; Musolino, M. G., Modelling, Measurement and Control B. *Journal homepage: http://iieta. org/Journals/MMC/MMC_B* **2018,** *87*, 129-134.

189. Zhang, H.; Yu, L.; Li, Q.; Du, Y.; Ruan, S., Reduced graphene oxide/α-Fe_2O_3 hybrid nanocomposites for room temperature NO_2 sensing. *Sensors and Actuators B: Chemical* **2017,** *241*, 109-115.

190. Wang, Z.; Ma, C.; Wang, H.; Liu, Z.; Hao, Z., Facilely synthesized Fe_2O_3–graphene nanocomposite as novel electrode materials for supercapacitors with high performance. *J. Alloys Compd.* **2013,** *552*, 486-491.

191. Nasiri, M.; Sangpour, P.; Yousefzadeh, S.; Bagheri, M., Elevated temperature annealed α-Fe_2O_3/reduced graphene oxide nanocomposite photoanode for photoelectrochemical water oxidation. *J. Environ. Chem. Eng.* **2019,** *7*, 102999.

192. Liu, X.; Chen, T.; Chu, H.; Niu, L.; Sun, Z.; Pan, L.; Sun, C. Q., Fe_2O_3-reduced graphene oxide composites synthesized via microwave-assisted method for sodium ion batteries. *Electrochim. Acta* **2015,** *166*, 12-16.

193. Lin, J.; Raji, A. O.; Nan, K.; Peng, Z.; Yan, Z.; Samuel, E. L. G.; Natelson, D.; Tour, J. M., Iron oxide nanoparticle and graphene nanoribbon composite as an anode material for high-performance li-ion batteries. *Adv Funct Mater.* **2014,** *24*, 2044-2048.

194. Fang, Y.; Xiao, L.; Qian, J.; Ai, X.; Yang, H.; Cao, Y. L., Mesoporous amorphous $FePO_4$ nanospheres as high-performance cathode material for sodium-ion batteries. *Nano letters* **2014,** *14*, 3539-3543.

195. Hummers Jr, W. S.; Offeman, R. E., Preparation of graphitic oxide. *J. Am. Chem. Soc.* **1958,** *80*, 1339-1339.

196. Lin, Y. F.; Chen, J. L.; Xu, C. Y.; Chung, T. W., One-pot synthesis of paramagnetic iron (III) hydroxide nanoplates and ferrimagnetic magnetite nanoparticles for the removal of arsenic ions. *Chem. Eng. J.* **2014,** *250*, 409-415.

197. Cheng, B.; Wang, W.; Shi, L.; Zhang, J.; Ran, J.; Yu, H., One-pot template-free hydrothermal synthesis of monoclinic hollow microspheres and their enhanced visible-light photocatalytic activity. *Int. J Photoenergy.* **2012,** *2012*, 1-10.

198. Yu, J.; Kudo, A., Effects of structural variation on the photocatalytic performance of hydrothermally synthesized $BiVO_4$. *Adv. Funct. Mater.* **2006,** *16*, 2163-2169.

199. Qurashi, A.; Zhong, Z.; Alam, M. W., Synthesis and photocatalytic properties of α-Fe_2O_3 nanoellipsoids. *Solid State Sci.* **2010,** *12*, 1516-1519.

200. Pinto, P. S.; Lanza, G. D.; Ardisson, J. D.; Lago, R. M., Controlled dehydration of $Fe(OH)_3$ to Fe_2O_3: Developing mesopores with complexing iron species for the adsorption of β-lactam antibiotics. *J. Braz. Chem. Soc.* **2019,** *30*, 310-317.

201. Wu, G.; Tan, X.; Li, G.; Hu, C., Effect of preparation method on the physical and catalytic property of nanocrystalline Fe_2O_3. *J. Alloys Compd.* **2010,** *504*, 371-376.

202. Onari, S.; Arai, T.; Kudo, K., Infrared lattice vibrations and dielectric dispersion in α−Fe_2O_3. *Phys. Rev. B* **1977,** *16*, 1717.

203. Bishop, J. L.; Murad, E.; Dyar, M. D., Akaganéite and schwertmannite: Spectral properties and geochemical implications of their possible presence on Mars. *Am. Mineral.* **2015,** *100*, 738-746.

204. Iiu, Y.; Lv, J.; Jin, W.; Zhao, Y., Defluoridation by rice spike-like akaganeite anchored graphene oxide. *RSC Adv.* **2016,** *6*, 11240-11249.

205. Tran, P. H.; Hang, A. H. T., Deep eutectic solvent-catalyzed arylation of benzoxazoles with aromatic aldehydes. *RSC adv.* **2018,** *8*, 11127-11133.

206. Lappi, S. E.; Smith, B.; Franzen, S., Infrared spectra of $H_2{}^{16}O$, $H_2{}^{18}O$ and D_2O in the liquid phase by single-pass attenuated total internal reflection spectroscopy. *Spectrochimica Acta Aart A: molecular and biomolecular spectroscopy* **2004,** *60*, 2611-2619.

207. Parveen, M. F.; Umapathy, S.; Dhanalakshmi, V.; Anbarasan, R., Synthesis and characterizations of nanosized iron (II) hydroxide and iron (II) hydroxide/poly (vinyl alcohol) nanocomposite. *J. Appl. Polym. Sci.* **2010,** *118*, 1728-1737.

208. Zhao, W.; Wu, Y.; Xu, J.; Gao, C., Retraction: Effect of ethylene glycol on hydrothermal formation of calcium sulfate hemihydrate whiskers with high aspect ratios. *RSC Adv.* **2016,** *6*, 99639-99639.

209. Chuntonov, L.; Kumar, R.; Kuroda, D. G., Non-linear infrared spectroscopy of the water bending mode: direct experimental evidence of hydration shell reorganization? *Phys. Chem. Chem. Phys.* **2014,** *16*, 13172-13181.

210. Manivannan, M.; Rajendran, S., Investigation of inhibitive action of urea–Zn^{2+} system in the corrosion control of carbon steel in sea water. *Int. J Eng. Sci. Technol.* **2011,** *3*, 8048-8060.

211. Amonette, J. E.; Rai, D., Identification of noncrystalline (Fe, Cr)$(OH)_3$ by infrared spectroscopy. *Clays Clay Miner.* **1990,** *38*, 129-136.

212. Ali, G.; Kim, H. J.; Kim, J. J.; Cho, S. O., Controlled fabrication of porous double-walled TiO_2 nanotubes via ultraviolet-assisted anodization. *nanoscale* **2014,** *6*, 3632-3637.

213. Wang, H. L.; Cui, J. Y.; Jiang, W. F., Synthesis, characterization and flocculation activity of novel $Fe(OH)_3$–polyacrylamide hybrid polymer. *Mater. Chem. Phys.* **2011,** *130*, 993-999.

214. Vieira, L.; Schennach, R.; Gollas, B., In situ PM-IRRAS of a glassy carbon electrode/deep eutectic solvent interface. *Phys. Chem. Chem. Phys.* **2015,** *17*, 12870-12880.

215. Zhou, Y. X.; Yao, H. B.; Zhang, Q.; Gong, J. Y.; Liu, S. J.; Yu, S. H., Hierarchical $FeWO_4$ microcrystals: solvothermal synthesis and their photocatalytic and magnetic properties. *Inorg. Chem.* **2009,** *48*, 1082-1090.

216. Qin, X.; Wang, J.; Xie, J.; Li, F.; Wen, L.; Wang, X., Hydrothermally synthesized $LiFePO_4$ crystals with enhanced electrochemical properties: simultaneous suppression of crystal growth along [010] and antisite defect formation. *Phys. Chem. Chem. Phys.* **2012,** *14*, 2669-2677.

217. Bumajdad, A.; Ali, S.; Mathew, A., Characterization of iron hydroxide/oxide nanoparticles prepared in microemulsions stabilized with cationic/non-ionic surfactant mixtures. *J. Colloid Interface Sci.* **2011,** *355*, 282-292.

218. Pinto, P. S.; Medeiros, T. P. V.; Ardisson, J. D.; Lago, R. M., Role of $[FeO_x(OH)_y]$ surface sites on the adsorption of β-lactamic antibiotics on Al_2O_3 supported Fe oxide. *J. Hazard. Mater.* **2016,** *317*, 327-334.

219. Ong, S. P.; Chevrier, V. L.; Hautier, G.; Jain, A.; Moore, C.; Kim, S.; Ma, X.; Ceder, G., Voltage, stability and diffusion barrier differences between sodium-ion and lithium-ion intercalation materials. *Energy Environ. Sci.* **2011,** *4*, 3680-3688.

220. Byles, B. W.; Palapati, N. K. R.; Subramanian, A.; Pomerantseva, E., The role of electronic and ionic conductivities in the rate performance of tunnel structured manganese oxides in Li-ion batteries. *APL Mater.* **2016,** *4*, 046108-046120.

221. Liu, J.; Xue, D., Hollow nanostructured anode materials for Li-ion batteries. *Nanoscale Res. Lett.* **2010,** *5*, 1525.

222. Malik, R.; Burch, D.; Bazant, M.; Ceder, G., Particle size dependence of the ionic diffusivity. *Nano Lett.* **2010,** *10* (10), 4123-4127.

223. Abe, T.; Fukuda, H.; Iriyama, Y.; Ogumi, Z., Solvated Li-ion transfer at interface between graphite and electrolyte. *J. Electrochem. Soc.* **2004,** *151*, A1120-A1123.

224. Liu, W. R.; Guo, Z. Z.; Young, W. S.; Shieh, D. T.; Wu, H. C.; Yang, M. H.; Wu, N. L., Effect of electrode structure on performance of Si anode in Li-ion batteries: Si particle size and conductive additive. *J. Power Sources* **2005,** *140*, 139-144.

225. Di Lecce, D.; Hassoun, J., Lithium transport properties in $LiMn_{1-\alpha}Fe_{\alpha}PO_4$ olivine cathodes. *J. Phys. Chem. C* **2015,** *119*, 20855-20863.

226. .Perera, S. D.; Archer, R. B.; Damin, C. A.; Mendoza-Cruz, R.; Rhodes, C. P., Controlling interlayer interactions in vanadium pentoxide-poly (ethylene oxide) nanocomposites for enhanced magnesium-ion charge transport and storage. *J. Power Sources* **2017,** *343*, 580-591.

227. Esmanski, A.; Ozin, G. A., Silicon inverse-opal-based macroporous materials as negative electrodes for lithium ion batteries. *Adv. Funct. Mater.* **2009,** *19* (12), 1999-2010.

228. Bahl, S. K.; Chopra, K. L., Electrical and optical properties of amorphous vs crystalline GeTe films. *J. Vac. Sci. Technol.* **1969,** *6*, 561-565.

229. Sheng, Y.; Tang, X.; Peng, E.; Xue, J., Graphene oxide based fluorescent nanocomposites for cellular imaging. *J. Mater. Chem. B* **2013,** *1*, 512-521.

230. Wen, Y.; He, K.; Zhu, Y.; Han, F.; Xu, Y.; Matsuda, I.; Ishii, Y.; Cumings, J.; Wang, C., Expanded graphite as superior anode for sodium-ion batteries. *Nat Commun.* **2014,** *5*, 4033-4043.

231. Some, S.; Kim, Y.; Yoon, Y.; Yoo, H.; Lee, S.; Park, Y.; Lee, H., High-quality reduced graphene oxide by a dual-function chemical reduction and healing process. *Sci. Rep.* **2013,** *3*, 1929.

232. Yun, Y. S.; Kim, D.-H.; Hong, S. J.; Park, M. H.; Park, Y. W.; Kim, B. H.; Jin, H. J.; Kang, K., Microporous carbon nanosheets with redox-active heteroatoms for pseudocapacitive charge storage. *Nanoscale* **2015,** *7*, 15051-15058.

233. Childres, I.; Jauregui, L. A.; Park, W.; Cao, H.; Chen, Y. P., Raman spectroscopy of graphene and related materials. *New developments in photon and materials research* **2013,** *1*, 1-20.

234. Beams, R.; Cançado, L. G.; Novotny, L., Raman characterization of defects and dopants in graphene. *J. Phys. Condens. Matter.* **2015,** *27*, 083002.

235. Wu, T.; Wang, X.; Qiu, H.; Gao, J.; Wang, W.; Liu, Y., Graphene oxide reduced and modified by soft nanoparticles and its catalysis of the Knoevenagel condensation. *J. Mater. Chem.* **2012,** *22*, 4772-4779.

236. Park, O. K.; Choi, Y. M.; Hwang, J. Y.; Yang, C. M.; Kim, T. W.; You, N. H.; Koo, H. Y.; Lee, J. H.; Ku, B. C.; Goh, M., Defect healing of reduced graphene oxide via intramolecular cross-dehydrogenative coupling. *Nanotechnology* **2013,** *24*, 185604-185611.

237. Ali, G.; Mehmood, A.; Ha, H. Y.; Kim, J.; Chung, K. Y., Reduced graphene oxide as a stable and high-capacity cathode material for Na-ion batteries. *Sci. Rep.* **2017,** *7*, 40910-40918.

238. Wang, Y.; Hu, M.; Ai, D.; Zhang, H.; Huang, Z. H.; Lv, R.; Kang, F., Sulfur-doped reduced graphene oxide for enhanced sodium ion pseudocapacitance. *Nanomaterials* **2019,** *9*, 752-762.

239. Lee, S. W.; Yabuuchi, N.; Gallant, B. M.; Chen, S.; Kim, B. S.; Hammond, P. T.; Shao-Horn, Y., High-power lithium batteries from functionalized carbon-nanotube electrodes. *Nat. Nanotechnol.* **2010,** *5*, 531.

240. Nollet, L. M. L.; Toldrá, F.; Benjakul, S.; Paliyath, G.; Hui, Y. H., *Food biochemistry and food processing*. John Wiley & Sons: 2012.

241. Monshi, A.; Foroughi, M. R.; Monshi, M. R., Modified Scherrer equation to estimate more accurately nano-crystallite size using XRD. *World journal of nano science and engineering* **2012,** *2*, 154-160.

242. Kan, J.; Wang, Y., Large and fast reversible Li-ion storages in Fe_2O_3-graphene sheet-on-sheet sandwich-like nanocomposites. *Sci. Rep.* **2013,** *3*, 3502.

243. Li, D.; Zhou, J.; Chen, X.; Song, H., Amorphous Fe_2O_3/graphene composite nanosheets with enhanced electrochemical performance for sodium-ion battery. *ACS Appl. Mater. Interfaces* **2016,** *8*, 30899-30907.

244. Li, L.; Zheng, Y.; Zhang, S.; Yang, J.; Shao, Z.; Guo, Z., Recent progress on sodium ion batteries: Potential high-performance anodes. *Energy Environ. Sci.* **2018,** *11*, 2310-2340.

245. Zou, Y.; Kan, J.; Wang, Y., Fe_2O_3-graphene rice-on-sheet nanocomposite for high and fast lithium ion storage. *J. Phys. Chem. C* **2011,** *115*, 20747-20753.